Universidade do Estado do Rio de Janeiro

Centro de Tecnologia e Ciências

Faculdade de Engenharia

Daniel Lessa Coelho
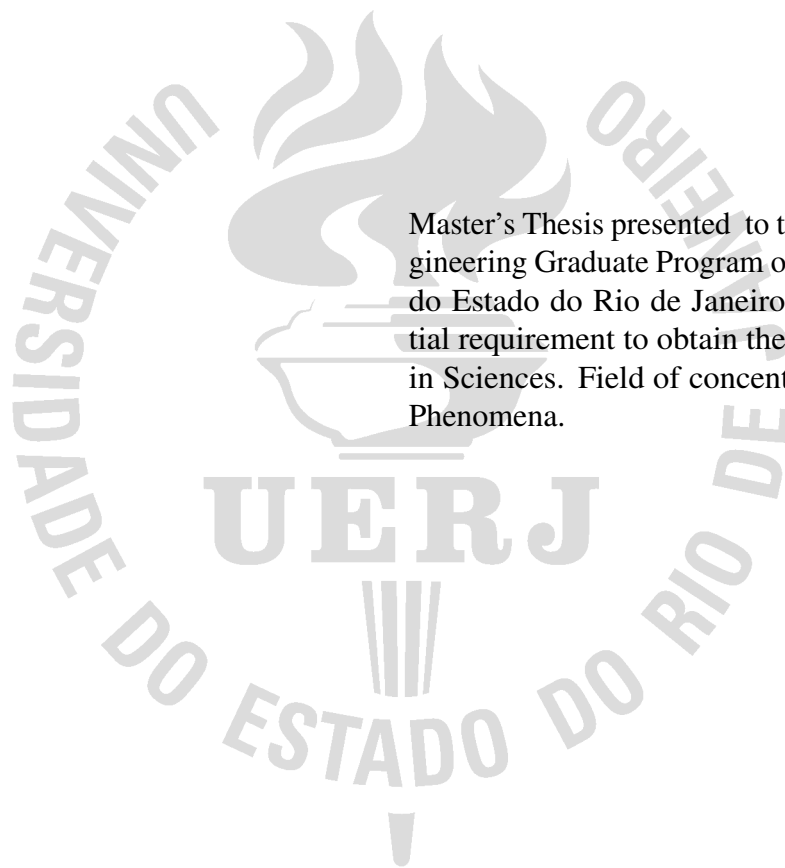
NONLINEAR ANALYSIS AND NUMERICAL INVESTIGATIONS OF ORIENTATIONAL EFFECTS IN SWIFT-HOHENBERG DYNAMICS

Rio de Janeiro

2020

Daniel Lessa Coelho

NONLINEAR ANALYSIS AND NUMERICAL INVESTIGATIONS OF ORIENTATIONAL EFFECTS IN SWIFT-HOHENBERG DYNAMICS

Master's Thesis presented to the Mechanical Engineering Graduate Program of the Universidade do Estado do Rio de Janeiro (UERJ) as a partial requirement to obtain the degree of Master in Sciences. Field of concentration: Transport Phenomena.

Advisor: Prof. José da Rocha Miranda Pontes (FEN/UERJ)
Co-Advisor: Prof. Norberto Mangiavacchi (FEN/UERJ)

Rio de Janeiro

2020

CATALOGAÇÃO NA FONTE

UERJ / REDE SIRIUS / BIBLIOTECA CTC/B

Autorizo, apenas para fins acadêmicos e científicos, a reprodução total ou parcial desta tese, desde que citada a fonte.

_____   _____
              Assinatura   28/12/2021
                                                              Data

Daniel Lessa Coelho

NONLINEAR ANALYSIS AND NUMERICAL INVESTIGATIONS OF ORIENTATIONAL EFFECTS IN SWIFT-HOHENBERG DYNAMICS

Master's Thesis presented to the Mechanical Engineering Graduate Program of the Universidade do Estado do Rio de Janeiro (UERJ) as a partial requirement to obtain the degree of Master in Sciences. Field of concentration: Transport Phenomena.

Approved on December 28, 2020.
Examining Committee:

Prof. José da Rocha Miranda Pontes, D.Sc. (Advisor)
PPG-EM UERJ

Prof. Norberto Mangiavacchi, Ph.D. (Co-Advisor)
PPG-EM UERJ

Prof. Alvaro Luiz Gayoso de Azeredo Coutinho, D.Sc.
COPPE UFRJ

Prof. Bruno Werneck Mintz, D.Sc.
PPGF UERJ

Eduardo Vitral Freigedo Rodrigues, Ph.D.
University of Nevada, Reno

Prof. Luca Roberto Augusto Moriconi, D.Sc.
PPGF UFRJ

Rio de Janeiro, Brazil
2020

ACKNOWLEDGMENTS

you for being a great company, and for the lessons I learned with each one of you.
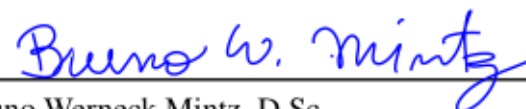
My great coworkers at GESAR: José Elias, Luis Carnevale, Lívia Corrêa, and Leandro Marques. I am very grateful for our moments of learning and joy together.

My dear parents, Sergio and Adriana, without whom none of this would be possible for me. Thank you for supporting me in my decisions, and for helping me to see them through. I am grateful for all your love, kindness, and for investing so much in my education. Thank you, my dear father, for cherishing my work for years, and for hearing me talk about chaos theory, atomic scale processes, nonlinear differential equations, and other crazy stuff I love studying. Thank you, my dear mother, for encouraging me to always go further. I extend my gratitude to all my family, whose support is essential for my journey.

I also acknowledge the State University of Rio de Janeiro (UERJ), for being the stage of many great life experiences during my education in both my graduation and masters. UERJ has been my second home for years, and where I found most of these great people I have the pleasure of working with. It was where my dreams became reality, and they keep becoming because of this great institution.

"Love is the one thing we're capable of perceiving
that transcends dimensions of time and space.
Maybe we should trust that, even if we can't understand it."

Christopher Nolan (Interstellar, 2014)

RESUMO

A formação de padrões espaço-temporais em sistemas naturais origina-se de uma dinâmica não linear rica, que pode levar ao surgimento de estruturas periódicas fora do equilíbrio. Uma das equações de maior sucesso, atualmente disponíveis, para investigar teoricamente o comportamento dessas estruturas é a Swift-Hohenberg (SH), que contém um parâmetro de bifurcação (forçagem) que controla a dinâmica alterando o nível energético do sistema. Embora uma grande parte da literatura sobre formação de padrões aborde sistemas uniformemente forçados, as forçagens não uniformes também são observadas em vários sistemas naturais, como por exemplo, em biologia do desenvolvimento e em aplicações de matéria condensada mole. Nesses casos, um efeito de orientação devido a um gradiente da forçagem é um novo fator desempenhando um papel no desenvolvimento dos padrões, particularmente na classe de padrões de listras, que investigamos por meio da dinâmica SH não uniformemente forçada. O presente trabalho aborda a estabilidade da orientação das listras e a competição entre o efeito de orientação do gradiente e outros efeitos de *bulk*, de borda e geométricos que participam da seleção dos padrões emergentes. Uma análise do fracamente não linear mostra que as listras tendem a se alinhar com o gradiente e se tornam instáveis quando perpendiculares à direção preferida. Esta análise é complementada por um trabalho numérico que leva em conta outros efeitos concorrentes. A abordagem numérica adotada consiste em um esquema semi-implícito de diferenças finitas com precisão de segunda ordem no tempo e no espaço, que é revisado e estendido com sucesso para as equações quadrática-cúbica (SH23) e cúbica-quíntica (SH35). As simulações mostram que as listras se alinham ou mesmo se reorientam a partir de condições preexistentes. No entanto, observamos que este efeito de orientação nem sempre prevalece em face de outros efeitos concorrentes.

Palavras-chave: Formação de padrões; Equação de Swift-Hohenberg; Método das diferenças finitas; Métodos Pseudo-espectrais.

ABSTRACT

COELHO, Daniel Lessa. *Nonlinear analysis and numerical investigations of orientational effects in Swift-hohenberg dynamics* . 93 f. Dissertação (Mestrado em Engenharia Mecânica) - Faculdade de Engenharia, Universidade do Estado do Rio de Janeiro (UERJ), Rio de Janeiro, 2020.

Spatio-temporal pattern formation in natural systems originates from rich nonlinear dynamics, which may lead to the emergence of periodic nonequilibrium structures. One of the most successful equations currently available for theoretically investigating the behavior of these structures is the Swift-Hohenberg (SH), which contains a bifurcation parameter (forcing) that controls the dynamics by changing the energy landscape of the system. Though a large part of the literature on pattern formation addresses uniformly forced systems, nonuniform forcings are also observed in several natural systems, for instance, in developmental biology and in soft matter applications. In these cases, an orientation effect due to a forcing gradient is a new factor playing a role in the development of patterns, particularly in the class of stripe patterns, which we investigate through the nonuniformly forced SH dynamics. The present work addresses the stability of stripes orientation, and the competition between the orientation effect of the gradient and other bulk, boundary, and geometric effects taking part in the selection of the emerging patterns. A weakly nonlinear analysis shows that stripes tend to align with the gradient, and become unstable when perpendicular to the preferred direction. This analysis is complemented by a numerical work that accounts for other competing effects. The adopted numerical approach consists of a semi-implicit finite-difference scheme with second order accuracy in both time and space, which is successfully reviewed and extended for the quadratic-cubic (SH23) and cubic-quintic (SH35) equations. Simulations show that stripes align, or even reorient from preexisting conditions. However, we observe that this orientation effect does not always prevail in face of further competing effects.

Keywords: Pattern formation; Swift-Hohenberg equation; Finite difference methods; Pseudo-spectral methods.

LIST OF FIGURES

LIST OF TABLES

LIST OF ABBREVIATIONS AND ACRONYMS

1D	One-dimensional
2D	Two-dimensional
3D	Three-dimensional
ADI	Alternating direction implicit
BC	Boundary conditions
FD	Finite difference
FE	Finite elements
FV	Finite volume
GDBC	Generalized Dirichlet boundary conditions
GL	Ginzburg-Landau
LB	Landau-Brazovskii
LHS	Left-hand side
MMS	Method of manufactured solutions
MS	Manufactured solution
NS	Navier-Stokes
NWS	Newell-Whitehead-Segel
OB	Oberbeck–Boussinesq
ODE	Ordinary differential equation
PBC	Periodic boundary conditions
PDE	Partial differential equation
PFM	Phase field method
PFC	Phase field crystal
PS	Pseudo-Spectral
RB	Rayleigh-Bénard
RD	Reaction-diffusion
RHS	Right-hand side
SH	Swift-Hohenberg
SH3	Cubic Swift-Hohenberg
SH23	Quadratic-cubic Swift-Hohenberg
SH35	Cubic-quintic Swift-Hohenberg
SmA	Smetic-A
WSL	Weak segregation limit

LIST OF SYMBOLS

Greek letters

ε	Control (bifurcation) parameter
ρ	Density
Λ	Spatially discretized differential operator
μ	Dynamic viscosity
ν	Kinematic viscosity
ψ	Order parameter
$\alpha, \zeta, \beta, \gamma$	Swift-Hohenberg equation parameters
λ	Wavelength

Roman letters

P	Pressure
T	Temperature
x, t	Position, Time
v	velocity

Superscripts

$(\cdot)^{n+1}$	Function in the new time step
$(\cdot)^{n+1/2}$	Function in the half time step
$(\cdot)^{n}$	Function in the current time step
$(\cdot)^{p+1}$	Function in the new iteration
$(\cdot)^{p}$	Function in the current iteration

Subscripts

L_x	Domain length in x-direction
L_y	Domain length in y-direction
ψ_m	Manufactured solution
ψ_k	Numerical solution

Symbols

$O(\cdot), \sim$	Asymptotic notation
$\mathcal{F}(\cdot)$	Fourier transform
$\mathcal{F}^{-1}(\cdot)$	Inverse Fourier transform
Ma	Marangoni number
Pr	Prandtl number
Ra	Rayleigh number
Re	Reynolds number

SUMMARY

INTRODUCTION

Nonlinear phenomena are commonly observed throughout nature. In many social and natural systems, matter and energy are continuously exchanged with their environment, as they are out of equilibrium. The emergence of order in such systems may be unexpected, but it definitely surprises the common sense by manifesting rich, vastous, and intriguing spatio-temporal pattern formation. From biology to materials science, one observes patterns in vegetation, climatic phenomena, human anatomy, animal coating, natural convection, materials microstructure, etc. The constant exchange with the environment allows the occurrence of instabilities characteristic of such nonequilibrium physical systems.

The instability mechanisms underlying spatio-temporal pattern formation in nature share some common and interesting features. The spontaneous appearance and evolution of organized states of matter out of equilibrium were described, in 1971, by Prigogine and Nicolis as dissipative structures (GLANSDORFF; PRIGOGINE, 1971). Following this investigation, Haken developed, in 1983, the concept of synergy to express the effects of cooperation resulting from nonlinearities (HAKEN, 1983), which was also named by Krinsky in 1984 as self-organization (KRINSKY, 1984). Synergy was the most accepted of these terms, and today it is well known in many other fields of knowledge, especially in developmental biology.

Before his death, Turing (1952) addressed the chemical basis of morphogenesis, predicting oscillating chemical reactions such as the Belousov-Zhabotinski (BZ) reaction (ZHABOTINSKI, 1964) originating from reaction-diffusion systems. Turing's developments went beyond scientific computing and today, reaction-diffusion systems still form an important class of systems capable of exhibiting self-organization phenomena and producing various types of spatio-temporal patterns from the diffusion of reacting species. In chemistry and developmental biology, there are further examples of Turing structures described by reaction-diffusion systems. One of them is the Brusselator reaction-diffusion mechanism, proposed by Prigogine and Lefever (1968), which has been studied as a toy model for pattern formation due to its analytical accessibility. It contains the basic ingredients which lead to destabilization of a uniform steady state towards an intriguing pattern formation (stripes, hexagons, e.g.). These Turing structures were first experimentally observed, in 1990, in the reaction with iodide-malonic chlorite acid (CASTETS et al., 1990), from the development of gel reactors in the laboratory. Figure 1 shows three examples of natural systems and a copolymer–homopolymer blend microstructure displaying commonly observed spatio-temporal patterns. They illustrate how self-organization phenomena is present in very distinct physical systems, and how their instabilities trigger similar intricate patterns.

Several physical problems in hydrodynamics, chemistry, nonlinear optics or in materials science, are related to the determination of instability mechanisms and the formation, selection and stability of the associated spatio-temporal patterns. These systems are usually described by nonlinear partial differential equations, and it is either impossible or impracticable to obtain

Figure 1 - Pattern formation in a copolymer–homopolymer blend, and in distinct natural systems. Self-organization of spatially periodic patterns can be observed in several physical systems, from materials microstructure to zebra coating. These phenomena are driven by similar instability mechanisms, and can produce particular stripes orientations and topological defects.
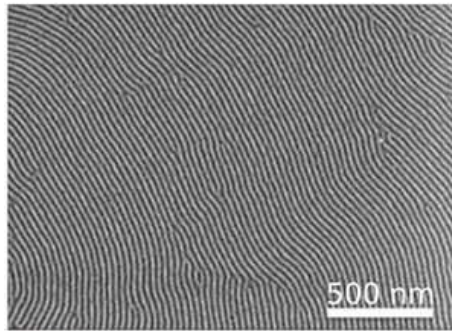
(a) Copolymer blend microstructure (DO-ERK; YAGER, 2017).

(b) Cloudy sky (COLEMAN, 2009).
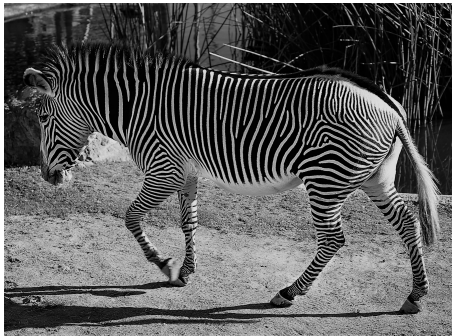
(c) Anna the Grevy's Zebra (GRUBB, 2020).

(d) Murzuq desert, Libya (SALVADOR, 2020).

Source: Authors indicated.

analytical solutions for them. However, some techniques guarantee an approximate solution (easier to achieve) in the vicinity of instability, based on, e.g., perturbation and bifurcation theories, or even asymptotic analysis (amplitude equation formalism). In the past fifty years, these methods have been successfully implemented to study some of these problems involving the transition from uniform states to nonuniform ones, which can be periodic, chaotic, etc. In materials science, these states are not necessarily induced by microscopic properties, but due to the collective behavior of a large number of atoms, molecules and cells, as they are result of phase transitions, defect dynamics, etc.

Swift and Hohenberg (1977) proposed a reduced model (equation) to study pattern formation in Rayleigh-Bénard convection. This type of natural convection takes place when a horizontal layer of fluid is heated from below, and the fluid develops a pattern of convection cells or of two-dimensional rolls (from planform view). They performed this reduction near the vicinity of their instability point. Around this point, the emergence of a particular pattern is expected, and its evolution is dominated by the dynamics of the first unstable modes. This is

Figure 2 - Rayleigh-Bénard convection (a) experimental (MEYER; CANNELL; AHLERS, 1992), and (b)
numerical (Original work by the author, 2020) results for a small circular domain with rigid
boundary conditions ($\psi = \partial_n \psi = 0$, where n is the unit outward normal vector).
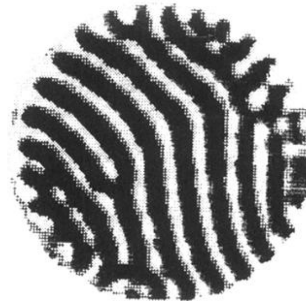
(a) Shadowgraph image of   (b) Dynamics simulated by
a convective pattern.   the SH equation.

Source: Authors indicated.

known as the weakly nonlinear regime, where these modes play the role of an order parameter
under an asymptotic dynamics of the Ginzburg-Landau type. In this regime (only), it's possible to
capture the main features from the whole dynamics by studying the reduced dynamics involving
these order parameters, which are linear combinations of the original variables. This reduction is
performed by adiabatically eliminating the stable modes, and, therefore, is referred to as adiabatic
elimination. Such technique was also performed for many systems featuring Turing instability
modeled by reaction-diffusion equations (HAKEN, 1981; WALGRAEF, 1997).

The Swift-Hohenberg (SH) equation (SWIFT; HOHENBERG, 1977) has been widely
used as a mathematical framework for modeling pattern formation in many physical systems
presenting symmetry breaking instabilities. The classical example where this symmmetry
breaking occurs is found in the emergence of convection stripes in a thin layer of fluid heated from
below, illustrated in Fig. 2. Roughly speaking, the SH equation has three basic pattern-forming
mechanisms, related to each term of the equation (CROSS, 2009):

$$\frac{\partial \psi}{\partial t} = \varepsilon \psi - \left(\nabla^2 + q_0^2 \right)^2 \psi - \psi^3 \, .$$

Basically, the nonlinear term saturates the linear growth promoted by the linear terms. Any
positive value for the control (or bifurcation) parameter ε "allows" the emergence of a periodic
structure with a wavenumber close to q_0, i.e., this parameter corresponds to the exponential
growth, the quadratic operator is a wavenumber filter of the pattern, and the negative cubic term is
related to the saturation of the dynamics. The linear term is accompanied by a control parameter
(related to temperature in the case of Rayleigh Bénard convection) and will be addressed as a
forcing parameter. It represents how far from the onset of the instability the system is. Secondly,
the wavelength filter contains all the equation spatial derivatives and tends to lead the pattern to
have the chosen critical wavelength. Finally the nonlinear terms allow for interactions between

the modes involved in the dynamics. There are versions of the SH equation, that are applied to further applications. In the SH3, the cubic term is responsible for saturating the linear growth. In the SH35, for example, the cubic term destabilizes the dynamics while the quintic one is responsible for the saturation. This extension of the original SH equation has been used to study the evolution of smectic-A (SmA) liquid crystal interfaces (VITRAL; LEO; VIÑALS, 2019), and the free energy functional associated with SH35 equation has been applied to the study of lamellar block copolymer microstructures for composition patterns in the weak segregation limit (WSL) using mean-field theory (AMUNDSON; HELFAND, 1993). In the Phase Field Crystal (PFC) framework, the SH equation is also considered as the "model A" of periodic systems (PROVATAS et al., 2005; ELDER et al., 2002; ELDER; GRANT, 2004), and its structure has been largely used to describe pure materials and their dynamics.

Although the SH equation and its similar versions have been extensively applied for the study of nonequlibrium pattern formation, not many works are found, addressing the orientation effect of gradients on a structure of stripes. More recently, Hiscock and Megason (2015) conducted analytical and numerical studies on the preferred orientation of stripe patterns in biological systems, using the Swift-Hohenberg equation. They concluded that gradients of the bifurcation parameter can induce stripe orientation in the Swift-Hohenberg dynamics and this was also verified by other analytical (SRULJES, 1970; WALTON, 1983) and numerical (PONTES, 1994; PONTES; WALGRAEF; CHRISTOV, 2008) investigations. However, this gradient effect faces competition from boundary, bulk and geometric effects, and stripes orientation becomes an intricate question. Since the SH equation can be used to study stripe patterns (Fig. 3), and many physical applications of interest demand oriented structures in order to realize or optimize some kind of electrical, mechanical, or chemical processing, it is interesting to tackle the question of how control parameter gradients affect their orientation under distinct forcings and boundary conditions.

This work extends Hiscock & Megason's work for the SH3 equation by initially studying the stability of stripes orientation in the direction of the gradient of the control parameter, in absence of other competing effects. For that purpose, we perform a weakly nonlinear analysis which suggests that the stripes tend to align in the gradient direction. A pair of Newell-Whitehead-Segel (NWS) equations is derived, from which we propose the amplitude instability induced by forcing gradients. In order to account for other competitive effects, we complement the previous analysis with a numerical work.

In the present work, a finite differences scheme, known as Stabilizing Correction (YA-NENKO; HOLT, 1971; CHRISTOV; PONTES, 2002), developed to integrate the cubic Swift-Hohenberg equation in two dimensions, is implemented. We extend their work, by employing rigid and periodic boundary conditions (PBC), distinct distributions of the control parameter (ramps, sinusoidal, gaussian), strict implementation of the associated Lyapunov functional, and second order representation of all derivatives, for both SH3 and SH35 equations.

Figure 3 - Microstructural zoology obtained by SH-like equations. (a) System forced with a constant control parameter ($\varepsilon = 0.1$), (b) System forced with a ramp of the control parameter ($0 \leqslant \varepsilon \leqslant 0.2$), (c) System with the addition of an anisotropic term ($\partial_x^2 \psi$) into the dynamics, and (d) System forced with a gaussian distribution of the control parameter. Applying the PFC approach, considering free energy functional of SH type, where the order parameter ψ follows a conserved dynamics, (e) a single crystal is obtained departing from a initial hexagonal seed, and (f) multiple grains are obtained starting with random initial conditions, both subjected to a constant control parameter. In (a), (b), (c), and (d), the system is subjected to rigid boundary conditions, and in (e) and (f), periodic boundary conditions (PBC).

| (a) Uniformly forced system | (b) Ramped system | (c) Anisotropic system |

| (d) Gaussian forcing | (e) Single crystal | (f) Multiple crystals and grain boundaries |
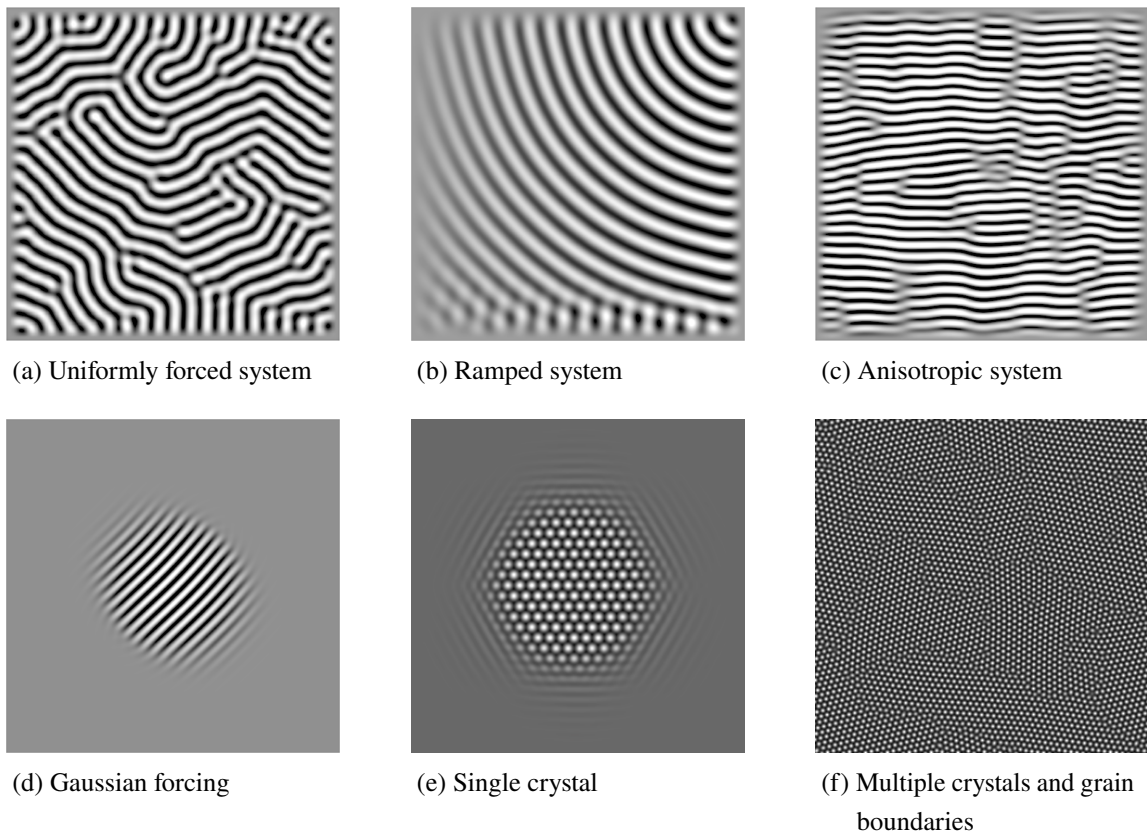
Source: Original work by the author, 2020.

The main objective of the thesis is to address what is the preferred orientation of stripes in a nonuniformly forced system using Swift-Hohenberg dynamics (both analytically and numerically). A second goal of this work is to provide a stable and easily adaptable splitting scheme framework for the nonuniformly forced SH3 and SH35 equations that strictly respects the Lyapunov functional ("free energy") decay.

This thesis is organized as follows:

Chapter 1 covers the relevant works addressing orientation effects due to control parameter gradient in Swift-Hohenberg dynamics, found in the literature.

Chapter 2 contains the mathematical formalism regarding the Swift-Hohenberg equation and its features. The linear stability analysis is able to show some of these features, but the nonlinear behavior is better explained by the amplitude equation formalism in the weakly nonlinear

regime. The stability of horizontal and vertical stripes orientation is addressed and discussed for the respective considerations.

Chapter 3 introduces the numerical framework of the thesis. A semi-implicit finite-difference scheme, with second order accuracy in time and space, is reviewed and extended for the quadratic-cubic and cubic-quintic Swift-Hohenberg equations. The scheme strictly respects the Lyapunov functional monotonic decay, which is expected for the considered relaxational dynamics.

Chapter 4 contains the verification of the code implementation for numerically solving the SH equation. For this purpose, a scheme stability and a convergence analysis are performed, and the scheme is shown to be stable and second order accurate in space.

Chapter 5 show the numerical results obtained for the Swift-Hohenberg equation. The two-dimensional simulations account for bulk, boundary and geometric effects involved in 'real' systems, and complement the analytical predictions derived in chapter 2.

Supplemental materials and informations are provided in the appendices as indicated throughout the thesis.

1 LITERATURE REVIEW

The Swift-Hohenberg (SH) equation (SWIFT; HOHENBERG, 1977) is a widely accepted mathematical framework for modeling pattern formation in many physical systems presenting symmetry breaking instabilities. A classical example where this symmmetry breaking occurs is found in the emergence of convection stripes in a thin layer of fluid heated from below, illustrated in Fig. 4a below:

Figure 4 - Rayleigh-Bénard convection rolls scheme.

(a) Experimental set-up

(b) Neutral stability curve
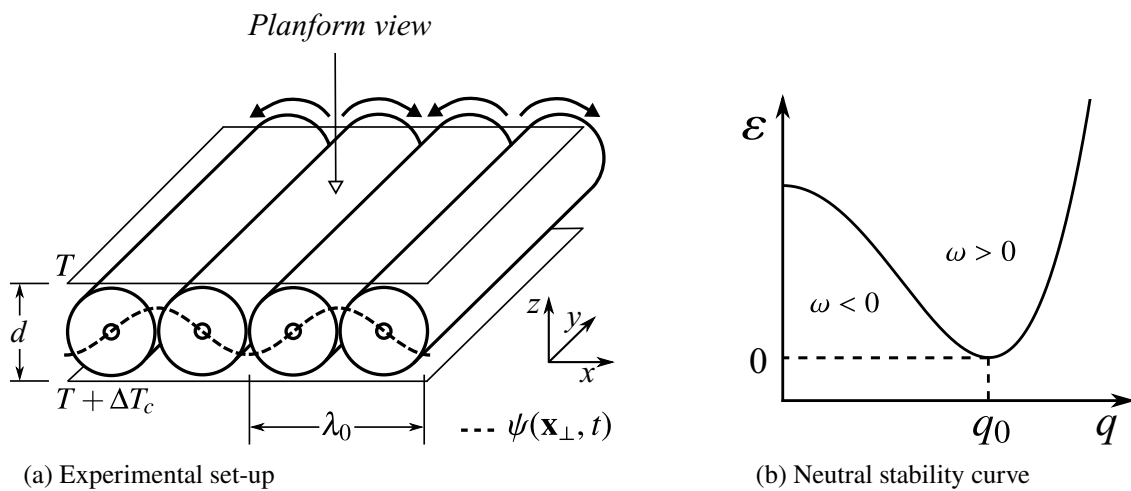
Source: Original work by the author.

Since there is a density gradient between the top and the bottom plates, the cooler (denser) liquid is pulled from top to bottom due to the gravitational force, which is opposed by the viscous damping force in the fluid. The balance of these two forces can be expressed by a dimensionless group known as the Rayleigh number (Ra), defined as:

$$Ra = \frac{\beta g |\Delta T| d^3}{\alpha \nu} \tag{1}$$

where the properties of the fluid are: β, the coefficient of thermal expansion; α, the diffusivity coefficient; and ν, the cinematic viscosity. The gravitational acceleration is denoted by g, and d is the distance between the two plates (or the height of the fluid layer). Whenever the temperature gradient, $|\Delta T|$, exceeds a critical value, $|\Delta T_c|$, i.e. $Ra \geqslant Ra_c$, the conductive profile turns into the convective profile (Rayleigh instability). Therefore, a pattern of rolls (or stripes) is observed from the planform view, illustrated in Fig. 4a. Several experimental works introduce a control (bifurcation) parameter to mesaure the distance of the system from the onset of instability, commonly denoted as $\varepsilon = |\Delta T|/|\Delta T_c| - 1$. This is equivalent to the definition used in many theoretical works, $\varepsilon = (Ra - Ra_c)/Ra_c$, which is more convenient considering the scope of the present work. In the vicinity of the instability, a control parameter greater than zero ($\varepsilon > 0$)

defines a bandwidth of wavenumbers close to the critical one, q_0, for which the linear growth is positive. Therefore, the spacing between the emerging rolls (or stripes) is also close to the critical wavelength, $\lambda_0 = 2\pi/q_0$. This feature is illustrated in the Fig. 4b.

The classical mathematical approach for describing the emergence of convection rolls consists of the Oberbeck-Boussinesq (OB) equations, and is outlined in appendix A following some classic literature (CHANDRASEKHAR, 1961; SWIFT; HOHENBERG, 1977; HAKEN, 1981; PONTES et al., 2018).

Swift and Hohenberg (1977) addressed the instability mechanism underlying Rayleigh-Bénard convection, proposing a simplified model, and also pointed out analogies with Brazovskii's model (BRAZOVSKII; DMITRIEV, 1975), for studying the condensation of a liquid (disordered phase) to a nonuniform state (periodic).. They derived a nonlinear equation for a scalar field, $\psi \equiv \psi(\mathbf{x}_\perp, t)$, where $\mathbf{x}_\perp = (x, y)$, that holds on the onset of Rayleigh instability and captures the main features from the full dynamics. This scalar field is considered an order parameter as it characterizes the transition from the uniform to the nonuniform (periodic) state. In order to achieve this, they considered a reduction of the full dynamics, led by the OB equations, to the slow modes dynamics, on the onset of instability, $Ra \sim Ra_c$. Considering the order parameter ψ, the two-dimensional SH equation describing dynamics in the vicinity of this transition can be expressed as:

$$\frac{\partial \psi}{\partial t} = \varepsilon\psi - \left(\nabla_\perp^2 + q_0^2\right)^2 \psi - \psi^3 . \tag{2}$$

where the Laplacian operator in the horizontal dimensions is: $\nabla_\perp^2 = \partial_x^2 + \partial_y^2$. It's clear that the trivial solution, $\psi \equiv 0$, and the periodic solution correspond to the uniform and nonuniform states, respectively. The periodic solution displays a stripe pattern with a wavenumber close to q_0 for small ε, according with the linear growth rates given by the dispersion relation, in Fourier space, $\omega = \varepsilon - (q^2 - q_0^2)^2$. The SH equation admits a Lyapunov functional or a 'free energy' potential in the form

$$\mathcal{F} = \int_\Omega d\mathbf{x} \frac{1}{2} \left\{ -\varepsilon\psi^2 + \left[\left(\nabla^2 + q_0^2\right)\psi\right]^2 - \frac{1}{2}\psi^4 \right\} , \tag{3}$$

and is derived by taking the variational derivative of Eq. 3 in L^2 norm,

$$\frac{\partial \psi}{\partial t} = -\frac{\delta\mathcal{F}}{\delta\psi} . \tag{4}$$

In many cases, it is possible to derive a similar dynamical equation from a potential, which leads to a relaxational gradient dynamics that has been explored in materials science and soft matter. This potential is often associated with the system's energy, allowing for non-local diffusive dynamics, pattern selection and emergence of dissipative structures. In this context, the SH model is part of the phase-field theory, which originates from statistical mechanics principles, and whose goal is to obtain governing equations for an order parameter evolution

(e.g. composition, some microstructural feature); it connects thus thermodynamic and kinetic properties with *microstructure* via a mathematical formalism (PROVATAS et al., 2005; ELDER et al., 2002; ELDER; GRANT, 2004).

An extension of the original Swift-Hohenberg equation (SH3) consists in adopting a destabilizing cubic term and in adding a quintic one. The resulting quintic equation (SH35) admits the coexistence of stable uniform and structured solutions, so that localized patterns may exist under a uniform control parameter (SAKAGUCHI; BRAND, 1996; BURKE; KNOBLOCH, 2006). This becomes a desirable physical feature in systems that allow for the coexistence of phases of distinct symmetry (VITRAL; LEO; VIÑALS, 2019). While localized states have been extensively studied through SH35, such states can also appear as solutions for SH3 and SH23. The issue for SH3 is that at the Turing point, $\varepsilon = 0$, we have a supercritical bifurcation representing the transition from trivial to modulated solutions. This means that the amplitude of the stripes emerging at $\varepsilon > 0$ increases with ε, and coexistence between the stripes and the trivial solution is not possible under uniform forcing. However, by allowing a spatial dependency on the control parameter ε, localized states become possible by varying ε between values above and below the Turing point. In turn, this poses the question of what are the consequences of control parameter gradients to pattern selection. While such gradients have been known to induce pattern orientation, we here propose a comprehensive numerical study of these orientation effects, how they affect state localization, and how does gradient orientation fare against other competing orientation effects.

Though extensively used for the study of nonequilibrium pattern formation, not many works are found before the turn of the century, addressing the orientation effect of gradients on a structure of stripes. One of the pioneers in the subject was Walton (1983)(WALTON, 1983), who considered the onset of convection in the Rayleigh-Bénard problem, with stress-free upper and lower surfaces, and perfect insulating sidewalls. Walton assumed a Rayleigh number weakly above the critical value at one of the sidewalls, and monotonically decreasing towards the bulk of the convection cell. Two cases were identified: if the hotter sidewall[1] was mantained sufficiently above the critical temperature a structure of stripes perpendicular to the sidewall appears. The result was latter confirmed by the theoretical works of Cross (1982)(CROSS, 1982a; CROSS, 1982b) and several others (CROSS; HOHENBERG, 1993; GREENSIDE; COUGHRAN, 1984; MANNEVILLE, 1990). On the opposite, if the hotter sidewall was mantained slightly above or below the critical temperature, a week structure of stripes parallel to the walls emerges. The existence of this weak structure had already been noted by the experimental work of Sruljes (1979)(SRULJES, 1970). However, the following step, concerning the interaction of the subcritical stripes with a supercritical structure, in the case where a positive horizontal gradient of temperaure is imposed, was not accomplished. One of the purposes of the present thesis consists

---

[1] The side corresponding to a greater value of the control parameter, ε

in mathematically analyzing this problem.

At the end of the eighties and the beginning of the nineties a group at the Free University of Brussels, pointed to the tendency of stripes to align to the gradient of the control parameter and also, to competing effects that, in many cases, dominate the orientation tendency created by the gradient (PONTES, 1994; PONTES; WALGRAEF; CHRISTOV, 2008). A coexistence between hexagons with opposite phases, and between hexagons with stripes perpendicular to the gradient of the control parameter was identified by Hilali *et al.* (1995)(HILALI et al., 1995), using a Swift-Hohenberg equation with a quadratic term. Malomed & Nepomnyashchy (1993)(MALOMED; NEPOMNYASHCHY, 1993) showed that the Lyapunov functional associated with a Newell-Whitehead-Segel equation governing the evolution of a structure of stripes depends on the angle between the stripes and the gradient. These authors showed that the Lyapunov potential is minimized whenever the stripes are parallel to the gradient and attain a maximum when perpendicular to it. More recently, Hiscock & Megason (2015)(HISCOCK; MEGASON, 2015) considered the orientation of stripe patterns in biological systems, using the Swift-Hohenberg equation. They derived Ginzburg-Landau type equations for the amplitudes of a structure of two perpendicular modes, one of them being oriented along the direction of gradient. Analytically, the steady state amplitude of both modes was perturbed and it was found that the mode with stripes perpendicular to gradient is unstable, and the resulting structure is made of stripes parallel to the gradient. In addition, these authors added a reaction term to the Swift-Hohenberg equation and found patterns of stripes perpendicular to the gradient of the control parameter. Only periodic boundary conditions (PBC) were considered by the authors.

The present thesis extends Hiscock and Megason's work. We initially address the orientation effect of the gradient of the control paramenter, in absence of other competing effects. We show that whenever a preexisting structure of stripes perpendicular to the gradient is perturbed in the direction of the gradient, the original structure becomes unstable, and is eventually replaced by stripes parallel to the gradient. The analysis was made using weakly nonlinear theory, from which we derive a pair of Newell-Whitehead-Segel equations. In sequence, we report the results of our numerical simulations with the SH equation with different nonlinearities, in presence of nonuniform forcings. Forcings were assumed in the form of spatial ramps, sinusoidal and gaussian distributions of the control parameter. We considered Generalized Dirichlet (GDBC) and Periodic Boundary conditions (PBC), and the cubic (SH3), quadratic-cubic (SH23) and cubic-quintic versions (SH35) of the Swift-Hohenberg equation. While we investigate orientation effects due to local nonlinearities outside the forcing term, there is also a recent interest (MORGAN; DAWES, 2014) on the nonlocal terms that could introduce a new lengthscale into the problem (short or long-ranged). These nonlocal nonlinearities significantly modify the coefficients of the amplitude equations, and open the opportunity for future studies on their effects for pattern selection and orientation in two-dimensional systems.

The analytical results from the weakly nonlinear analysis are compared with the numerical experiments. Now, due to restriction on finite or periodic domain, the gradient faces the competing

effect of other bulk and the boundaries effects, as well as possible discontinuities of ε (e.g. ramp in a periodic domain).

Competing bulk effects appear in the level of forcing, and in the interaction with modes in all directions, either existing in pseudo-random initial conditions or generated by the nonlinearity of the dynamics. If the forcing is sufficiently high, patterns with a high density of defects emerge and dominate the orientation effect of the gradient. Another bulk effect appears in nonuniform forcings, when $\varepsilon = 0$ somewhere in the domain. This situation occurs, for example, in configurations of the control parameter resulting in domains where both subcritical and supercritical regions coexist. In this case, the coherence length of the structure, $\xi \sim \varepsilon^{-1/2}$, diverges at $\varepsilon = 0$, making the domain "short", in the sense of that critical regions are affected by the boundaries, no matter how far they are.

Boundary effects consist of the well known tendency of stripes to approach supercritical sidewalls perpendicularly to walls (CROSS, 1982a; CROSS, 1982b; GREENSIDE; COUGHRAN, 1984; CROSS; HOHENBERG, 1993; MANNEVILLE, 1990), and of the less known effect of approaching subcritical sidewalls in parallel to the walls (WALTON, 1982; WALTON, 1983; PONTES; WALGRAEF; CHRISTOV, 2008). We call this last one by *subcritical boundary effect* or *subcritical effect* for short.

Though none of these competing effects are taken into account in the weakly nonlinear analysis, they can be investigated by a complementary numerical study. There are many works presenting fruitful numerical frameworks for the Swift-Hohenberg equation. In the beginning of this endeavor, Greenside and Coughran (1984) achieved relevant results through a finite differences approach by using a backward Euler time-integration scheme with rigid (CROSS, 1982b; CROSS, 1982a) and periodic boundary conditions (PBC). Those types of boundary conditions were also explored by Manneville (1990) and Cross and Hohenberg (1993). These works considered uniform control parameters. Other authors employed nonuniform distributions (ramps and gaussians) for the control parameter and presented very interesting results as well, displaying rich competition between bulk and boundary effects. A ramped control parameter mostly appears in the context of rigid boundaries (CHRISTOV et al., 1997; PONTES; WALGRAEF; CHRISTOV, 2008), which will be addressed here as rigid, or Generalized Dirichlet boundary conditions (GDBC), following Christov et al. (1997), Christov and Pontes (2002), Pontes, Walgraef and Christov (2008).

The SH model has a potential form such that we can associate its dynamics to a free energy functional, usually called the Lyapunov functional. In the last years, this potential nature has been explored in the materials science framework as a physical feature associated with the system's free energy and can be related to the description of materials patterning. In this context, the SH model is part of the phase-field theory, which was developed from statistical mechanics principles, and whose goal is to obtain governing equations for microstructure evolution; it connects thus thermodynamic and kinetic properties with microstructure via a mathematical formalism (PROVATAS; ELDER, 2010; PROVATAS et al., 2005; ELDER et al., 2002; ELDER;

GRANT, 2004). The phase-field theory is a descendant of the van der Waals, Cahn-Hilliard and Landau type classical field theoretical approaches, originating from a single order parameter gradient theory of Langer (LANGER; MÜLLER-KRUMBHAAR, 1978; LANGER, 1980). In the phase-field theory, the local state of matter is characterized by an order parameter $\psi(\mathbf{x}, t)$, called the phase-field variable, which monitors the transition between phases of distinct order of property. It can represent the structural order parameter that measures local crystallinity, the composition of a phase, the degree of a molecular ordering, etc. In the case of the phase-field crystal (PFC) approach, a conserved dynamics is assumed for this order parameter. Although this formalism will not be addressed in this paper, it is worth mentioning that many interesting numerical works explored the SH equation in a PFC framework (ELSEY; WIRTH, 2013; LEE; KIM, 2016; LI; KIM, 2017).

Spectral methods have become largely used due to their highly spatial accurate solutions (LEE, 2019; VITRAL; LEO; VIÑALS, 2019; WANG; ZHAI, 2020). They usually treat the nonlinear terms explicitly in the physical space and therefore are called pseudo-spectral methods. Fully explicit schemes leads to severe stability restrictions on the time step, because of the fourth-order nonlinear partial differential equation originated from the non-conserved dynamics. In the case of the phase-field crystal (PFC) approach (conserved dynamics), one derives a six-order nonlinear partial differential equation, which is even more restrictive for the time step selection. While PFC is not a subject of this work, our proposed scheme can be readily translated into a numerical framework for many PFC problems.

The present work is also a continuation of the work presented by Christov and Pontes (2002) where those authors employed a finite differences scheme originally introduced by Douglas & Rachford in the framework of the temperature equation, for solving the cubic Swift-Hohenberg equation (SH3) in two dimensions, with uniform forcing, GDBC, and strict implementation of the associated functional. The scheme is known as Stabilizing Correction (DOUGLAS; RACHFORD., 1956; YANENKO; HOLT, 1971). Here, we expand this study for additional nonlinearities, boundary conditions and a spatially dependent control parameter. This includes the quintic version of the Swift-Hohenberg equation (SH35) with both GDBC and PBC, nonuniform gaussian distributions of the control parameter in addition to ramps, and also a strict implementation of the associated Lyapunov functional. The scheme features a semi-implicit time splitting with second order representation of time and space derivatives. Some other works also used stabilizing correction scheme for similar fourth-order nonlinear differential equations, such as the anisotropic damped Kuramoto-Sivashinsky equation (VITRAL et al., 2018).

2 MATHEMATICAL MODELING

2.1 The Swift-Hohenberg equation

The SH equation has the so-called gradient dynamics, which means there is a potential, known as a Lyapunov functional, $\mathcal{F} \equiv \mathcal{F}[\psi]$, associated with the order parameter field $\psi(\mathbf{x}, t)$ that has the property of decreasing monotonically during the evolution (SWIFT; HOHENBERG, 1977; CROSS, 1982b; GREENSIDE; COUGHRAN, 1984; CROSS; HOHENBERG, 1993; CHRISTOV; PONTES, 2002). It can be derived by using the L^2-gradient flow of the Lyapunov energy functional:

$$\mathcal{F} = \int_{\Omega} d\mathbf{x} \frac{1}{2} \left\{ -\varepsilon(\mathbf{x})\psi^2 + \alpha \left[\left(\nabla^2 + q_0^2 \right) \psi \right]^2 - \frac{2\zeta}{3}\psi^3 - \frac{\beta}{2}\psi^4 + \frac{\gamma}{3}\psi^6 \right\}, \tag{5}$$

$$\frac{\partial \mathcal{F}}{\partial t} = -\int_{\Omega} d\mathbf{x} \left(\frac{\partial \psi}{\partial t} \right)^2 \leqslant 0, \tag{6}$$

where Ω represents the domain whose size is commensurate with the length scales of the patterns. We consider a regular domain $\Omega : \{x \in [0, L_x], y \in [0, L_y]\}$. As discussed, ε is a control parameter (forcing) that measures the distance from the onset of instability, and it may present a spatial dependency. The constants ζ, β and γ control the energy structure of the system, which describes the energy of phases of distinct symmetry and their stability (with implications to the bifurcation diagram). The constant α may present different physical interpretations (e.g. elastic constant), but it is typically scaled to $\alpha = 1$. Also, Eq. 6 denotes the nonincreasing behaviour of the Lyapunov functional, which monotonically decreases until steady state is reached (CHRISTOV; PONTES, 2002). By taking the variational derivative of Eq. 5 in L^2 norm, the following Swift-Hohenberg equation is obtained:

$$\frac{\partial \psi}{\partial t} = -\frac{\delta \mathcal{F}}{\delta \psi}, \tag{7}$$

$$\frac{\partial \psi}{\partial t} = \varepsilon(\mathbf{x})\psi - \alpha \left(\nabla^2 + q_0^2 \right)^2 \psi + \zeta\psi^2 + \beta\psi^3 - \gamma\psi^5. \tag{8}$$

Choosing different values for ζ, β and γ, we obtain the SH3, SH23 and SH35 equations, which we numerically solve in two dimensional square domains, i.e.', computational domains $\Omega = [0, L]^2$, where L is the domain length.We adopted Generalized Dirichlet Boundary Conditions (GDBC), and Periodic Boundary Conditions (PBC) $\psi = \nabla\psi \cdot \mathbf{n} = 0$ (on $\partial\Omega$) and $\psi(\mathbf{x}) = \psi(\mathbf{x} + \mathbf{x}_L)$ ($\forall \mathbf{x} \in \Omega$), respectively, where $\mathbf{x}_L = (L_x, L_y)$.

Figure 5 - Parameters assumed for the governing equations studied in this work.

Equation	Nonlinearity	α	β	γ	ζ	q_0
SH23	quadratic-cubic	1	-1	0	±1	1
SH3	cubic	1	-1	0	0	1
SH35	cubic-quintic	1	1	1	0	1

Source: Original work by the author.

By analyzing the polynomials from the Lyapunov functional, we can define a function of ψ,

$$F = -\frac{\varepsilon}{2}\psi^2 - \frac{\zeta}{3}\psi^3 - \frac{\beta}{4}\psi^4 + \frac{\gamma}{6}\psi^6 \tag{9}$$

and plot it in a range of the order parameter. The obtained curves shown in Fig. 6 allows us to observe that for a $\varepsilon > 0$, the periodic phase is favoured, and otherwise ($\varepsilon \leqslant 0$), the uniform phase ($\psi \equiv 0$) prevails.

Figure 6 - Potential from the Lyapunov functional for the following parameters: $(\zeta, \beta, \gamma) = (0, -1, 0)$.
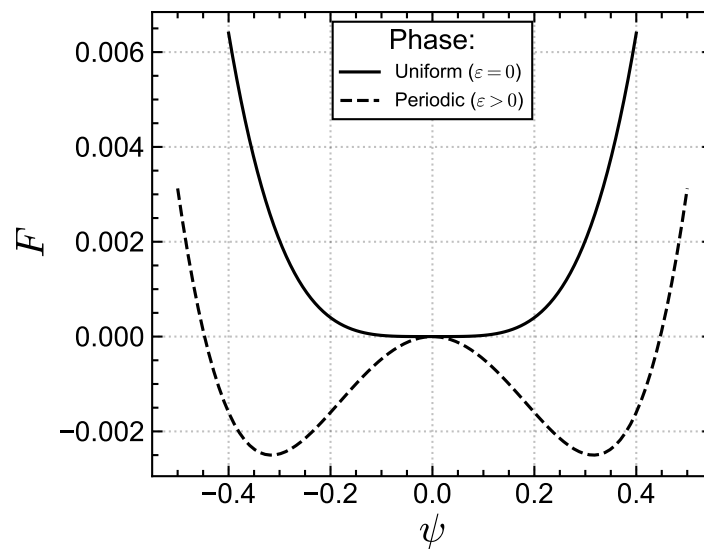
Source: Original work by the author.

The phase transition from uniform state to a periodic state appears in many physical systems (LANDAU; LIFSHITZ, 1980), specially in materials science, where it's usually addressed as crystallization (formation of a highly organized solid from liquid) in the Phase Field Crystal (PFC) framework (ELDER et al., 2002; ELDER; GRANT, 2004; PROVATAS; ELDER, 2010), for example.

2.2 Linear stability analysis

For simple purposes, the linear stability analysis of the uniformly forced SH3 equation is carried out in this section (CROSS, 2009). We denote the base state solution as ψ_b, and define the original order parameter field as

$$\psi(\mathbf{x}, t) = \psi_b + \psi_p(\mathbf{x}, t),\tag{10}$$

where ψ_p is the perturbation field. The original equation can be cast in form:

$$\frac{\partial \psi}{\partial t} = \hat{N}[\psi],\tag{11}$$

where the nonlinear operator $\hat{N}$ is defined by considering the right-hand side of Eq. (8) to be a function of the field ψ, such that

$$\hat{N}[\psi] = \varepsilon\psi - \alpha\left(\nabla^2 + q_0^2\right)^2\psi + \beta\psi^3.\tag{12}$$

where $\alpha = 1$, and $\beta = -1$, typically. In order to obtain an equation for the perturbation ψ_p, we linearize the nonlinear operator $\hat{N}$ by taking its Taylor expansion up to first order only (truncating at second order), around ψ_b:

$$\hat{N}[\psi_b + \psi_p] = \hat{N}[\psi_b] + \left.\frac{\delta\hat{N}}{\delta\psi}\right|_{\psi_b}\psi_p.\tag{13}$$

Since $\hat{N}[\psi_p] = \hat{N}[\psi_b + \psi_p] - \hat{N}[\psi_b]$, we have that

$$\frac{\partial \psi_p}{\partial t} = \left.\frac{\delta\hat{N}}{\delta\psi}\right|_{\psi_b}\psi_p,\tag{14}$$

where

$$\left.\frac{\delta\hat{N}}{\delta\psi}\right|_{\psi_b} = \varepsilon - \left(\nabla^2 + q_0^2\right)^2 - 3\psi_b^2.\tag{15}$$

Assuming the particular case where the base state is uniform $\psi_b = 0$, and that the perturbation depends on time and space as

$$\psi_p(\mathbf{x}, t) = A\exp(\omega t - i\mathbf{q} \cdot \mathbf{x}),\tag{16}$$

we readily obtain

$$\omega(q) = \varepsilon - \left(q^2 - q_0^2\right)^2\tag{17}$$

Figure 7 - Linear stability analysis of the Swift-Hohenberg equation.
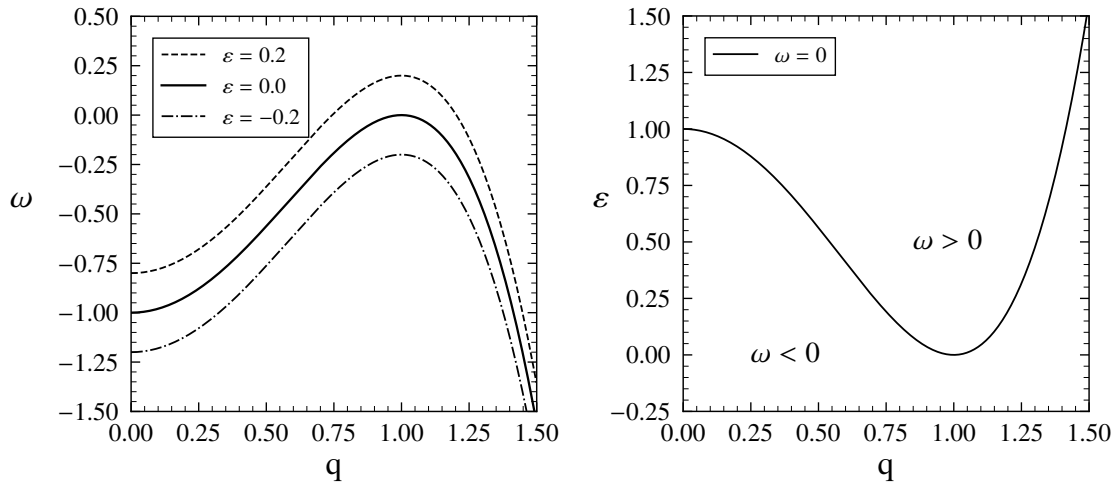
(a) Linear growth rate.

(b) Neutral stability curve.

Source: Original work by the author.

where $\omega(q)$ corresponds to the linear growth rate associated with mode $\mathbf{q}$ for a particular set of the parameters ε, α, and the fundamental wavenumber q_0. A plot of the linear growth rate as a function of q modes is illustrated in Fig.7a, and the neutral stability curve, corresponding to $\omega = 0$ is plotted n Fig.7b.

2.3 **Weakly nonlinear analysis**

The stability of preexisting patterns can be investigated through the amplitude equations derived from the Swift-Hohenberg equation. These equations describe the motion of the amplitude that envelopes the oscillating order parameter ψ, and from this coarse-grained description we can evaluate how perturbations evolve depending on the orientation of the initial pattern and of the gradient of the control parameter (MANNEVILLE, 1990; CROSS; HOHENBERG, 1993; HOYLE, 2006). Since the derivation of the amplitude equations is relatively similar for SH3, SH23 and SH35, in terms of scaling and considerations between coefficients, we will only provide derivation details for the SH3 case ($\zeta = \gamma = 0$). The SH3 has the form

$$\frac{\partial \psi}{\partial t} \psi \;=\; \varepsilon \psi - \alpha \, (\nabla^2 + q_0^2)^2 \psi + \beta \, \psi^3 \tag{18}$$

where $\beta < 0$ and $\alpha > 0$ (generally $\alpha = 1$).

The solution for a two-dimensional stripe or square pattern can be written in terms of a superposition between a sinusoidal function in x and another in y

$$\psi(\mathbf{x}, t) \;=\; A(\mathbf{x}, t) \, e^{i q_0 x} + B(\mathbf{x}, t) \, e^{i q_0 y} + c.c.$$

where A and B are complex amplitudes. To perform a multiscale expansion, we introduce slow variables $\{X, Y, T\}$ which are distinct from the fast variables $\{x, y, t\}$. The amplitudes are modulated along the slow variables as $A(X, Y, T)$ and $B(X, Y, T)$, while oscillation of the order parameter in the vicinity of the fundamental wavevector of the pattern, $\mathbf{q}_0$, lie in the scale of the fast variables.

Assume we have an initial pattern of perfectly aligned stripes in the x direction, that is, stripes presenting a wavenumber $\mathbf{q}_0 = q_0 \mathbf{j}$ (unit vector in the y direction). By introducing small perturbations to the wavenumber in Eq. 18, such as $q = q_0 + \delta q_y$ and comparing terms, we find that for consistency the slow variables should scale as

$$X = \varepsilon^{1/4} x, \quad Y = \varepsilon^{1/2} y, \quad T = \varepsilon t \, .$$

From this scaling, we note that derivatives in Eq. 18 should follow the chain rule accounting for slow and fast variables, so that

$$\partial_x \to \varepsilon^{1/4} \, \partial_X \, , \quad \partial_y \to \partial_y + \varepsilon^{1/2} \, \partial_Y \, , \quad \partial_t \to \varepsilon \, \partial_T \, . \tag{19}$$

For small ε, the order parameter ψ can be expanded about the trivial solution as

$$\psi \;=\; \varepsilon^{1/2} \, \psi_1 + \varepsilon \, \psi_2 + \varepsilon^{3/2} \, \psi_3 + \dots$$

By substituting the expanded ψ into Eq. 18 with derivatives acting in multiple scales as defined in Eq. 19, we are able to collect terms from SH3 in powers of ε. This way, we obtain equations from each order of ε that should be independently satisfied, from which we can derive the functions ψ_i and the equations governing the evolution of $A(X, Y, T)$ and $B(X, Y, T)$. At orders $O(\varepsilon^{1/2})$ and $O(\varepsilon)$, using the notation $L_c = (\nabla^2 + \mathbf{q}_0^2)^2$, we find

$$O(\varepsilon^{1/2}): \ L_c\psi_1 = 0 \Rightarrow \psi_1 = B_{11} e^{iq_0y} + c.c., \ A_{11} = 0$$

$$O(\varepsilon): \ L_c\psi_2 + L_c\psi_1 = 0 \Rightarrow \psi_2 = B_{21} e^{iq_0y} + c.c., \ A_{21} = 0$$

The contribution from the nonlinear cubic term appears starting from the next order. This term expands as

$$\psi^3 = \varepsilon^{3/2}\psi_1^3 + 3\varepsilon^2\psi_1^2\psi_2 + 3\varepsilon^{5/2}(\psi_1^2\psi_3 + \psi_1\psi_2^2) + \dots,$$

and ψ_1 expand as

$$\psi_1^3 = B_{11}^3 e^{3iq_0y} + 3B_{11}^2 e^{2iq_0y}B_{11}^* e^{-iq_0y} + 3B_{11} e^{iq_0y}(B_{11}^*)^2 e^{-2iq_0y} + (B_{11}^*)^3 e^{-3iq_0y}.$$

Therefore, at order $O(\varepsilon^{3/2})$ we find

$$L_c\psi_3 = (-\partial_T + 1 + 4\alpha q_0^2\partial_Y^2 - \alpha\partial_X^4 - 4i\alpha q_0\partial_Y\partial_X^2 + 3\beta|B_{11}|^2)B_{11}e^{iq_0y} + (\dots)e^{i3q_0y} + c.c.$$

By rewriting Eq. 20 as $L_c\psi_3 = \theta$, the solvability condition associated to this equation is that θ must be perpendicular to the null space of L_c^*: $\theta \perp g \in Nu(L_c^*)$. This is the Fredholm's Alternative, the condition under which the inner product $(\theta, g) = (\psi, L_c^*g) = 0$ is satisfied, and the implication for Eq. 20 is that the right-hand side must be orthogonal to the eigenfunctions e^{iq_0y}, and e^{-iq_0y}. Therefore, by enforcing solvability we obtain the amplitude equation for $B_{11}(X, Y, T)$,

$$\partial_T B_{11} = B_{11} + \alpha(2q_0\partial_Y - i\partial_X^2)^2B_{11} + 3\beta|B_{11}|^2B_{11}.$$

We can similarly find the amplitude equation for $A(X, Y, T)$. Since $A_{11} = A_{21} = 0$, we need to gather terms up to order $O(\varepsilon^{5/2})$, so that from the Fredholm's Alternative we obtain,

$$\partial_T A_{31} = A_{31} + \alpha(2q_0\partial_Y - i\partial_X^2)^2A_{31} + 6\beta|B_{11}|^2A_{31}.$$

In order to rewrite these amplitude equations in terms of the original variables, we first note that both amplitudes A and B can be expanded in the same form as ψ, that is

$$A = \varepsilon^{3/2}A_{31} + \varepsilon^2A_{41} + \dots,$$

$$B = \varepsilon^{1/2}B_{11} + \varepsilon B_{21} + \dots$$

Therefore, accounting for the possibility of a control parameter with spatial dependence, the pair of amplitude equations for the two-dimensional SH3 with stripes perpendicular to the y direction is

$$\partial_t A = \varepsilon(\mathbf{x})A + \alpha(2q_0\partial_y - i\partial_x^2)^2 A + 6\beta|B|^2 A , \tag{20}$$

$$\partial_t B = \varepsilon(\mathbf{x})B + \alpha(2q_0\partial_y - i\partial_x^2)^2 B + 3\beta|B|^2 B . \tag{21}$$

That is, we obtain a system of coupled Newell-Whitehead-Segel (NWS) equations (MALOMED; NEPOMNYASHCHY, 1993).

The amplitude equations allow us to evaluate a preexisting pattern stability in the presence of perturbations, and the role played by $\nabla\varepsilon$ in such stability. Note that while A and B are complex amplitudes, it can be shown that the phase becomes a constant for steady state solutions of parallel stripes (MANNEVILLE, 1990), so that we focus on the equation for the real part of the amplitude in the following analysis.

Assume $\varepsilon = \varepsilon(x)$ is an increasing ramp in x only, and that stripes are initially perpendicular to y, with a steady state amplitude $A_0 = 0$. The steady real amplitude B_0 satisfies

$$\varepsilon(x)B_0 - \alpha\partial_x^4 B_0 + 3\beta B_0^3 = 0 .$$

Away from the Turing point ($\epsilon = 0$), the steady state solution is approximately

$$B_0 \approx \left(\frac{\varepsilon(x)}{-3\beta}\right)^{1/2} .$$

By introducing small perturbations δA and δB to the steady state solutions, we find from Eqs. 20 and 21 that these perturbations evolve as

$$\partial_t(\delta A) = -\varepsilon(x)\delta A + \alpha(4q_0^2\partial_y^2 - \partial_x^4)\delta A$$

$$\partial_t(\delta B) = -2\varepsilon(x)\delta B + \alpha(4q_0^2\partial_y^2 - \partial_x^4)\delta B.$$

Since the existence of the solution ($A_0 = 0, B_0$) requires $\varepsilon > 0$, this implies that when stripes are parallel to $\nabla\varepsilon$, the solution $(0, B_0)$ is stable with respect to small perturbations δA and δB.

For the case of stripes perpendicular to the $\nabla\varepsilon$, we keep the ramp $\varepsilon(x)$ in the x direction but change the preexisting pattern to stripes aligned in the y direction. The consequence to Eqs. 20 and 21 is that A, B and space derivatives swap, and the following coupled NWS equations are found

$$\partial_t A = \varepsilon(\mathbf{x})A + \alpha(2q_0\partial_x - i\partial_y^2)^2 A + 3\beta|A|^2 A , \tag{22}$$

$$\partial_t B = \varepsilon(\mathbf{x})B + \alpha(2q_0\partial_x - i\partial_y^2)^2 B + 6\beta|A|^2 B . \tag{23}$$

Therefore, now we have a steady state solution $B_0 = 0$ and $A_0 \neq 0$. Due to the $\partial_x^2 A$ derivative in Eq. 22, near the Turing instability at $\varepsilon = 0$, A_0 will not behave as $(\varepsilon(x)/-3\beta)^{1/2}$. The A_0 solution satisfying

$$\varepsilon(x)A_0 + 4\alpha q_0^2 \partial_x^2 A_0 + 3\beta A_0^3 \;\; = \;\; 0$$

should also satisfy boundary conditions $A_0(x = 0) = 0$ and $A(x \rightarrow \infty) = (\varepsilon(x)/-3\beta)^{1/2}$. Note that we set the Turing point at $x = 0$ for simplicity. For constant ε, the solution is of the type $A_0 \sim \sqrt{\varepsilon} \tanh(x\sqrt{\varepsilon}/2)$, which behaves as $A_0 \sim x\varepsilon$ for small x and ε. Since for $\varepsilon(x) = c\,x$, where c is a positive constant, there is no analytic solution A_0, so we assume that $A_0 \sim cx^2$ for small x.

For stripes perpendicular to the control parameter gradient, perturbations δB evolve as

$$\partial_t(\delta B) \;\; = \;\; (\varepsilon(x) + 6\beta|A|^2)\delta B \;. \tag{24}$$

Taking into account $\varepsilon(x) = cx$, $\beta < 0$ and $A_0 \sim cx^2$ for small x, we conclude the solution $(A_0, B_0 = 0)$ is unstable. Therefore, while stripes with wavevector $\mathbf{q}_0 \perp \nabla\varepsilon$ are stable with respect to small perturbations $(\delta A, \delta B)$, we find that stripes with $\mathbf{q}_0 \parallel \nabla\varepsilon$ are unstable in the vicinity of the Turing point.

In the following chapters, we address to the asymptotic height of the amplitude as

$$h \;\; = \;\; \left(\frac{\varepsilon(x)}{-3\beta}\right)^{1/2} \;. \tag{25}$$

This quantity, which appears from the weakly nonlinear analysis for the two studied orientation of stripes, will be addressed to as an analytical result, and used for comparison with the attained steady state amplitudes of the numerical results.

3 COMPUTATIONAL METHODOLOGY

3.1 **Governing equations**

The mathematical description of the dimensionless governing equations is briefly discussed in the beginning of this section. Then, the details of the numerical framework are exposed as an extension of Christov and Pontes (2002) work. For both SH3 and SH35 discretizations, a finite difference semi-implicit scheme of second order accuracy in time and space is presented. Finally, the choices for the operator splitting method, spatial discretizations and mesh types are clarified.

We expand Eq. 8 by considering the following Laplacian operator in cartesian coordinates: $\nabla^2 \equiv \partial^2/\partial x^2 + \partial^2/\partial y^2$, we have:

$$
\begin{aligned}
\frac{\partial \psi}{\partial t} &= \varepsilon(\mathbf{x})\psi - \alpha q_0^4 \psi - 2\alpha q_0^2 \nabla^2 \psi - \alpha \nabla^4 \psi + \zeta \psi^2 + \beta \psi^3 - \gamma \psi^5 \\
&= \varepsilon(\mathbf{x})\psi - \alpha q_0^4 \psi - 2\alpha q_0^2 \frac{\partial^2 \psi}{\partial x^2} - 2\alpha q_0^2 \frac{\partial^2 \psi}{\partial y^2} - \alpha \frac{\partial^4 \psi}{\partial x^4} - 2\alpha \frac{\partial^4 \psi}{\partial x^2 \partial y^2} - \alpha \frac{\partial^4 \psi}{\partial y^4} \\
&\quad + \zeta \psi^2 + \beta \psi^3 - \gamma \psi^5 \; .
\end{aligned} \tag{26}
$$

In the following sections, the time-stepping scheme ,and the spatial discretization implemented for discretizing Eq.(26) are addressed.

3.2 **The target scheme**

In order to construct a Crank-Nicolson second order in time numerical scheme, we adopt the following representation proposed by Christov and Pontes (2002) for the time derivative of Eq. 8, where the RHS is evaluated at the middle of the time step Δt. The updated scheme, now including a quintic term takes the form:

$$
\begin{aligned}
\frac{\psi^{n+1} - \psi^n}{\Delta t} &= \left[\varepsilon(\mathbf{x}) - \alpha q_0^4 - 2\alpha q_0^2 \frac{\partial^2}{\partial x^2} - 2\alpha q_0^2 \frac{\partial^2}{\partial y^2} - \alpha \frac{\partial^4}{\partial x^4} - 2\alpha \frac{\partial^4}{\partial x^2 \partial y^2} - \alpha \frac{\partial^4}{\partial y^4} \right. \\
&\quad \left. + \zeta \frac{\psi^{n+1} + \psi^n}{2} + \beta \frac{\left(\psi^{n+1}\right)^2 + (\psi^n)^2}{2} - \gamma \frac{\left(\psi^{n+1}\right)^4 + (\psi^n)^4}{2} \right] \left(\frac{\psi^{n+1} + \psi^n}{2} \right).
\end{aligned} \tag{27}
$$

The superscript $(n + 1)$ refers to the next time to be evaluated and n, to the current one. The parameter values for α, β, γ and q_0 are chosen according to Tab. 5.

The RHS terms of Eq. 27 are grouped in three parts, the first and the second ones containing the semi-implicit operators $\Lambda_x^{n+1/2}$ and $\Lambda_y^{n+1/2}$ that will act on the variable $\left(\psi^{n+1} + \psi^n\right)/2$, and a function $f^{n+1/2}$, evaluated at the middle of the time step Δt. This function will contain explicit terms only, in the final discrete form of Eq. 27. Space derivatives are represented by centered

second order formulæ. Implicit terms are chosen having in mind to construct negative definite operators that will assure the stability of the scheme. The factor $1/2$ multiplying $\left(\psi^{n+1} + \psi^n\right)$ in the RHS of the above equation is included in the operators $\Lambda_x^{n+1/2}$ and $\Lambda_y^{n+1/2}$, leading to the following target scheme:

$$\frac{\psi^{n+1} - \psi^n}{\Delta t} = \left(\Lambda_x^{n+1/2} + \Lambda_y^{n+1/2}\right)\left(\psi^{n+1} + \psi^n\right) + f^{n+1/2} \ . \tag{28}$$

For the SH23 ($\zeta = \pm 1$) and SH3 ($\zeta = 0$, $\beta = -1$) equations, the operators $\Lambda_x^{n+1/2}$, $\Lambda_y^{n+1/2}$ and $f^{n+1/2}$ are defined as:

$$\Lambda_x^{n+1/2} = \frac{1}{2}\left[-\alpha\left(\frac{\partial^4}{\partial x^4} + \frac{q_0^4}{2}\right) + \beta\frac{\left(\psi^{n+1}\right)^2 + \left(\psi^n\right)^2}{2}\right] \ ;$$

$$\Lambda_y^{n+1/2} = \frac{1}{2}\left[-\alpha\left(\frac{\partial^4}{\partial y^4} + \frac{q_0^4}{2}\right) + \beta\frac{\left(\psi^{n+1}\right)^2 + \left(\psi^n\right)^2}{2}\right] \ ; \tag{29}$$

$$f^{n+1/2} = \frac{1}{2}\left[\varepsilon(\mathbf{x}) - \alpha\left(2q_0^2\frac{\partial^2}{\partial x^2} + 2q_0^2\frac{\partial^2}{\partial y^2} + 2\frac{\partial^4}{\partial x^2\partial y^2}\right) + \zeta\frac{\psi^{n+1} + \psi^n}{2}\right]\left(\psi^{n+1} + \psi^n\right) \ ,$$

and for the SH35 ($\zeta = 0$, $\beta = 1$):

$$\Lambda_x^{n+1/2} = \frac{1}{2}\left[-\alpha\left(\frac{\partial^4}{\partial x^4} + \frac{q_0^4}{2}\right) - \gamma\frac{\left(\psi^{n+1}\right)^4 + \left(\psi^n\right)^4}{2}\right] \ ;$$

$$\Lambda_y^{n+1/2} = \frac{1}{2}\left[-\alpha\left(\frac{\partial^4}{\partial y^4} + \frac{q_0^4}{2}\right) - \gamma\frac{\left(\psi^{n+1}\right)^4 + \left(\psi^n\right)^4}{2}\right] \ ;$$

$$f^{n+1/2} = \frac{1}{2}\left[\varepsilon(\mathbf{x}) - \alpha\left(2q_0^2\frac{\partial^2}{\partial x^2} + 2q_0^2\frac{\partial^2}{\partial y^2} + 2\frac{\partial^4}{\partial x^2\partial y^2}\right) + \beta\frac{\left(\psi^{n+1}\right)^2 + \left(\psi^n\right)^2}{2}\right]\left(\psi^{n+1} + \psi^n\right) \ . \tag{30}$$

3.3 Internal iterations

Since the operators $\Lambda_x^{n+1/2}$, $\Lambda_y^{n+1/2}$ and the function $f^{n+1/2}$ in Eqs. 28, 29 and 30 contain implicit terms due to the time discretization and linearization of the nonlinear terms, we do internal iterations. They are required to secure the approximation of the nonlinearities in the scheme (Eq. 28) at each time step. The internal iterations scheme reads:

$$\frac{\psi^{n+1,p+1} - \psi^n}{\Delta t} = \left(\Lambda_x^{n+1/2,p} + \Lambda_y^{n+1/2,p}\right)\left(\psi^{n+1,p+1} + \psi^n\right) + f^{n+1/2,p} \ , \tag{31}$$

where the index (p) refers to the internal iteration number. The superscript $(n+1, p+1)$ identifies the new iteration, while (n) are the values of the previous time step. The superscript $(n+1)$ for

the nonlinear term in the function $f^{n+1/2}$ will be replaced by (n, p), which stands for the values obtained from the previous iteration.

The operators $\Lambda_x^{n+1/2,p}$, $\Lambda_y^{n+1/2,p}$ function $f^{n+1/2,p}$ are redefined as follows, for the SH3 equation:

$$
\begin{aligned}
\Lambda_x^{n+1/2,p} &= \frac{1}{2}\left[-\alpha\left(\frac{\partial^4}{\partial x^4} + \frac{q_0^4}{2}\right) - \beta\frac{\left(\psi^{n+1,p}\right)^2 + \left(\psi^n\right)^2}{2}\right], \\
\Lambda_y^{n+1/2,p} &= \frac{1}{2}\left[-\alpha\left(\frac{\partial^4}{\partial y^4} + \frac{q_0^4}{2}\right) - \beta\frac{\left(\psi^{n+1,p}\right)^2 + \left(\psi^n\right)^2}{2}\right], \\
f^{n+1/2,p} &= \frac{1}{2}\left[\epsilon(\mathbf{x}) - \alpha\left(2q_0^2\frac{\partial^2}{\partial x^2} + 2q_0^2\frac{\partial^2}{\partial y^2} + 2\frac{\partial^4}{\partial x^2\partial y^2}\right)\right]\left(\psi^{n+1,p} + \psi^n\right),
\end{aligned}
\tag{32}
$$

and for the SH35:

$$
\begin{aligned}
\Lambda_x^{n+1/2,p} &= \frac{1}{2}\left[-\alpha\left(\frac{\partial^4}{\partial x^4} + \frac{q_0^4}{2}\right) - \gamma\frac{\left(\psi^{n+1,p}\right)^4 + \left(\psi^n\right)^4}{2}\right], \\
\Lambda_y^{n+1/2,p} &= \frac{1}{2}\left[-\alpha\left(\frac{\partial^4}{\partial y^4} + \frac{q_0^4}{2}\right) - \gamma\frac{\left(\psi^{n+1,p}\right)^4 + \left(\psi^n\right)^4}{2}\right], \\
f^{n+1/2,p} &= \frac{1}{2}\left[\epsilon(\mathbf{x}) - \alpha\left(2q_0^2\frac{\partial^2}{\partial x^2} + 2q_0^2\frac{\partial^2}{\partial y^2} + 2\frac{\partial^4}{\partial x^2\partial y^2}\right)\right. \\
&\quad \left. +\beta\frac{\left(\psi^{n+1,p}\right)^2 + \left(\psi^n\right)^2}{2}\right]\left(\psi^{n+1,p} + \psi^n\right).
\end{aligned}
\tag{33}
$$

The iterations loop proceed until the following criterion for the L_∞ norm is satisfied with $\delta = 1.0 \times 10^{-8}$:

$$
L_\infty = \frac{\max \mid \psi^{n+1,p+1} - \psi^{n+1,p} \mid}{\max \mid \psi^{n+1,p+1} \mid} \leq \delta;
\tag{34}
$$

so that the last iteration gives the sought function ψ in the new time $\psi^{n+1} \equiv \psi^{n+1,p+1}$.

3.4 Stabilizing correction

Although employing sparse matrices for the operators, computationally solving Eq. 31 still represents a costly procedure. In order to reduce such computational effort and errors (from discretization and floating-point operations), the operators splitting method was adopted. The splitting of Eq. 28 is made according to the Douglas second scheme (also known as scheme of stabilizing correction, shown by (CHRISTOV et al., 1997),(CHRISTOV; PONTES, 2002)), and is briefly reviewed. The following equations represent a consistent approximation of the original

scheme:

$$\frac{\widetilde{\psi} - \psi^n}{\Delta t} = \Lambda_x^{n+1/2,p}\widetilde{\psi} + \Lambda_y^{n+1/2,p}\psi^n + f^{n+1/2,p} + (\Lambda_x^{n+1/2,p} + \Lambda_y^{n+1/2,p})\psi^n, \tag{35}$$

$$\frac{\psi^{n+1,p+1} - \widetilde{\psi}}{\Delta t} = \Lambda_y^{n+1/2,p}(\psi^{n+1,p+1} - \psi^n), \tag{36}$$

where $\widetilde{\psi}$ is an intermediary estimation of ψ at the new time step. In order to show that the splitting represents the original scheme, we rewrite Eqs. 35 and 36 in the form:

$$\left(E - \Delta t\Lambda_x^{n+1/2,p}\right)\widetilde{\psi} = \left(E + \Delta t\Lambda_x^{n+1/2,p}\right)\psi^n + 2\Delta t\Lambda_y^{n+1/2,p}\psi^n + \Delta t f^{n+1/2,p} \ ;$$

$$\left(E - \Delta t\Lambda_y^{n+1/2,p}\right)\psi^{n+1,p+1} = \widetilde{\psi} - \Delta t\Lambda_y^{n+1/2,p}\psi^n \ ;$$

where E is the unity operator. Rearranging these equations, the intermediate variable $\widetilde{\psi}$ is eliminated and the result may be rewritten as:

$$\left(E - \Delta t\Lambda_x^{n+1/2,p}\right)\left(E - \Delta t\Lambda_y^{n+1/2,p}\right)\psi^{n+1,p+1} = \left(E + \Delta t\Lambda_x^{n+1/2,p}\right)\psi^n + 2\Delta t\Lambda_y^{n+1/2,p}\psi^n +$$

$$+ \Delta t f^{n+1/2,p} - \left(E - \Delta t\Lambda_x^{n+1/2,p}\right)\Delta t\Lambda_y^{n+1/2,p}\psi^n \ .$$

This result may be rewritten as:

$$\left(E + \Delta t^2\Lambda_x^{n+1/2,p}\Lambda_y^{n+1/2,p}\right)\frac{\psi^{n+1,p+1} - \psi^n}{\Delta t} = (\Lambda_x^{n+1/2,p} + \Lambda_y^{n+1/2,p})(\psi^{n+1,p+1} + \psi^n) + f^{n+1/2,p} \ , \tag{37}$$

where E is the unity operator. A comparison with Eq. 28 shows that Eq. 37 is actually equivalent to the former except by the positive definite operator having a norm greater than one:

$$B \equiv E + \Delta t^2\Lambda_x^{n+1/2,p}\Lambda_y^{n+1/2,p} = E + O(\Delta t^2), \tag{38}$$

which acts on the term $(\psi^{n+1,p+1} - \psi^n)/\Delta t$. This means that this operator does not change the steady state solution. Furthermore, since $||B|| > 1$, the scheme given by Eqs. 37, and 37 is more stable than the target one (Eq. 28).

3.5 Spatial discretization and boundary conditions

We solve numerically the SH equation with GDBC and PBC. For the case of rigid boundary conditions we adopt a staggered grid, as illustrated in Fig. 8. Consider a staggered

mesh in both spatial directions, namely

$$x_i \;=\; -\frac{\Delta x}{2} + i\,\Delta x\,, \quad \Delta x \;\equiv\; \frac{L_x}{n_x - 2}\,, \quad y_j \;=\; -\frac{\Delta y}{2} + j\,\Delta y\,, \quad \Delta y \;\equiv\; \frac{L_y}{n_y - 2}\,,$$

where n_x and n_y are the number of points in x-and y-directions, respectively. The mesh pattern is shown in Fig. 8. Let $\psi_{i,j}$ be an arbitrary set function defined on the above described mesh. We confine ourselves to the case of constant coefficients. The PBC, which is less restrictive than the GDBC, borrows the crystallography concept of unit cell, which is a repeating pattern representative of the material. That is, using PBC we have a domain that would also act as a unit cell for a infinite two-dimensional surface, with cells being periodically repeated all around the bidimensional domain.

The centered difference approximations of the spatial derivatives are obtained by Taylor developments of the function ψ at the points of the uniform grid:

$$
\begin{aligned}
\psi_{i+1} &= \psi_i + \Delta x\,\partial_x\psi + \frac{\Delta x^2}{2!}\partial_x^2\psi + \frac{\Delta x^3}{3!}\partial_x^3\psi + \frac{\Delta x^4}{4!}\partial_x^4\psi + O\!\left(\frac{\Delta x^5}{5!}\right)\,; \\
\psi_{i+2} &= \psi_i + 2\Delta x\,\partial_x\psi + \frac{4\Delta x^2}{2!}\partial_x^2\psi + \frac{8\Delta x^3}{3!}\partial_x^3\psi + \frac{16\Delta x^4}{4!}\partial_x^4\psi + O\!\left(\frac{32\Delta x^5}{5!}\right)\,; \\
\psi_{i-1} &= \psi_i - \Delta x\,\partial_x\psi + \frac{\Delta x^2}{2!}\partial_x^2\psi - \frac{\Delta x^3}{3!}\partial_x^3\psi + \frac{\Delta x^4}{4!}\partial_x^4\psi - O\!\left(\frac{\Delta x^5}{5!}\right)\,; \\
\psi_{i-2} &= \psi_i - 2\Delta x\,\partial_x\psi + \frac{4\Delta x^2}{2!}\partial_x^2\psi - \frac{8\Delta x^3}{3!}\partial_x^3\psi + \frac{16\Delta x^4}{4!}\partial_x^4\psi - O\!\left(\frac{32\Delta x^5}{5!}\right)\,.
\end{aligned}
\tag{39}
$$

Considering ψ in the bidimensional domains (Fig. 8), we can define the derivatives by truncating the following Taylor expansions (39). Then, second derivatives of ψ with second order spatial accuracy can be written as:

$$
\begin{aligned}
\partial_x^2\psi \equiv \frac{\partial^2\psi_{i,j}}{\partial x^2} &= \frac{\psi_{i,j-1} - 2\psi_{i,j} + \psi_{i,j+1}}{\Delta x^2} + O\!\left(\frac{2\Delta x^2}{4!}\right)\,; \\
\partial_y^2\psi \equiv \frac{\partial^2\psi_{i,j}}{\partial y^2} &= \frac{\psi_{i-1,j} - 2\psi_{i,j} + \psi_{i+1,j}}{\Delta y^2} + O\!\left(\frac{2\Delta y^2}{4!}\right)\,.
\end{aligned}
\tag{40}
$$

Following the same procedure, fourth derivatives of ψ with second order spatial accuracy are written as:

Figure 8 - The grids and boundary conditions used in this work. (a) The "*staggered*" grid. In the case of GDBC, values of ψ in the first two lines and in the two last ones, and also in the first two columns and in the last two ones are assigned to zero. (b) The periodic grid.

Source: Own author.

$$\partial_x^4 \psi \equiv \frac{\partial^4 \psi_{i,j}}{\partial x^4} = \frac{\psi_{i-2,j} - 4\psi_{i-1,j} + 6\psi_{i,j} - 4\psi_{i+1,j} + \psi_{i+2,j}}{\Delta x^4} + O\left(\frac{120\Delta y^2}{6!}\right) ;$$

$$\partial_y^4 \psi \equiv \frac{\partial^4 \psi_{i,j}}{\partial y^4} = \frac{\psi_{i,j-2} - 4\psi_{i,j-1} + 6\psi_{i,j} - 4\psi_{i,j+1} + \psi_{i,j+2}}{\Delta y^4} + O\left(\frac{120\Delta y^2}{6!}\right) ;$$

$$\partial_x^2 \partial_y^2 \psi \equiv \frac{\partial^4 \psi_{i,j}}{\partial x^2 \partial y^2} = \frac{1}{\Delta x^2 \Delta y^2}\left(\psi_{i-1,j-1} - 2\psi_{i,j-1} + \psi_{i+1,j-1} - 2\psi_{i-1,j} + 4\psi_{i,j} - 2\psi_{i+1,j} + \right.$$

$$\left. +\psi_{i-1,j+1} - 2\psi_{i,j+1} + \psi_{i+1,j+1}\right) + O\left(\frac{4\Delta x \Delta y}{6!}\right) . \tag{41}$$

Standard second order representations of spatial derivatives are adopted in uniform and structured grids. In order to verify the correctness of the implementation, we conducted convergence tests using the method of manufactured solutions (MMS) (ROACHE, 2002; ROY, 2005).

4 CODE VERIFICATION

One important issue concerning the simulations is the time and mesh size selection, such that we seek reasonable choices inside the stable region of the proposed numerical scheme, keeping accuracy in the numerical solutions. The governing equation (8) can be rewritten in the form $P\psi(\mathbf{x}, t) = 0$, where P is an operator containing all the partial derivatives and terms acting on the order parameter $\psi(\mathbf{x}, t)$. The consistency of the numerical scheme can be easily verified since $P\psi(\mathbf{x}, t) - P_{\Delta t, \Delta x, \Delta y}\psi(\mathbf{x}, t) \longrightarrow 0$ as $\Delta t, \Delta x, \Delta y \longrightarrow 0$, where $P_{\Delta t, \Delta x, \Delta y}$ is the finite difference discretization of P. In this section, scheme stability, free energy functional decay and convergence tests are performed to verify the code implementation.

4.1 Linear growth analysis

The linear stability analysis performed in section 2.3 provided the linear growth rates for the unstable modes in the bandwidth associated with a particular ε value. Therefore, we have the analytical prediction of the linear growth for each wavenumber q by means of the following dispersion relation:

$$\omega(q) = \varepsilon - \alpha \left(q^2 - q_0^2 \right)^2 . \tag{42}$$

Numerically, we can obtain this linear growth by starting a simulation from a preexisting initial condition of stripes, with a wavenumber q, in the form

$$\psi_m(x, 0) = F \cos(q x), \tag{43}$$

where $F = 10^{-8}\sqrt{\epsilon}$ is assumed. Considering that at earlier time steps, the dynamics is dominated by the linear terms, one can numerically obtain ω_q, by evaluating it as

$$\omega_q = \frac{1}{\Delta t} \left(\frac{\psi_c^{n+1}}{\psi_c^n} - 1 \right) . \tag{44}$$

For the sake of simplicity, the values of the order parameter used in Eq. (44) correspond to those extracted from the center of the domain, $C(L_x/2, L_y/2)$, for which the notation, ψ_c^{n+1}, ψ_c^n, holds. In order to compare with the theoretical $\omega(q)$, the numerical linear growth ω_q is evaluated after five time steps. Figure 9 shows the comparison between the results for the linear growths, considering two different domain sizes (8×8 wavelengths, and 64×64 wavelengths), and three numerical set ups. Firstly, using the finite-difference scheme outlined in the previous chapter with GDBC and PBC, and secondly using the pseudo-spectral scheme for PBC outlined in appendix C.

Figure 9 - Numerical linear growth rates compared to linear stability analysis prediction for the Swift-
Hohenberg dynamics
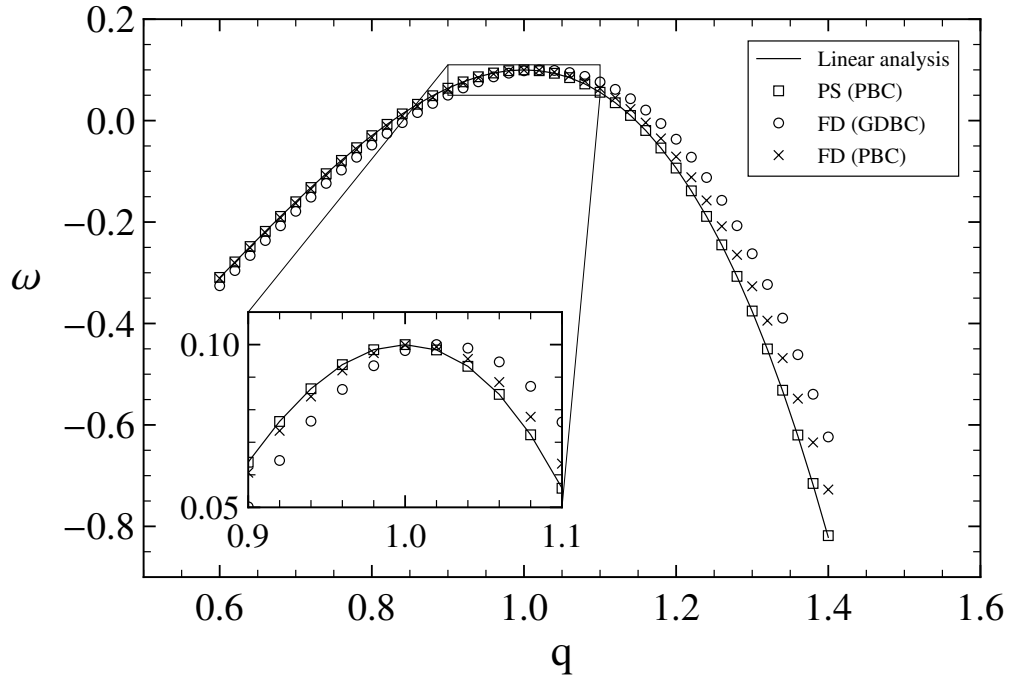
(a) 8 × 8 wavelengths domain (128 × 128 nodes)
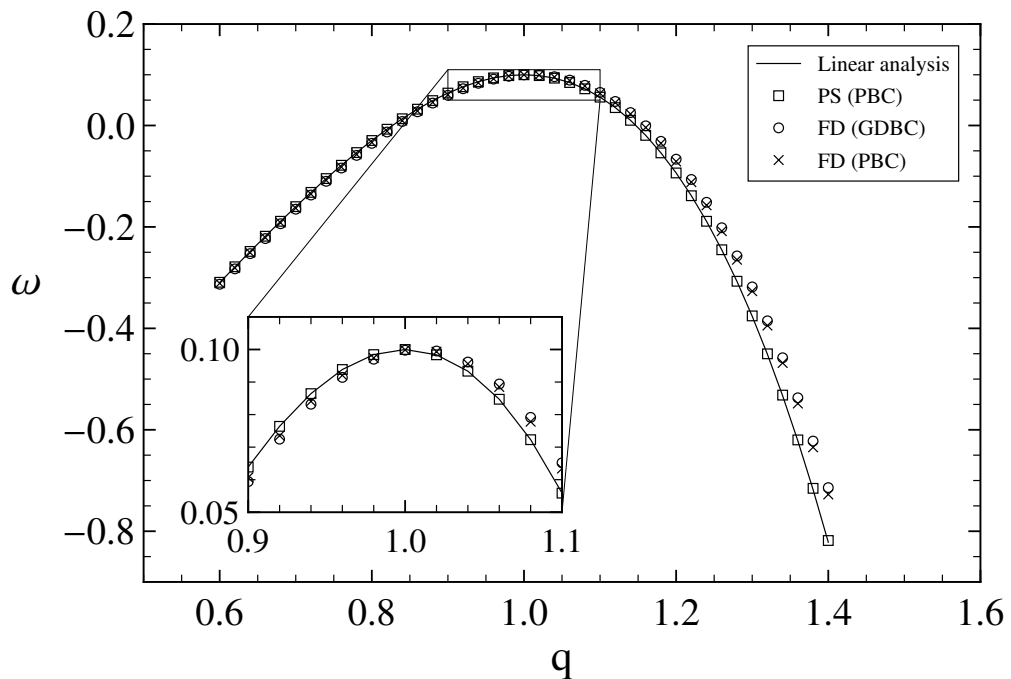
(b) 64 × 64 wavelengths domain (1024 × 1024 nodes)

Source: Original work by the author.

Figure 10 - Pattern developed with the SH3 model, GDBC, forced with a spatial ramp of the control parameter given by $0.0 \leq \varepsilon(\mathbf{x}) \leq 0.2$, and six different time steps. Top row: transient states at $t = 100$. Bottom: the steady state for the six time steps. All tests started from the exactly same initial condition (pseudo-randomly generated) for a 64×64 nodes domain. Note that the use of larger time steps results in smaller number of required steps to attain the same "time" ($t = 100$ for instance). Errors with larger time steps result in delay in the emergence of the pattern and thus later steady states is expected.

| $t = 100$ | $t = 100$ | $t = 100$ | $t = 100$ | $t = 100$ | $t = 100$ |
| $\Delta t = 0.01$ | $\Delta t = 0.1$ | $\Delta t = 0.5$ | $\Delta t = 1.0$ | $\Delta t = 2.0$ | $\Delta t = 10.0$ |

| $t = 3062$ | $t = 3066$ | $t = 3142$ | $t = 3412$ | $t = 4522$ | $t = 30230$ |
| $\Delta t = 0.01$ | $\Delta t = 0.1$ | $\Delta t = 0.5$ | $\Delta t = 1.0$ | $\Delta t = 2.0$ | $\Delta t = 10.0$ |
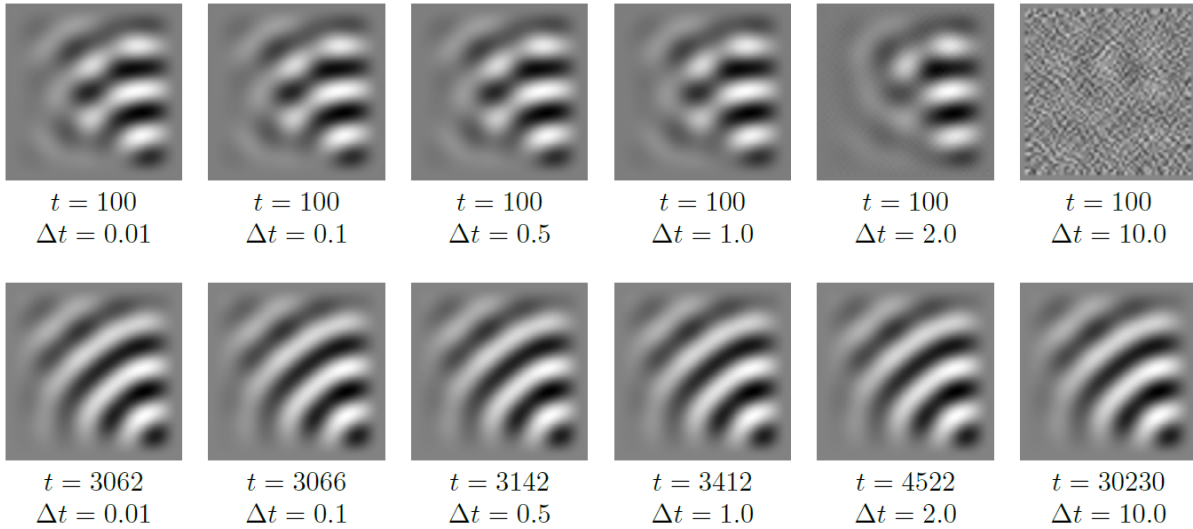
Source: Original work by the author.

4.2 Scheme Stability

Here, following Christov and Pontes (2001)(CHRISTOV; PONTES, 2002), we study the effect of the time step in the structure evolution by assessing the rate of change in time of the pattern during the simulation. We do this by monitoring $\dot{L}_1$, the relative norm rate of change defined as:

$$\dot{L}_1 = \frac{1}{\Delta t} \left(\frac{\sum\limits_{i=1}^{n_x} \sum\limits_{j=1}^{n_y} |\psi_{i,j}^{n+1} - \psi_{i,j}^{n}|}{\sum\limits_{i=1}^{n_x} \sum\limits_{j=1}^{n_y} |\psi_{i,j}^{n+1}|} \right), \tag{45}$$

which roughly corresponds to the ratio between the spatial average of the modulus of time derivative $\partial \psi / \partial t$ and the spatial average of the modulus of the function itself. The calculations begin from a random initial condition and proceeded until $\dot{L}_1 \leq 5 \times 10^{-7}$, which is our criterion for reaching the steady state. Following this implementation, Fig. 10 shows the system state at $t = 100$ and the steady state attained in six simulations run with different time steps Δt. Fig. 11 shows the evolution of the associated $\dot{L}_1$ and the curves of the accomplished internal iterations at each time step. This group of simulations is run with GDBC.

Figure 11 - Scheme stability analysis from the numerical integration of the Swift-Hohenberg equation.
(a) $\dot{L}_1$ and (b) internal iterations are shown as a function of time t for a 64×64 nodes domain
for all six tests are presented in Fig. 10. The same steady pattern is reached for all six analyzed
cases independently of the time step. The simulations started from the same random initial
conditions.

(a)

(b)
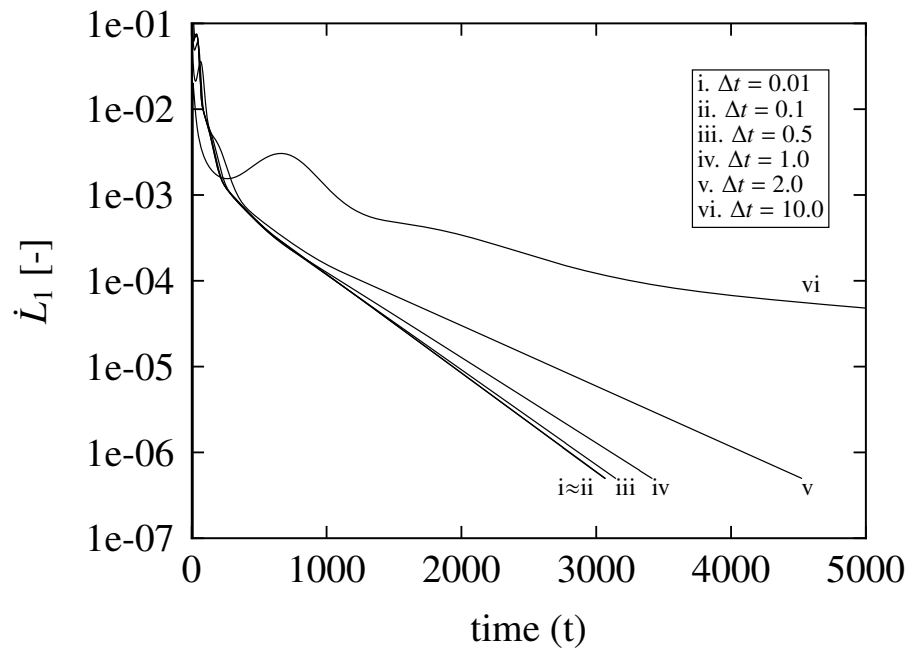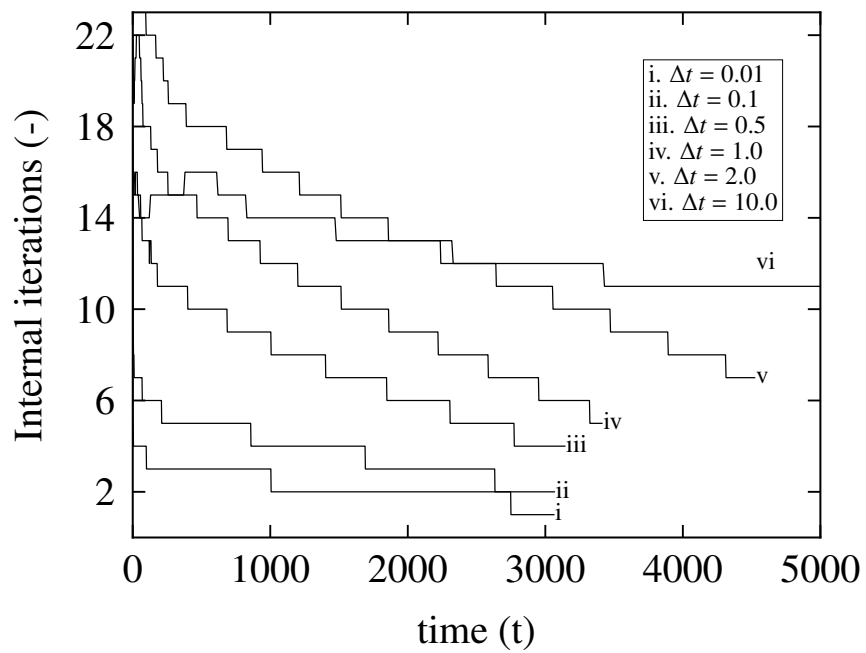
Table 1 - Computational time spent for each of the simulations presented in Fig. 10 on the computer outlined in appendix D.

Time step	Minimum iterations	Maximum iterations	Steady state	Computational time spent (min/min)
$\Delta t = 0.01$	1	23	$t = 3062$	234.4
$\Delta t = 0.1$	2	15	$t = 3066$	6.6
$\Delta t = 0.5$	4	18	$t = 3142$	1.7
$\Delta t = 1.0$	5	22	$t = 3412$	1.4
$\Delta t = 2.0$	7	23	$t = 4522$	1.2
$\Delta t = 10.0$	7	16	$t = 30230$	1

Source: Original work by the author.

Since the semi-implicit scheme is unconditionally stable for any time step, the CPU time to reaching the desired numerical solutions can be be optimized without major restrictions to selected time step, as shown by Tab. 1. A conservative choice for all simulations would be $\Delta t = 0.1$, which presents the same $\dot{L}_1$ decay curve as for $\Delta t = 0.01$. The choice for the remainder of this work is $\Delta t = 0.5$ for the SH3 simulations and $\Delta t = 0.1$ for the SH35, so that lower computational time is required without losing physically consistent transient results given the numerical scheme stability.

4.3 Convergence analysis

The adopted method to verify the order of accuracy of the code is the method of manufactured solutions (MMS). It provides a convenient way of verifying the implementation of nonlinear numerical algorithms by using a manufactured (artificial) solution (MS) for such purpose (ROACHE, 2002; ROY, 2005; VITRAL et al., 2018). In terms of the proposed problem, we take all the members of the SH equation 8 and consider the following differential equation:

$$F(\psi) = 0, \tag{46}$$

where ψ is the order parameter function that satisfies Eq. 46 and therefore is the PDE solution. The MMS consists of adopting an arbitrary function to be the manufactured solution, $\psi_m(\mathbf{x}, t)$, and since this function is not likely to solve the PDE, a source term is expected, s_m. This term can be seen as an additional forcing function, leading to a modified operator with this

Table 2 - Parameters assumed for the governing equations studied in this work.

MS Parameters	Value	SH Parameters	Value
q_1	$0.25\sqrt{2}q_0$	ε	-0.1
q_1^*	$\sqrt{2}q_0$	q_0	1.0
ψ_0	0.0	α	1.0
ψ_{xy}	$\sqrt{|\varepsilon|}$	β	-1.0
a	0.0	γ, ζ	0.0

Source: Original work by the author.

new source:

$$\bar{F}(\psi) \equiv F(\psi) - s_m . \tag{47}$$

For the previous equation, $\bar{F}(\psi_m) = 0$ and $\bar{F}(\psi) = -s_m$. Following this new approach to the problem, we find an approximate numerical solution, ψ_k, for the discretized problem so that $\bar{F}(\psi_k) = 0$ or $F(\psi_k) = s_m$. This source term is a minimal intrusion to the code's formulation. The chosen function is periodic with a wavenumber q_1 and is defined as:

$$\psi_m(\mathbf{x}, t) = \psi_0 + \psi_{xy} \cos[q_1(x + y)]e^{at}, \tag{48}$$

where all parameters employed in the manufactured solution and in the differential equation are present on Tab. 2.

The global discretization error is examined by the L_2 norm, defined as follows:

$$L_2 = \left(\frac{\sum\limits_{i=1}^{n_x} \sum\limits_{j=1}^{n_y} |(\psi_k)_{i,j}^n - (\psi_m)_{i,j}^n|^2}{\sum\limits_{i=1}^{n_x} \sum\limits_{j=1}^{n_y} |(\psi_m)_{i,j}^n|^2} \right)^{1/2} . \tag{49}$$

In the previous section, a second-order scheme is presented and therefore the formal order of accuracy is two. The observed order of accuracy of the code can be acquired from the global discretization error for meshes with different grid spacing, and can described by the following

Table 3 - Meshes employed for the code verification by MMS. The chosen domain for the test has 4×4 critical wavelengths. The observed order of accuracy of the code in Fig. 12 can be calculated using Eq. (50) for two cases: $q_1 = 0.25\sqrt{2}q_0$ and $q_1^* = \sqrt{2}q_0$. In the first case the formal order of accuracy is achieved, $p \approx 2.0$, while in the second case $p^* \approx 4.0$ due to discretization error canceling.

Mesh	Number of nodes	Grid resolution (g_r)	Convergence rate (p)	
			$\left(q_1 = 0.25\sqrt{2}q_0\right)$	$\left(q_1^* = \sqrt{2}q_0\right)$
Mesh A	16×16	4	-	-
Mesh B	32×32	8	1.99514004	3.95294357
Mesh C	64×64	16	1.99862314	3.98876043
Mesh D	128×128	32	1.99964767	3.99722721
Mesh E	256×256	64	1.99991139	3.99916624

Source: Original work by the author.

relation:

$$p = \frac{\ln\left(L_2^B/L_2^A\right)}{\ln(r)}, \tag{50}$$

where L_2^A and L_2^B are the L_2 norm for meshes A and B respectively, and r is the ratio of the grid resolution, g_r, given in number of mesh nodes per critical wavelength of mesh B to A. The meshes employed for the present tests, the number of nodes, and grid resolutions are shown in Tab. 3, and the L_2 curves for the numerical experiments can be seen in Fig. 12.

A truncation error canceling could be seen when the choice for the manufactured solution wavenumber is $q_1 = \sqrt{2}q_0$. The latter modifies the expected convergence rate up to fourth-order, which is consistent with the analytical development of the manufactured solution in Eq. 47. To verify the general case, we construct a manufactured solution with $q_1 \neq \sqrt{2}q_0$. Following this approach, a second-order convergence rate is recovered as theoretically expected.

The numerical scheme has been proven to be consistent, unconditionally stable and truly second-order accurate in space, in the general case. The chosen grid resolution for the numerical experiments, presented in the next section, is $g_r = 16$, which has a good trade-off between resolution and computational cost in order to represent periodic solutions.

Figure 12 - L_2 norm of the ψ function for the manufactured solution. The observed order of accuracy of the code using Eq. 50 for both cases shown in Tab. 3. In first case, the L_2 norm is parallel to the (a) second-order slope and in the second case it is parallel to the (b) fourth-order slope.

(a)

(b)
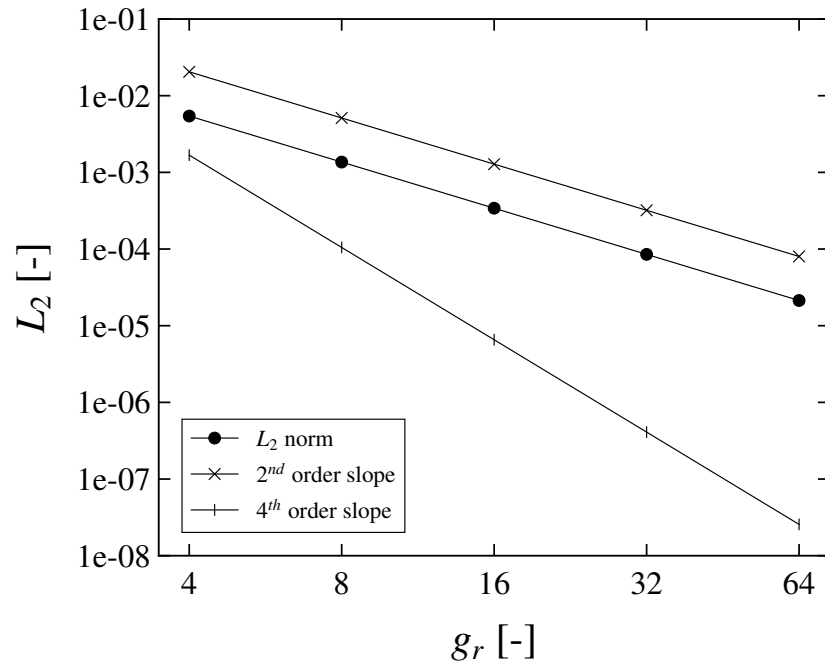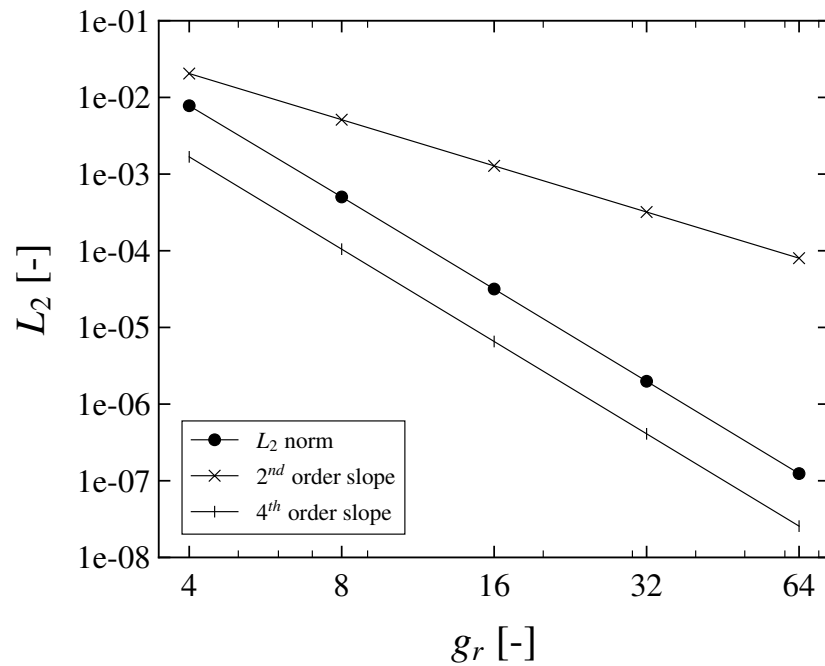
Source: Original work by the author.

Figure 13 - Evolution in time of the L_2 norm comparing different grid resolutions. The resulting curves for the L_2 norm evolution in time are shown for the (a) first and (b) second case. Both L_2 norm evolutions start from values close to the machine precision (10^{-16}), since we start the convergence analysis simulations from the exact solution. In the first case the formal order of accuracy is achieved, $p \approx 2.0$, while in the second case $p^* \approx 4.0$ due to discretization error canceling.

(a)

(b)
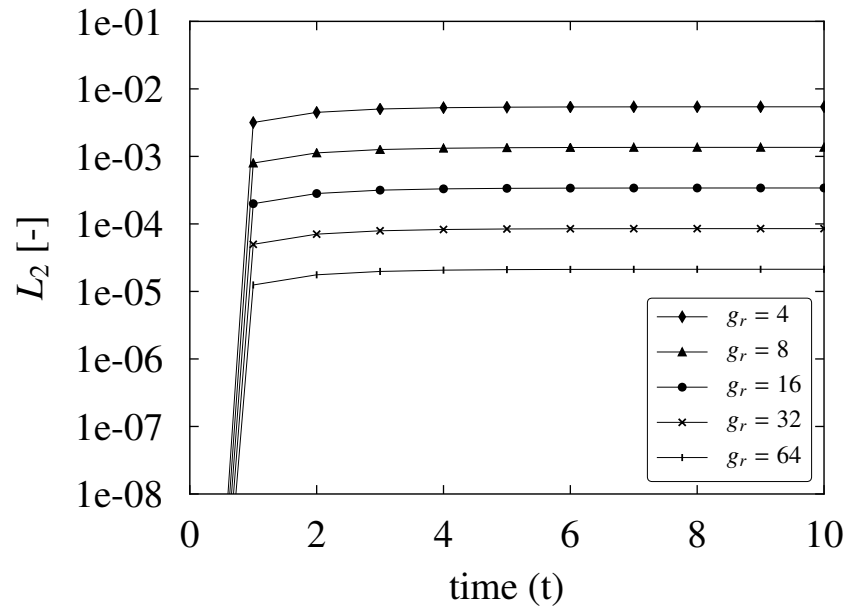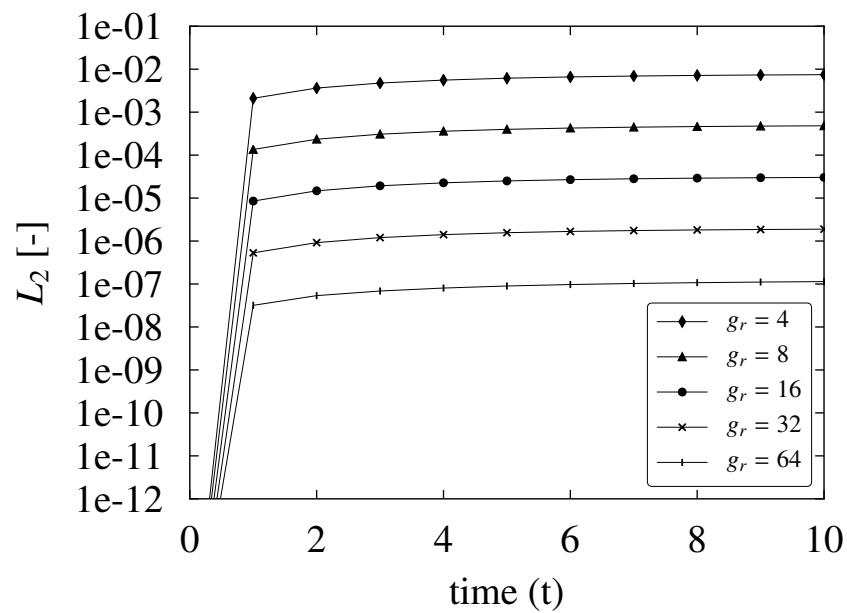
Source: Original work by the author.

4.4 Lyapunov functional decay

The decay of the Lyapunov functional ('free energy') is monitored so that we can confirm it is always monotonically decreasing until a minimum value is reached in the steady state. In order to take into account the assumed boundary conditions adopted in this work, we expand the bulk integrals to show that boundary integrals vanish, leading to a new expression for the free energy functional, which is going to be discretized. Using integration by parts and the 2D Gauss theorem (first Green identity), we have:

$$
\int_{\Omega} d\mathbf{x} \left(\psi \nabla^2 \psi \right) = \oint_{\partial\Omega} \psi \frac{\partial \psi}{\partial n} dl - \int_{\Omega} d\mathbf{x} (\nabla \psi)^2, \tag{51}
$$

where the first integral from RHS vanishes for the assumed GDBC, above mentioned. Now Eq. 5 can be rewritten as:

$$
\mathcal{F}[\psi] = \int_{\Omega} d\mathbf{x} \frac{1}{2} \left\{ -\epsilon(\mathbf{x})\psi^2 + \alpha \left[q_0^4 \psi^2 - 2q_0^2 (\nabla \psi)^2 + (\nabla^2 \psi)^2 \right] - \frac{\beta}{2} \psi^4 + \frac{\gamma}{3} \psi^6 \right\}. \tag{52}
$$

The Lyapunov functional associated to the SH equation is implemented through the discrete formula derived by Christov and Pontes (2002) for the cubic version, and now extended for the quintic one. The formula presents a $O\left(\Delta t^2 + \Delta x^2 + \Delta y^2\right)$ approximation of the functional given by Eq. 6. As pointed by those authors, the monotonic decay of the finite differences version is enforced, provided that the internal iterations converge. The decay is monitored by:

$$
\frac{\mathcal{F}^{n+1} - \mathcal{F}^n}{\Delta t} = -\sum_{i=1}^{n_x} \sum_{j=1}^{n_y} \left(\frac{\psi_{i,j}^{n+1} - \psi_{i,j}^n}{\Delta t} \right)^2, \tag{53}
$$

and

$$
\begin{aligned}
\mathcal{F}^n = & \sum_{i=1}^{n_x} \sum_{j=1}^{n_y} \left[-\frac{\epsilon}{2} \left(\psi_{i,j}^n \right)^2 - \frac{\zeta}{3} \left(\psi_{i,j}^n \right)^3 - \frac{\beta}{4} \left(\psi_{i,j}^n \right)^4 + \frac{\gamma}{6} \left(\psi_{i,j}^n \right)^6 + \frac{\alpha q_0^4}{2} \left(\psi_{i,j}^n \right)^2 \right] \\
& - \frac{\alpha q_0^2}{2} \sum_{i=1}^{n_x} \sum_{j=1}^{n_y} \left[\frac{\psi_{i+1,j}^n - \psi_{i,j}^n}{\Delta x} \right]^2 + \left[\frac{\psi_{i,j}^n - \psi_{i-1,j}^n}{\Delta x} \right]^2 + \left[\frac{\psi_{i,j+1}^n - \psi_{i,j}^n}{\Delta y} \right]^2 + \left[\frac{\psi_{i,j}^n - \psi_{i,j-1}^n}{\Delta y} \right]^2 \\
& + \frac{\alpha}{2} \sum_{i=1}^{n_x} \sum_{j=1}^{n_y} \left[\psi_{i+1,j}^n - 2\psi_{i,j}^n + \psi_{i-1,j}^n \Delta x^2 + \psi_{i,j+1}^n - 2\psi_{i,j}^n + \psi_{i,j-1}^n \Delta y^2 \right]^2. \tag{54}
\end{aligned}
$$

In order to check if the Lyapunov functional is correctly implemented, we ran two simulations with the cubic SH (with ramped ϵ) and four with the quintic one (both uniformly and ramped ϵ), and monitored the evolution of the functional, of $\dot{L}_1$ and of the patterns observed through the order parameter $\psi(\mathbf{x}, t)$. The patterns evolution and the associated $\dot{L}_1$ and Lyapunov potentials are presented in Figs. 14, 20. The simulations were run with ramps of the control

parameter $\epsilon(\mathbf{x})$ along the x-direction for both GDBC and PBC. The two simulations with the SH3 model started from the same pseudo-random initial condition. The four simulations with the SH35 model started from a squared localized patch in the center of the cell. This pre-existing structure of stripes parallel to the y-direction were constructed by:

$$\psi(\mathbf{x}, 0) = A_0 \cos(q_0 x), \tag{55}$$

where $A_0 = \left\{ (\beta/(2\gamma)) [1 + \sqrt{1 + \epsilon\gamma/\beta^2}] \right\}^{1/2}$, which is compatible with the expected field ψ amplitude for a stable spatially homogeneous states, for the SH35 (SAKAGUCHI; BRAND, 1996). The results of these six simulations confirm the correct implementation of the Lyapunov functional for both equations, with a monotonic decay in all cases.

Figure 14 - The results of two simulations run to verify the correctness of the implementation of the Lyapunov functional for the SH3 model. First and second rows: SH3 pattern evolution for a ramped system forced with $0.0 \leq \epsilon \leq 0.2$ GDBC (a) and PBC (b), respectively, until the indicated steady state.. Both simulations started with the same pseudo-random initial condition. $\dot{L}_1$ and the Lyapunov potential evolutions are showed below.

(a) GBDC

(b) PBC

(c)
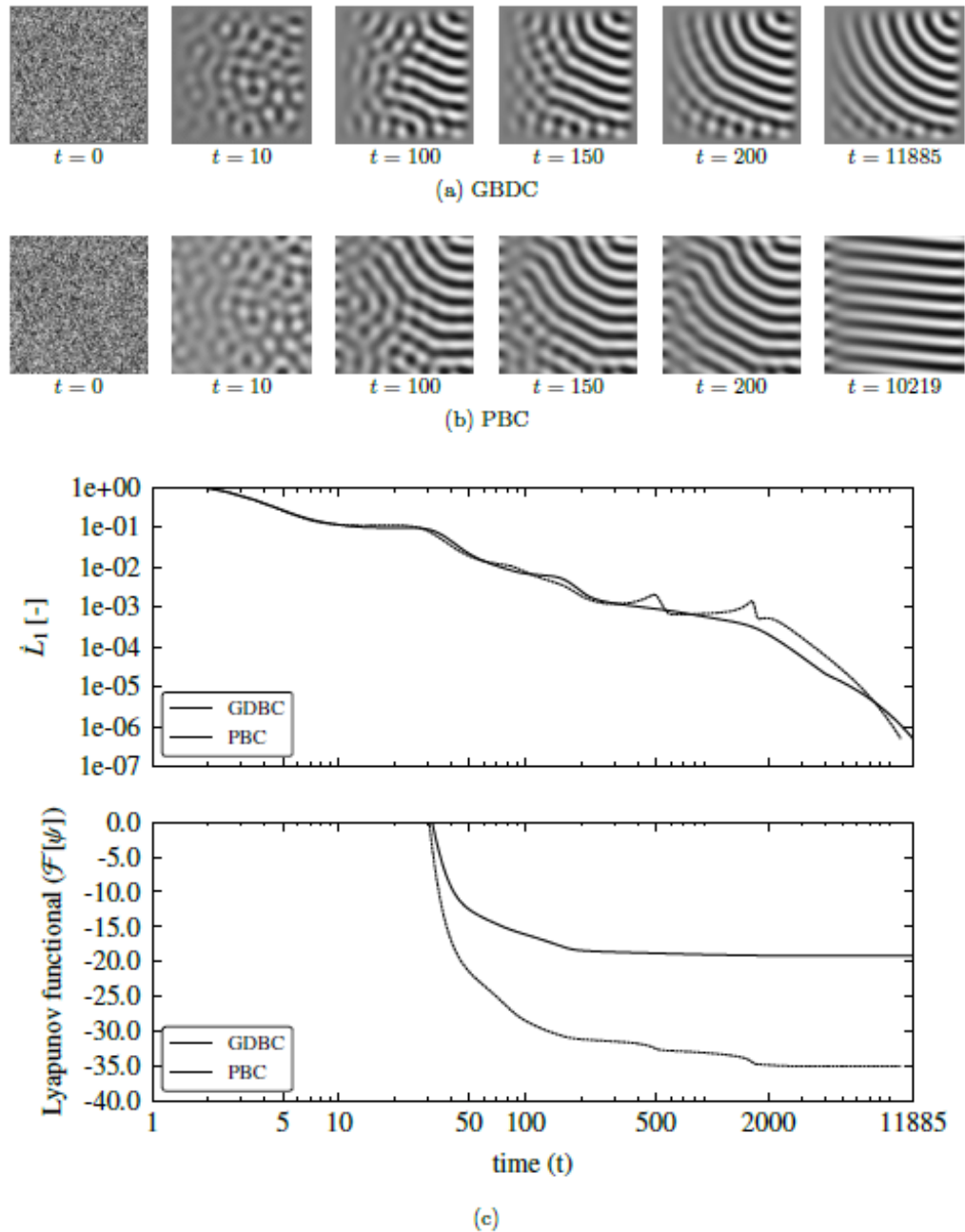
Source: Original work by the author.

Figure 15 - The results of two simulations run to verify the correctness of the implementation of the Lyapunov functional for the SH35 model. First and second rows: SH35 pattern evolution for a ramped system forced with $-1.4 \le \epsilon \le -1.2$, GDBC (a) and PBC (b), respectively, until the indicated steady state.. Both simulations started from the same pre-existing structure of rolls perpendicular to the gradient of the control parameter. $\dot{L}_1$ and the Lyapunov potential evolutions are showed below.

(a) GDBC

(b) PBC

(c)
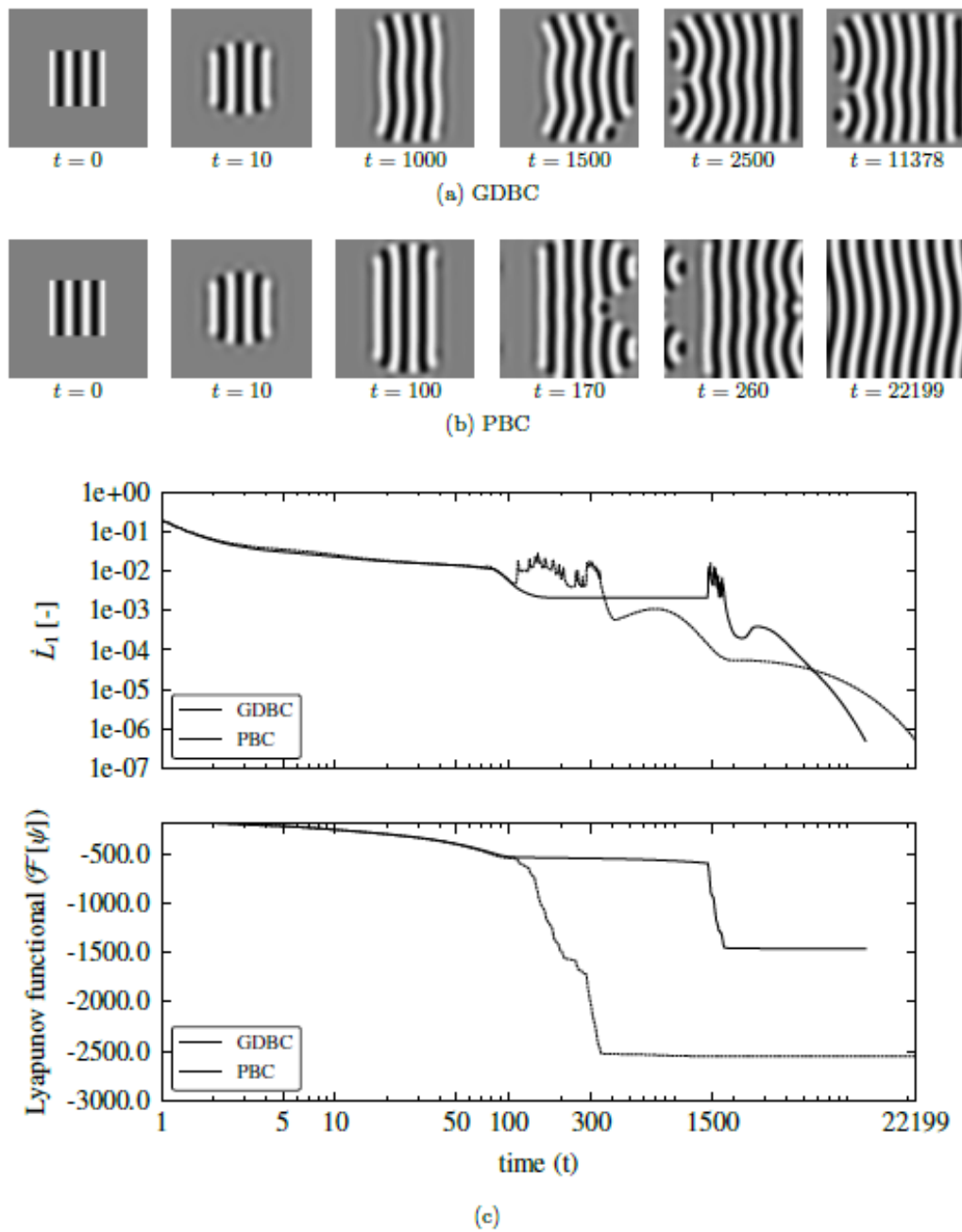
Source: Original work by the author.

5 RESULTS

In this chapter numerical results are shown for stripes pattern behavior in the presence of the orientation effect, due to gradients of the control parameter, and of competing effects, complementing the stability analysis presented in Sec. 2.3. The study is made through a numerical integration of the SH3 equation, using the semi-implicit finite-difference scheme, outlined in Chapter 3 that has been previously adopted for Swift-Hohenberg (CHRISTOV et al., 1997; COELHO et al., 2020) and other nonlinear parabolic equations (VITRAL et al., 2018). Just as remainder, the common parameters used are $\alpha = 1$, and $q_0 = 1$. Unless otherwise noted, the computational domain is 128×128 grid points, which corresponds to a physical domain of 8×8 critical wavelengths considering a grid resolution of 16 points per wavelength. Therefore, the grid size is $\Delta x = \Delta y \approx 1.016[2\pi/(16q_0)]$ when using GDBC and $\Delta x = 2\pi/(16q_0)$ when using PBC. We employ a second order accurate time integration scheme using a Crank-Nicolson approach and the time steps used are $\Delta t = 0.5$ (SH3) and $\Delta t = 0.1$ (SH23/SH35).

All patterns shown are at the steady state, with the exceptions of the initial conditions, and of those shown during the evolution. We consider a pattern at the steady state when its velocity of evolution, $\dot{L}_1$, falls below 5×10^{-7}. All simulations starting from a pseudo-random distribution of ψ use the same distribution as an initial condition.

5.1 Competition between the gradient, boundary and bulk effects – SH3

The results are organized in five sections 5.1.1, 5.1.2, 5.1.3, and 5.1.4. Section 5.1.1 shows the results of simulations starting from preexisting stripes, with forcings in the form of spatial ramps of ε along the x direction. Both Generalized Dirichlet (GDBC) and Periodic (PBC) boundary conditions are considered. Cross sections of selected steady state patterns are shown, along with the envelopes obtained as the steady state solution of Eqs. 21, 22 and 25. Section 5.1.2 presents the results of simulations starting from a pseudo-random initial condition, forced with ramps of ε along the x direction. In Secs. 5.1.3 and 5.1.4 we describe the results obtained with sinusoidal and Gaussian forcings, respectively, both cases starting from pseudo-random initial conditions.

5.1.1 Spatial ramps of ε and preexisting patterns

This section presents results of eight simulations whose initial conditions consist of preexisting structures of straight stripes parallel or perpendicular to the $\nabla\varepsilon$. The forcing takes the form of spatial ramps along the x direction, submitting the dynamics to this spatial variation of

Table 4 - Parameters adopted for the simulations.

Parameter	Formulæ	Value	Description
q_0	-	1.0	Critical wavenumber
λ_0	$2\pi/q_0$	2π	Critical wavelength
w_x, w_y	-	8	Wavelengths per domain length
g_r	-	16	Grid resolution
n_x, n_y	$w_x \times g_r$, $w_y \times g_r$	128	Nodes per mesh side
N	$n_x \times n_y$	128×128	Total mesh nodes
L_x, L_y	$w_x\lambda_0, w_y\lambda_0$	≈ 50.2655	Domain length (L)
$\Delta x, \Delta y$	$L/(n-2)$	≈ 0.3989	Space step (GDBC)
$\Delta x, \Delta y$	L/n	≈ 0.3927	Space step (PBC)
Δt	-	0.5	Time step (SH3)
Δt	-	0.1	Time step (SH23/SH35)
A	-	0.2	Gaussian maximum value (peak)
R_1	n_x^{-1}	-	Configs. 04 and 09
R_2	$0.2n_x^{-1}$	-	Configs. 05 and 10
x_0, y_0	$L_x/2, L_y/2$	-	Gaussian center

Source: Original work by the author.

ε. The results are shown in Figs. 16 and 18. Figure 16 presents the initial conditions and the steady state of the simulations. Figure 18 shows the one dimensional profile of four patterns from Fig. 16, taken along the x direction, at the middle height (y-direction) of the domain. For these profiles, we compared the envelopes of modes either parallel or perpendicular to the gradient, to analytic and numerical estimates based on the weakly nonlinear analysis detailed in Sec. 2.3.

Results shown in the first two rows of Fig. 16 are run from an initial condition consisting of stripes parallel to the gradient, while the last two rows started from stripes perpendicular to the gradient. GDBC is adopted for the simulations in the first and the third rows, and those in the second and fourth rows are obtained adopting PBC. The preexisting structure of stripes is shown in the first column of Fig. 16. The configurations (steady states) shown in the second and third column are numbered for reference.

Configuration 1, with a ε ramp increasing from 0 to 0.1, evolved from stripes parallel to the x axis to a bent structure of stripes approaching the upper and the right sidewalls, oriented perpendicularly to the walls. At the left sidewall, this structure is parallel to wall, a result that complies with the work of Walton (1982)(WALTON, 1982), who identified the onset of a weak structure of stripes parallel to a slightly subcricrical or supercritical sidewall, in presence of a negative gradient of the Rayleigh number pointing to the bulk of a Rayleigh-Bénard cell. A weak structure of stripes perpendicular to the lower wall is visible close to that wall, since GDBC favors this orientation due to the zero normal derivative. Boundary effects dominate both the bulk effects represented by the initial condition, and $\nabla \varepsilon$.

A different situation occurs in the case of configuration 2. The gradient, along with orientation of the initial condition, forces the preexisting structure to remain parallel to it, and stripes are kept straightly aligned up to the steady state. This result is attributed to the increase in slope and magnitude of the ε ramp, which now increases from 0 up to 0.5.

The cases represented by configurations 3 and 4 of Fig. 16 are run with PBC. In both cases, the gradient orientation effect, along with the initial condition and the lack of the competition with boundary effects, result in stripes that remained parallel to the gradient, independently of the forcing magnitude.

Configuration 5 presents a result similar to the one obtained in configuration 1, while in configurations 6, 7 and 8, the preexisting initial conditions persist, even with PBC, where boundary effects are suppressed. The resulting orientation is, in these cases, dominated by the preexisting pattern and boundary effects, opposite to the orientation favored by $\nabla \varepsilon$. The results of configurations 6, 7 and 8 suggest that without a certain level of perturbation, the presence of the gradient is not enough to destabilize stripes in finite or periodic domains, in the sense that no reorientation by the gradient is observed. While $\nabla \varepsilon$ is not sufficient to reorient a preexisting pattern with initial wavevector $\mathbf{q}_0$ parallel to it (without perturbing the system), Fig. 17 shows through the evolution of the Lyapunov functional from Eq. 5. The orientation of the pattern with respect to the gradient strongly affects the relaxational dynamics and energy of the steady state structures. The top panel of Fig. 17 follows the energy for the dynamics leading to configurations

Figure 16 - The results of eight simulations with the SH3 equation, preexisting structures, and forced with a spatial ramp of the control parameter. The first column presents the prescribed initial condition. Columns 2 and 3 show the attained steady state. The ramp of the control parameter is given by the diagrams of first row. Rows two and three correspond to simulations with rigid boundary conditions (GDBC), while results presented in rows four and five are obtained with periodic boundary conditions (PBC).
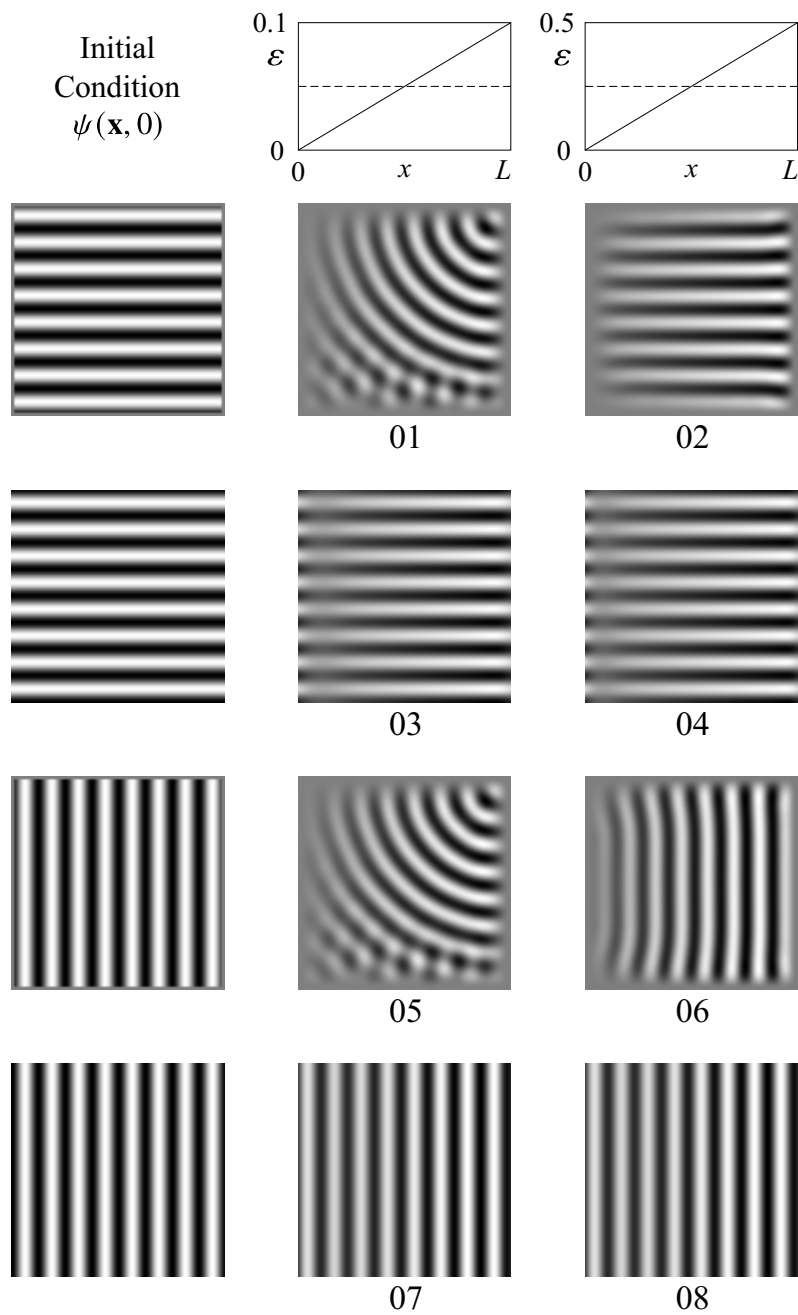
Source: Original work by the author.

Figure 17 - Lyapunov functional curves of configurations with ramped forcings with each configuration indicated. It roughly corresponds to the "normalized" modulus of the time derivative $\partial \psi / \partial t$ and therefore is sensitive not only to the growth of the amplitude, but also to the pattern phase dynamics.
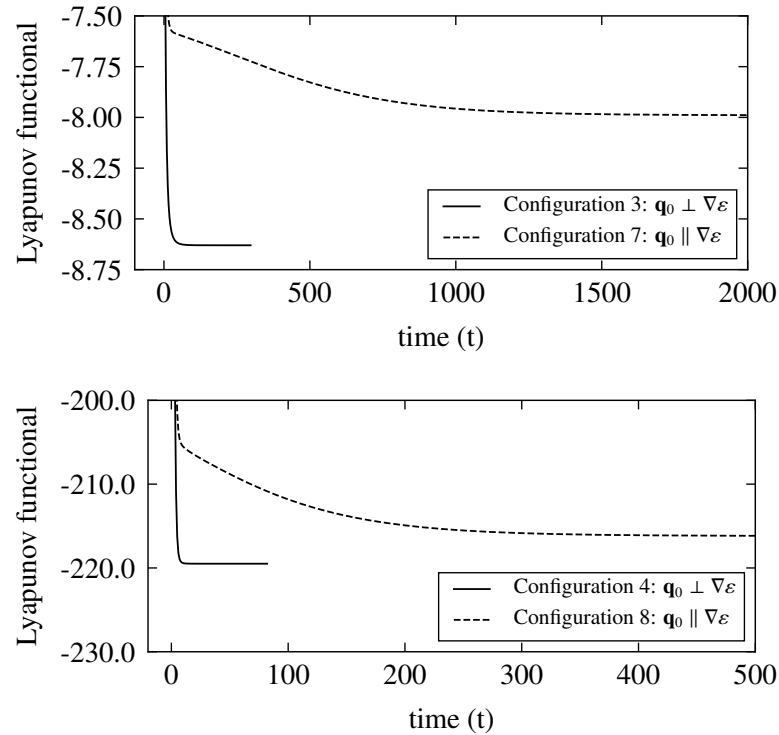
Source: Original work by the author.

3 and 7 in Fig. 16, and the bottom panel follows the energy evolution leading to the patterns in configurations 4 and 8. For both comparisons it is evident that the configuration of stripes parallel to the $\nabla \varepsilon$ is the one of minimum energy (among the two), whose amplitude quickly relaxes to satisfy the control parameter ramp. However, for $\mathbf{q}_0 \parallel \nabla \varepsilon$, the relaxation towards the steady state is much slower, since this orientation is penalized by the gradient and the steady state pattern presents a higher associated energy.

We also observe that for higher forcing levels and higher ramp slope (bottom panel), the system achieves the steady state faster than for lower forcing levels (top panel). Moreover, the energy ratio between $\mathbf{q}_0 \perp \nabla \varepsilon$ and $\mathbf{q}_0 \parallel \nabla \varepsilon$ decreases from 1.080 between the two steady states in the top panel to 1.015 in the bottom panel. The previous two observations suggest that the orientational effects due to $\nabla \varepsilon$ weaken as the forcing level increases.

Figure 18 shows cross sections of configurations 1, 2, 3 and 6 of Fig. 16. The cross sections are taken along the x direction, at the middle height (y-direction) of the domain. The obtained profiles are superposed with the patterns envelope, estimated using two approaches, based on the weakly nonlinear analysis presented Sec. 2.3. The first approach consists of an analytic estimation of the envelope height, using the steady state solution of the NWS equation given by Eq. 21,

Figure 18 - Cross sections along the *x*-direction, taken at the middle of the height of the domain (*y*-direction), and envelopes obtained by the two methods based on the weakly analysis described in Sec. 2.3. The pattern profiles extracted directly from the integration of the SH3 equation are represented by dotted lines. The envelopes estimated with Eq. 25 are shown in dashed lines, and the envelope obained as the steady state solutions of the NWS Eqs.20 and 21 are represented in continuous lines. Eq. 25 gives a good estimation of the enveleope, except close to the boundaries, since this equation does not take boundary conditions into account. Note that the so obtained envelopes in case (*a*) shoud not necessarily fit the crests of the pattern, since these curves refer to single mode stripes, either parallel or perpendicular to the gradient, and not to bended stripes, where the angle of the wavevector with the gradient continuous varies across the domain. Nevertheless, the envelope estimated with Eq. 25 matches well the pattern crests, except at the boundaries.

(a) Configuration 01 (GDBC): $0 \leqslant \varepsilon(x) \leqslant 0.1$.

(b) Configuration 02 (GDBC): $0 \leqslant \varepsilon(x) \leqslant 0.5$.

(c) Configuration 03 (PBC): $0 \leqslant \varepsilon(x) \leqslant 0.1$.

(d) Configuration 06 (GDBC): $0 \leqslant \varepsilon(x) \leqslant 0.5$.
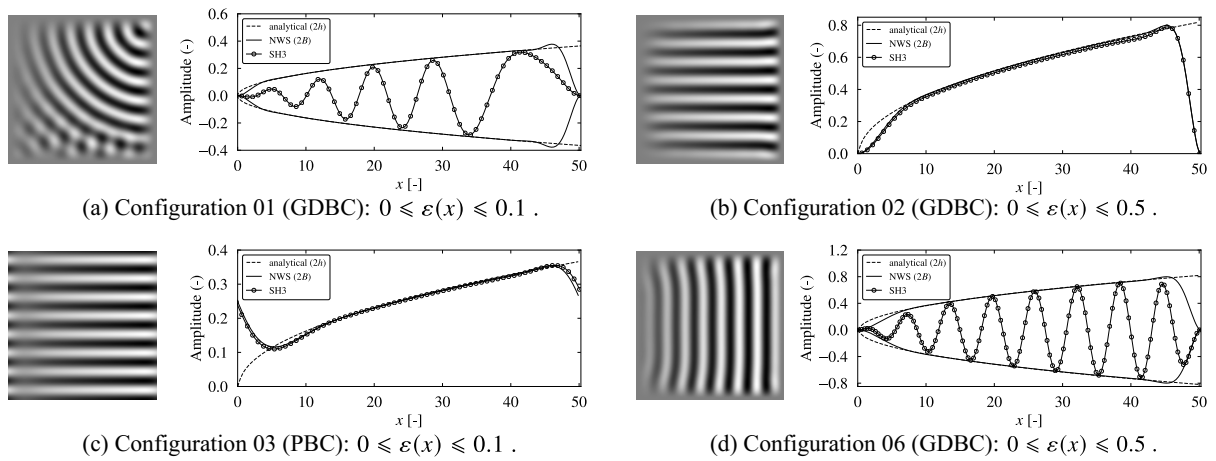
Source: Original work by the author.

obtained away from the Turing point assuming small spatial variations. The amplitude solution is given by Eq. 25, which depends only parametrically on *x* in this approximation. Note that no subcritical solutions are possible with this equation. The second approach consists in solving the NWS Eq. 21 at the steady state with a pseudo-spectral method described in Appendix B.

For case (*a*) of Fig. 18 we acquired the profile from configuration 1 of Fig. 16, which adopts GDBC. Strictly speaking, the envelopes for this case should not necessarily fit the crests of the pattern, since these envelopes refer to single mode stripes, either parallel or perpendicular to the gradient, and not to bent stripes, where the angle of the wavevector with the gradient continuously varies across the domain. Nevertheless, the envelope estimated with Eq. 25 matches well the pattern crests, except at the boundaries. The amplitude obtained as the steady solution of Eq. 21 matches well the crests of the pattern. This satisfactory agreement suggests that the local amplitude depends, in this case, on the local value of ε, and not on the local orientation of the wavevector.

Cases (*b*) and (*c*) of Fig. 18 refer to structures of stripes *B* parallel to the gradient, with GDBC (configuration 02) and PBC (configuration 03), respectively. The cross sections capture

Figure 19 - The results of eight simulations with the SH3 equation, preexisting structures, forced with a spatial ramp of the control parameter and PBC. The ramp of the control parameter is given by the diagrams of first row. In the first row are shown (a) steady patterns obtained from the indicated initial condition of preexisting vertical stripes without pseudo-random perturbation. In the second row are shown (b) Steady patterns obtained from the steady states above with the exact same pseudo-random perturbation $\delta\psi \in (-10^{-4}, 10^{-4})$. Periodic domains (PBC) are chosen in order to observe "only" interactions between bulk and $\nabla\varepsilon$ effects without the rigid imposition on the boundary (GDBC). Since in the weakly nonlinear analysis we find that vertical stripes are unstable in the presence of the $\nabla\varepsilon$, a small perturbation is sufficient to the system evolve into a new steady pattern where stripes align to the $\nabla\varepsilon$ direction (Configurations 13 and 15). Configuration 14 does not present such behavior and the preexisting stripes orientation prevails.
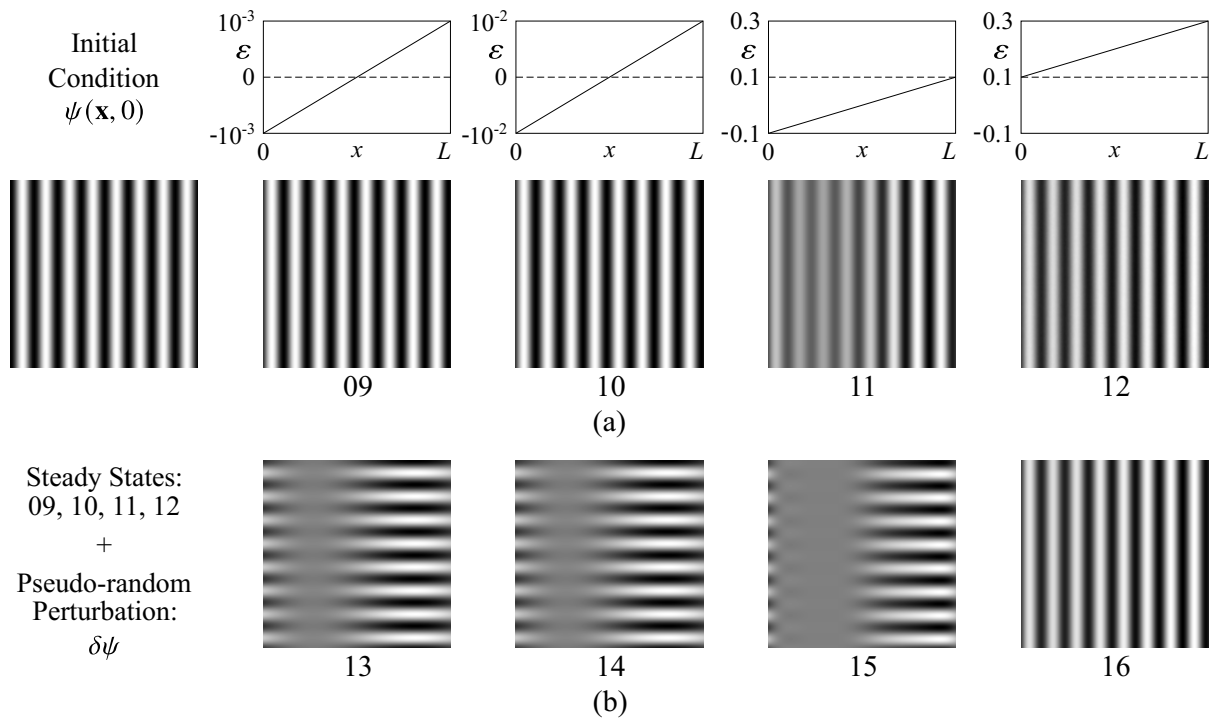
Source: Original work by the author.

the amplitude of the stripes along the direction of the gradient. The envelope given by Eq. 25 fits well the amplitude of the pattern away from the boundaries. Moreover, an excellent matching exists between the envelope obtained as the solution of the NWS Eq. 21, and the one extracted directly from the pattern, with both boundary conditions. Finally, case (*d*) of Fig. 18 is obtained from a preexisting structure of stripes A, perpendicular to the gradient (configuration 06). As in case (*a*), the crests of the pattern fit well the envelopes, and reinforces the observation that away from the boundaries $\nabla \varepsilon$ dictates the behavior of the amplitude.

To evaluate possible reorientation effects due to $\nabla \varepsilon$, as suggested by Sec. 2.3, we perturb the steady state configuration that originally have a monomodal pattern with $\mathbf{q}_0 \parallel \nabla \varepsilon$. The orientation effect can be seen in some of the configurations from Fig. 19, using PBC, so that we avoid effects from the rigid imposition on the boundary in the GDBC case. From a monomodal initial condition, we first obtain steady states under different ramps of ε, as seen in configurations 9, 10, 11, and 12, which preserve the original preexisting vertical stripes. By imposing a pseudo-random perturbation of $\delta\psi \in (-10^{-4}, 10^{-4})$ to these steady states, the cases with a ramp of ε crossing the Turing point at $\varepsilon = 0$ reorient into horizontal stripes, as observed in configurations 13, 14, and 15, independently of the slope and magnitude used for the ramp in ε. This result agrees with the conclusion from the stability analysis (Eq. 24) as in face of perturbation, the neighborhood of the Turing point should become unstable when $\mathbf{q}_0 \parallel \nabla \varepsilon$, leading the pattern to reorient. However, when the ε ramp stays in the supercritical regime, $\varepsilon > 0$, the initial pattern did not reorient, as shown in configuration 16.

5.1.2 Spatial ramps of ε and pseudo-random initial conditions

In this section we present the results of four simulations run from the same pseudo-random initial condition, and the cross section for two of the obtained configurations. Two simulations are performed with GDBC, and the other two with PBC. The results are sumarized in Fig. 20.

In the case of configuration 17, the orientation effect of the gradient is dominated by the boundary and the subcritical effects: a bent structure of stripes perpendicular to the right and to the upper sidewalls emerges. This structure persists in the subcritical region, with weak stripes approaching the left sidewall in parallel orientation. The result is in agreement with the works of Sruljes (1979)(SRULJES, 1970) an Walton (1982)(WALTON, 1982).

The steady state pattern developed in configuration 17 is similar to the one appearing in configuration 1 of Fig. 16, with the orientation effect of the gradient dominated by the boundary and the subcritical effects. The structure developed in configuration 18 is similar to the one of configuration 17, with stripes perpendiculars to the supercritical lower and right sidewalls, and paplelels to the critical left sidewall. Additionally an weak structure of stripes perpendiculars to the upper supercritical sidewall is visible.

In the case of PBC, configurations 19 and 20, no boundary effects are present and the

Figure 20 - The results of four simulations with the SH3 equation, forced with a spatial ramp of the
control parameter ε. All simulations started from the same pseudo-random initial conditions,
shown in the first column. The remaining columns present the steady state. First row: the
prescribed profile of the control parameter ε. Second and third rows: GDBC, and PBC
boundary conditions, respectively. Simulations of the second row show that boundary effects
dominate the orientaion effect when GDBC are prescribed. In the third row, the absence of
boundary effects allows the dominance of the orientation effect of the gradient.

17   18

(a) GDBC

19   20

(b) PBC
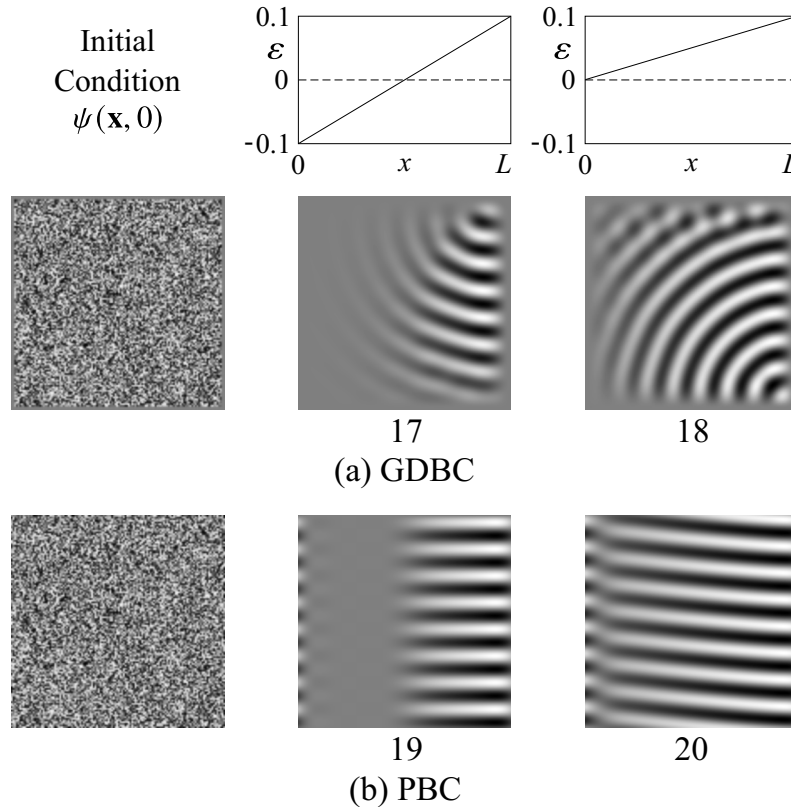
Source: Original work by the author.

resulting structure selects a direction almost parallel to the the gradient, even with the presence
of modes in every directions in the initial condition. A Benjamin-Feir instablility appears at the
left limit of the periodic structure of configuration 20.

       Figure 21 shows in the first row the cross section of configuration 17 from Fig. 20. In
the second row, we move the Turing point from 1/2 to 1/4 of the domain length, to evaluate if a
translation of the forcing may result in any pulling of reorientation of the pattern. We use the
steady pattern of configuration 17 as the initial condition, for the configuration shown in the
second row. In both cases, the cross section is taken at the middle height (y-direction) of the
domain. We compare the ψ profile with the estimated amplitude of mode B, evaluated by the
steady state solution of the NWS Eq.21, and also with the analytic approximation from Eq. 25.

       As in configuration 1 profile from Fig. 18, the evaluated envelopes refer to modes
parallel to the gradient and not to bent stripes of the pattern, where the angle between the local

Figure 21 - Cross section of configuration 17 of Fig. 20, and of the pattern obtained from the same configuration as initial condition, now run with a ramp of ε where the Turing point is located at 1/4 of the domain length. The same maximum value of ε prescribed for configuration 1 is adopted for the simulation shown in the second row of the present figure. Though associated to straight stripes aligned to the gradient, the envelopes fit well the crests of the patterns, which consist of bended stripes, with the angle between the local wavevector and the gradient continuously varying across the domain.
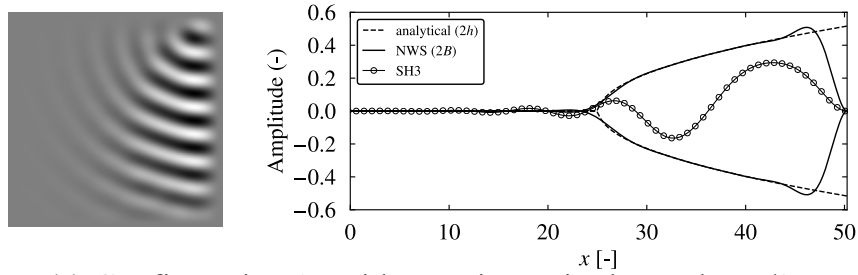
(a) Configuration 17 with a Turing point located at $L/2$.
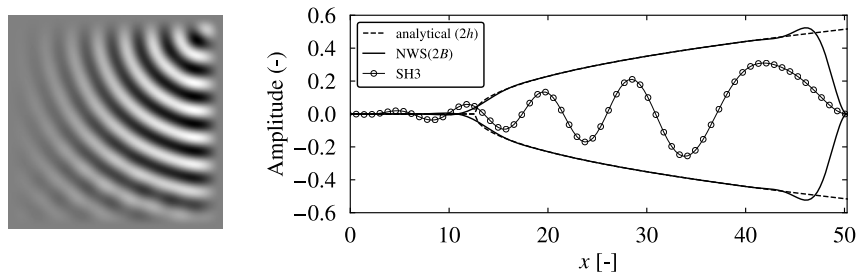
(b) Configuration 17 with a Turing point located at $L/4$.

Source: Original work by the author.

wavevector and the gradient continuously varies across the domain. In spite of this fact, the envelopes qualitatively fit the peaks of the pattern, suggesting that the height of the envelope far of boundaries depends primarily on the local value of ε and not on the direction of the wavevector.

Note that the solution of the NWS Eq. 21 presents an estimate for the envelope on the subcritical region. The results show that a translation of the forcing ramp expands the pattern towards the new location of the Turing point, keeping the original bent form of the pattern in configuration 17. Therefore, bulk and boundary effects still win over gradient effects, and no reorientation is observed.

5.1.3 Sinusoidal forcings

This section presents the results of eigth simulations run from pseudo-random initial conditions with sinusoidal forcings in x. Both GDBC and PBC are prescribed. Sinusoidal forcings are of interest because they allow for multiple subcritical and supercritical regions in

Figure 22 - The results of eight simulations with the SH3 equation, forced with a spatial sinusoidal profile of the control parameter ε. All simulations started from the same pseudo-random initial conditions, shown in the first column. The remaining columns present the steady state, attained when $\dot{L}_1 \leq 5 \times 10^{-7}$. First row: the prescribed profile of the control parameter ε. Second and third rows: GDBC (a), and PBC (b) boundary conditions, respectively.

(a) GDBC

(b) PBC
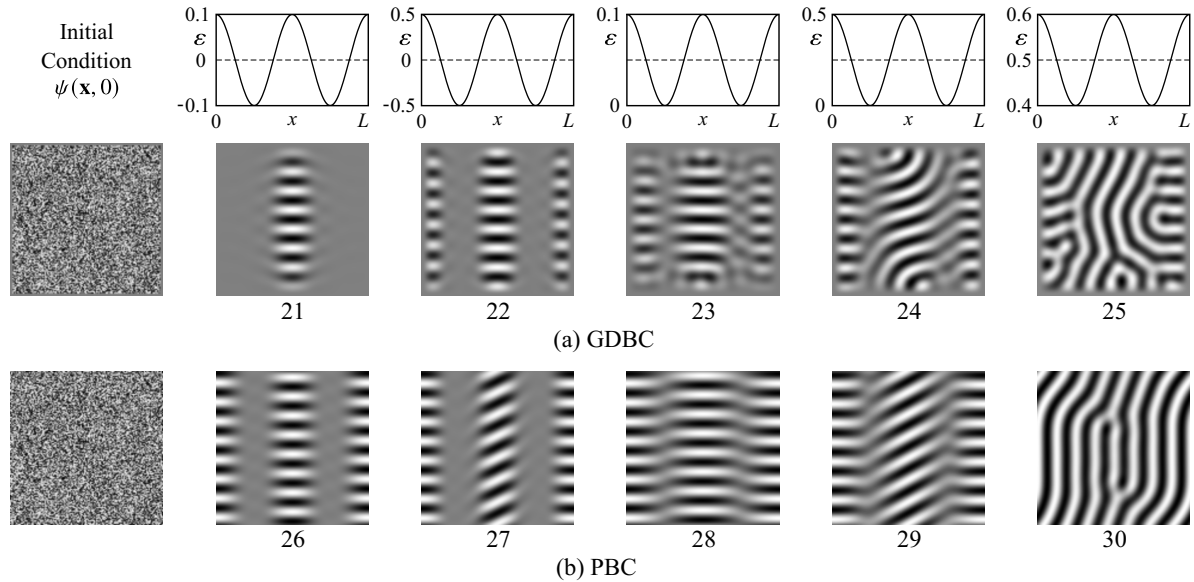
Source: Original work by the author.

a single domain, with multiple Turing points in x. Also, when compared to ramps, periodic forcings better accommodate PBC, so that undesired effects due to a jump of ε at the boundary are not an issue. The results are summarized in Fig. 22, where we present the resulting steady state patterns (labeled as configurations 13-22). The first row displays the distribution of ε forcings, the second patterns obtained by prescribing GDBC, and the third those obtained by prescribing PBC.

Results shown in configurations 21 to 25 (GDBC) and 26 to 30 (PBC) of Fig. 22 evolved either to patterns parallel to gradient, or at least, with regions where the stripes are parallel to the gradient. The orientation effect clearly appears in these simulations, even when the restrictive GDBC are prescribed.

To obtain configuration 21, we used a low amplitude sinusoidal distribution of ε with subcritical regions $(-0.1 \leq \varepsilon \leq 0.1)$. Due to GDBC, we observe the existence of supercritical regions close to the right and left walls where no pattern emerges. A higher amplitude of the forcing, as depicted in configuration 30, leads to the emergence of stripes aligned to the gradient in all supercritical regions, so that a higher ε allows to overcome energy penalizations due to boundary conditions. Configuration 23 of Fig. 22 is run with a sinusoidal forcing added to a constant, so that $\varepsilon \geqslant 0$. No subcritical regions are present in this simulation. A weak structure of small stripes perpendicular to the upper and lower walls emerges at the center of these walls. Several Benjamin-Feir instabilities are also observed. Configuration 24 is run with a similar

sinusoidal forcing, but of higher amplitude. Due to the higher forcing, the structure can more easily accommodate defects. A pattern of winding stripes appear at the central region, with two focus defects showing at the top and at the bottom of this region. We note that the winding form of these stripes comes from the fact that they anchor perpendicularly to the upper and lower walls, while approaching regions of ε close to zero with a parallel alignment. This is in agreement with our previous observation from Fig. 17, that orientational effects due to $\nabla \varepsilon$ become less prevailing as the magnitude of the forcing increases.

Configuration 25 is obtained by increasing the minimum ε even further, so that we have a fluctuating forcing of high magnitude and GDBC. The orientational effect of the gradient is fully dominated by the bulk and boundary effects. A pattern of diagonal stripes with a high density of defects emerges.

The results presented in the third row of Fig. 22 are run with PBC. In the case of configuration 26, a low forcing and the lack of boundaries prevent the emergence of defects. The orientational effect of the gradient prevails and a structure of stripes parallel to the gradient emerges in all supercritical regions. Configuration 27 is similar to the previous, but the sinusoidal forcing presents a higher amplitude. This higher forcing in supercritical regions allows for stripes that deviate from the gradient alignment, and we observe columns of stripes that alternate between parallel and inclined alignments. The steady state for this case strongly depends on the initial distribution of ψ, and once a column of inclined stripes is formed, it is unable to completely reorient in the gradient direction.

Configuration 28 of Fig. 22 presents again a case where the forcing consists of a low amplitude with zero minimum ε. The absence of sidewalls and the relatively low forcing weakens competing effects and pattern aligns accordingly to the gradient. The resulting structure is parallel to the gradient and Benjamin-Feir instabilities are observed at the neighborhood of the Turing point. For configuration 29 we use the same forcing as in configuration 24. The steady state pattern is similar the one of configuration 27, but with stripes occupying the entire domain, as the forcing is non-negative. Lastly, configuration 30 starts from the same forcing as configuration 25, and the resulting winding pattern shows that, even for PBC, $\nabla \varepsilon$ fails to orient the stripes whenever the magnitude of the force remains at large magnitude.

Fig. 23 shows a cross section of the steady state pattern from configuration 30 of Fig. 22. The cross section profile is taken at the middle of the height (y-direction) and is represented by a a line with small circles. To this profile we superposed the pattern envelope of mode B estimated from two approaches: the first one consisted in the steady state solution of Eqs. 22 and 23, for the amplitude B, using a sinusoidal distribution of ε. The so evaluated envelope is represented by a continuous line in Fig. 23. The second evaluation of the envelope is done by using Eq. 25 also adopting a sinusoidal distribution of ε. The envelope is represented by a dashed line in Fig. 23. The two estimated envelopes fit the central part of the pattern cross section, and deviate at the boundaries, which are not taken into account in the derivation of those two curves.

Fig. 24 presents the result of a configuration consisting of a pseudo-random distribution

Figure 23 - Cross section along the x-direction, of the pattern shown in configuration 22 of Fig. 22 (dotted line). The cross section is taken at the middle of the height (y-direction). To the profile obtained directly from the pattern we superpose the envelope of mode B, obtained by two methods: as the steady state solution of Eqs. 22 and 23, adopting a sinusoidal distribution of ε along the x direction and as an estimation of the envelope profile, using Eq. 25.
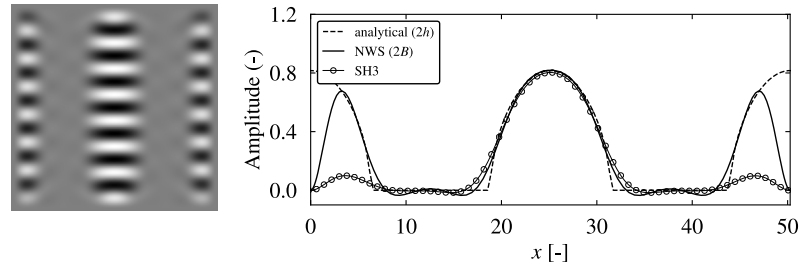
Source: Original work by the author.

Figure 24 - Pattern evolution from pseudo-random initial conditions, subjected to PBC and a diagonal sinusoidal distribution of the control parameter, given by: $\varepsilon(\mathbf{x}) = 0.1 \cos [q_1(x + y)]$. The structure evolve into stripes aligned in the $\nabla \varepsilon$ direction until the steady state is reached.

$t = 0$ $t = 70$ $t = 4435$
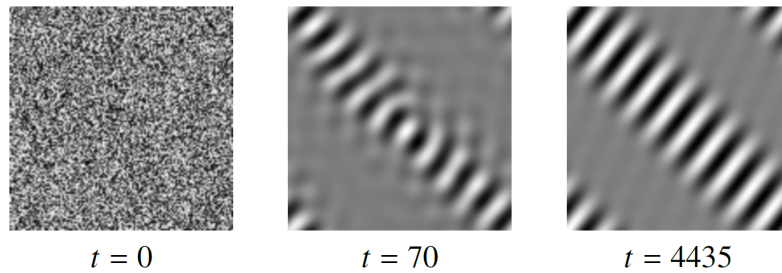
Source: Original work by the author.

Figure 25 - Comparison between $\dot{L}_1$ curves of configurations 22 (GDBC) and 27 (PBC) with sinusoidal forcings. It roughly corresponds to the "normalized" modulus of the time derivative $\partial \psi / \partial t$ and therefore is sensitive not only to the growth of the amplitude, but also to the pattern phase dynamics.
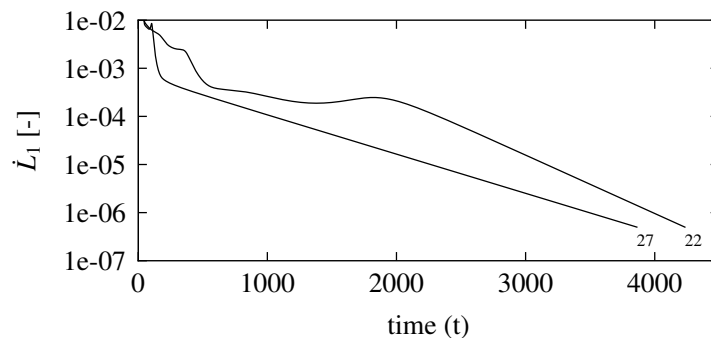
Source: Original work by the author.

of ψ as the initial condition, a sinusoidal forcing along the domain diagonal, and PBC. Lack of boundary effects along with the orientation effect of the gradient, and existence of modes along all direction in the initial condition lead to a pattern of stripes parallel to the diagonal.

Figure 25 shows the $\dot{L}_1 \times t$ curves of selected configurations shown in Fig. 22. These curves present an irregular region at the very begining of the simulations, when the patterns emerges from the pseudo-random initial condition. Most of the pattern growth occurs at this phase. As a result, $\dot{L}_1$ decreases by some orders of magnitude. The evolution proceeds with changes in the phase, and with the amplitude essentially saturated. $\dot{L}_1$ evolves irregularly at much lower level, with peaks occuring at the collapse of defects. This phase is followed, in all cases, by a linear (exponential) decrease of $\dot{L}_1$. We assume that the pattern reached a steady state when $\dot{L}_1$ attains the value 5×10^{-7}. We mention that also the Lyapunov potential decreases exponentially at this phase.

Fig. 26 presents a case of a preexisting structure of stripes along the y-direction and a sinusoidal profile of ε along the diagonal of the domain, using PBC. Despite lacking the restrictive effect of boundary conditions, the gradient is dominated by the initial condition, and the preexisting structure persists. Upon adding a noise $\delta\psi \in (-10^{-2}, 10^{-2})$ to the initial condition, the preexisting structures is destabilized and replaced by a sinusoidal distribution of stripes parallels to the gradient.

5.1.4 Gaussian forcings, and pseudo-random initial conditions

By imposing Gaussian forcings we observe another bulk effect that competes with the gradient in orienting the stripes. Fig. 27 shows the steady state patterns obtained in four simulations, two of them run with a sharper circular gaussian distributions of the control parameter, centered at the middle of the domain and two, with a wider gaussian forcing. GDBC and PBC are considered for each configuration of ε. The four simulations started from the same pseudo-random initial condition adopted in all cases presented in Secs. 5.1.2 and 5.1.3. The adopted Gaussian distribution is given by:

$$\varepsilon\left(\mathbf{x}\right) = Ae^{-R\left((x-x_0)^2 + (y-y_0)^2\right)} . \tag{56}$$

In the first case, configurations 31 (GDBC) and 25 (PBC), we used a sharper distribution of ε with parameters R given in Tab. 4 (R_1 and R_2). For both, the resulting pattern takes the form of a target, with stripes presenting a wavevector parallel to the gradient, $\mathbf{q} \parallel \nabla\varepsilon$, a completely opposite situation with respect to several other cases run from pseudo-random initial conditions using forced with ramps or sinusoidal distributions of ε. The orientation effect of the gradient does not appear in this case, and orientation is dominated by a geometric bulk effect. Due to the disk-form of ε in the two-dimensional domain, a target pattern is the one that fills the supercritical

Figure 26 - Pattern evolution from preexisting vertical stripes, subjected to PBC and a diagonal sinusoidal distribution of the control parameter, given by: $\varepsilon(\mathbf{x}) = F \cos[q_1(x+y)]$, where $q_1 = 0.125q_0$. For (a) $F = 0.1$ and (b) $F = 0.5$, the preexisting structure persists, and dominates the orientation effect of the gradient. (c) Upon adding a perturbation in the form of a uniform distribution ranging from -10^{-2} to 10^{-2} to the initial condition, the preexiting structure collapses and is replaced by stripes parallels to the gradient. (d) The time evolution of $\dot{L}_1$ for the latter is shown and this simulation proceeded until $\dot{L}_1 \leqslant 5 \times 10^{-9}$.

$t = 0$ 　　　 $t = 150$ 　　　 $t = 310$

(a)

$t = 0$ 　　　 $t = 20$ 　　　 $t = 214$

(b)

$t = 0$ 　　　 $t = 10000$ 　　　 $t = 35935$

(c)

(d)
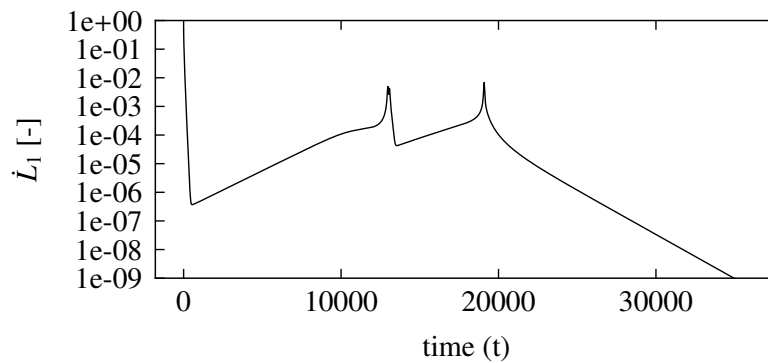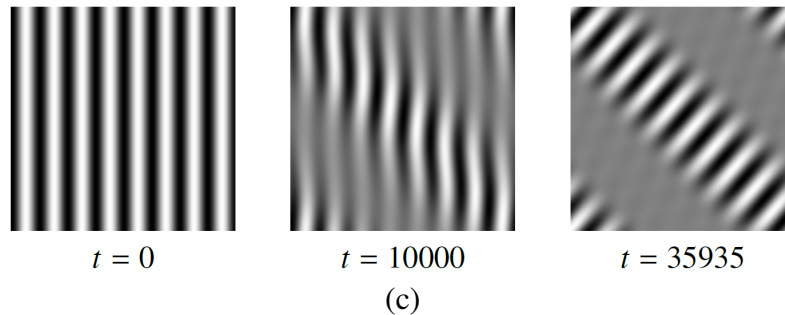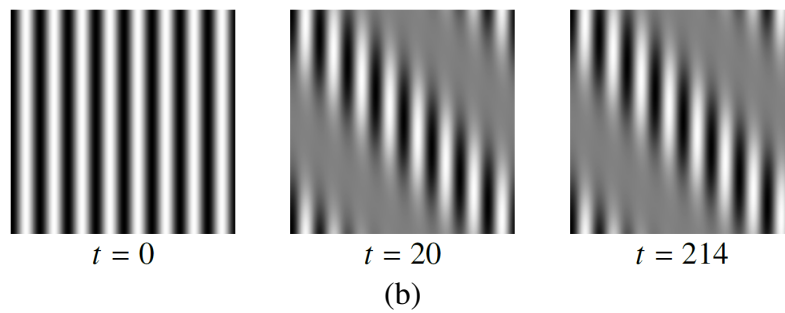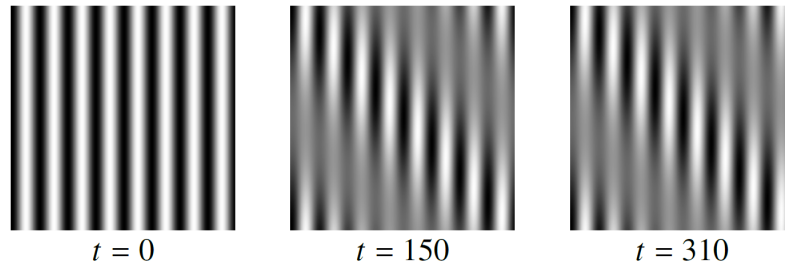
Figure 27 - The results of four simulations with the SH3 equation, forced with a Gaussian distribution of ε. All simulations started from the same pseudo-random initial conditions, shown in the first column. Configurations 31 and 32 are run with GDBC, while PBC are prescribed for configurations 33 and 33.

(a) GDBC

(b) PBC
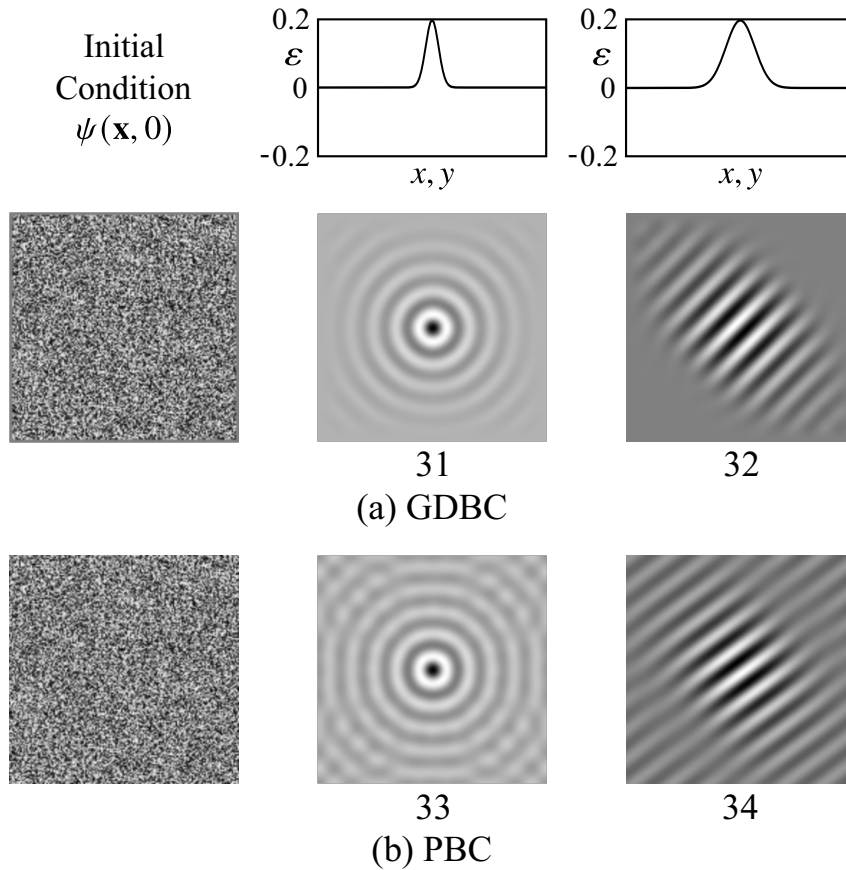
Source: Original work by the author.

region while minimizing defects, which is a geometric compatibility effects. Otherwise, if stripes are to orient accordingly to the $\nabla\varepsilon$, the resulting pattern would cointain a large ammount of defects (dislocations) to accomodate such orientation, increasing significantly the energy of the configuration. Therefore, target patterns minimizes the Lyapunov potential, in spite of being penalized by the control parameter gradient.

A second case with a wider Gaussian forcing is shown in Fig. 27, configurations 32 (GDBC) and 33 (PBC), with parameters R given in Tab. 4 (R_1 and R_2). This case corresponds to a forcing with a sharper distribution of Fourier modes, therefore a smaller range of modes persists in the steady state pattern. We observe that a pattern of stripes with wavevector aligned with the diagonal of the domain appears. The pattern extends for a longer distance in this diagonal direction, even invading the subcritical region, for both GDBC nad PBC. The effect is due to the fact that the hardest direction for modulation of the amplitude occurs in the direction of the wavevector, whereas the easiest direction is the perpendicular one. This property of periodic patterns results in amplitudes modulated in compliance with Newell-Whitehead-Segel

equations (NEWELL; WHITEHEAD, 1969; SEGEL, 1969).

5.2 Competition between the gradient, boundary and bulk effects – SH23 and SH35

In this section, we briefly explore two other forms of the SH equation with additional nonlinearities, in order to numerically evaluate the effects of altering a bifurcation diagram on the orientation of resulting patterns. As mentioned before, Eq. 8 can be addressed to as SH23 for $\gamma = 0$, and $\zeta, \beta \neq 0$. Analogously, we refer to it as SH35 for $\zeta = 0$, and $\gamma, \beta \neq 0$. The numerical scheme follows the semi-implicit approach described in Appendix 3 with minor modifications depending on which nonlinear terms are present.

Accordingly to the simulations presented in the previous sections and Refs. (PONTES, 1994; CHRISTOV et al., 1997; CHRISTOV; PONTES, 2002; PONTES; WALGRAEF; CHRISTOV, 2008), GDBC introduces additional restraints for the patterns, i.e, stripes anchoring perpendicularly to sidewalls. We adopt PBC to study interacting bulk effects for SH23 in the presence of a nonzero $\nabla \varepsilon$. For small positive ε, hexagonal patterns are the minimum energy state, which destabilizes when ε is increased and stripe patterns become energetically favored. The coexistence of both structures with a nonuniform forcing is addressed by Hilali et al. (HILALI et al., 1995), where stripes formed with $\mathbf{q} \parallel \nabla \varepsilon$, contrary to our results for SH3. To clarify if such effect observed for SH23 is induced by initial conditions (an initial ramp in ψ, in their case), and assess how $\nabla \varepsilon$ interferes in the hexagon to stripe transition, we perform simulations for SH23 using different initial conditions and ramps for ε. Numerical results are shown in Fig. 28, using $\zeta = 0.65$ and $\beta = 1$, in which we observe the possibility of coexistence between hexagons and stripes. The nonuniform forcings considered are the following ramps: $-0.5 \leqslant \varepsilon(\mathbf{x}) \leqslant 0.5$ and $0.0 \leqslant \varepsilon(\mathbf{x}) \leqslant 0.5$. Three configurations for each forcing are considered, starting from pseudo-random initial conditions and preexisting patterns (horizontal and vertical stripes, respectively).

Configurations 43 and 44 started from pseudo-random initial conditions, and configurations 37, 38, 39 and 40 had their preexisting condition perturbed with a pseudo-random noise ranging from -10^{-6} to 10^{-6} with an uniform distribution. In the absence of perturbations, the initial condition is preserved, *i.e*, hexagon patterns do not emerge. The results show that, in the presence of a $\nabla \varepsilon \neq 0$, the preexisting patterns are unstable, and we observe regions where stripes decay to $\psi = 0$ or evolve towards hexagons.

First, we compare configurations 43, 37 and 39, where a ramp ranging from $\varepsilon = -0.5$ to $\varepsilon = 0.5$ is employed. Starting from a pseudo-random initial condition, we observe that stripes with $\mathbf{q} \perp \nabla \varepsilon$ appear in the region of positive ε, with a weakly formed hexagonal structure close to $\varepsilon = 0$. Configuration 37 show that when a preexisting structure of stripes with $\mathbf{q} \perp \nabla \varepsilon$ is perturbed, stripes in the positive ε region remain perfectly aligned to the gradient, and no transition to hexagons is observed. In configuration 39 we see that by perturbing an initial

condition of stripes with $\mathbf{q} \parallel \nabla\varepsilon$, the remaining stripes did not reorient according to $\nabla\varepsilon$, and (opposite to configuration 37) a well formed column of hexagons appeared for regions of small ε. This is a consequence of the higher energy associated to stripes when $\mathbf{q} \parallel \nabla\varepsilon$, as compared in Fig. 17, so that for small ε a stripe to hexagon transition is promoted. For configurations 44, 38 and 40, where the ramp ranges from $\varepsilon = 0$ to $\varepsilon = 0.5$, we note that due to the smaller $\nabla\varepsilon$ this gradient has a weaker effect on inducing stripe pattern alignment. In configuration 44, we do not see alignment starting from a pseudo-random initial condition, while in configuration 38, even though the preexisting pattern is made of stripes with $\mathbf{q} \perp \nabla\varepsilon$, hexagons still emerged in the $0 < \varepsilon < 0.25$ region (opposite to configuration 37).

Finally, we present numerical results for the SH35 equation in the presence of a control parameter gradient, using $\beta = 3$, and $\gamma = 1$. The $\psi = 0$ to stripe transition in SH35 is associated to a subcritical bifurcation, so that there is a jump of the amplitude in this transition. Due to the symmetry in the energy structure associated to SH35, the bifurcation parameter presents a coexistence value $\varepsilon_c = -27\beta^2/160\gamma$ for which both stripes and $\psi = 0$ states have approximately zero energy density (SAKAGUCHI; BRAND, 1996; VITRAL; LEO; VIÑALS, 2019). For $\varepsilon > \varepsilon_c$, stripes are energetically favored, while for $\varepsilon < \varepsilon_c$ the equilibrium state is $\psi = 0$. A consequence of the subcritical bifurcation is that even in $\varepsilon > \varepsilon_c$ regions, stripes do not form from a pseudo-random initial condition for finite values of ε_c. Therefore, in the SH35 case we adopt a square pattern as initial condition, of the type $\psi = A\cos(q_0 x) + B\cos(q_0 y)$, in order to evaluate the $\nabla\varepsilon$ effect on filtering the pattern.

For obtaining configurations 41 and 42, we use GDBC, while for configurations 43 and 44, we use PBC. For the chosen set of parameters $\varepsilon_c \approx -1.52$. With a ramp ranging from $\varepsilon = -3$ up to $\varepsilon = 0$, for both GDBC (away from the boundary) and PBC the y direction mode is filtered, and the resulting structures present stripes with $\mathbf{q} \perp \nabla\varepsilon$ for $\varepsilon > \varepsilon_c$, and $\psi = 0$ for $\varepsilon < \varepsilon_c$. By changing the ramp to $\varepsilon = -1.8$ up to $\varepsilon = 0$, we see in configuration 44 (PBC) that away from the boundaries the structure perfectly aligns according to $\nabla\varepsilon$. However, in configuration 42 we note that by decreasing the ramp inclination, orientation effects due to boundary conditions become stronger in comparison to $\nabla\varepsilon$, as they mostly dictate the resulting pattern. From our simulations using SH35 with PBC, we observed that patterns tend to orient more strongly according to $\nabla\varepsilon$ than in the case of SH3 or SH23, which is presumably associated to the subcritical nature of the bifurcation.

Figure 28 - The results of six simulations with the SH23 equation, forced with a spatial ramp of the control parameter ε indicated in the first row. The parameters of the SH23 are: $\zeta = 0.65$, $\beta = 1$ and $\gamma = 1$. Initial conditions for configurations 37, 38, 39 and 40 are perturbed so that the remaining stripes share the domain with hexagons, as expected for this range of parameters.
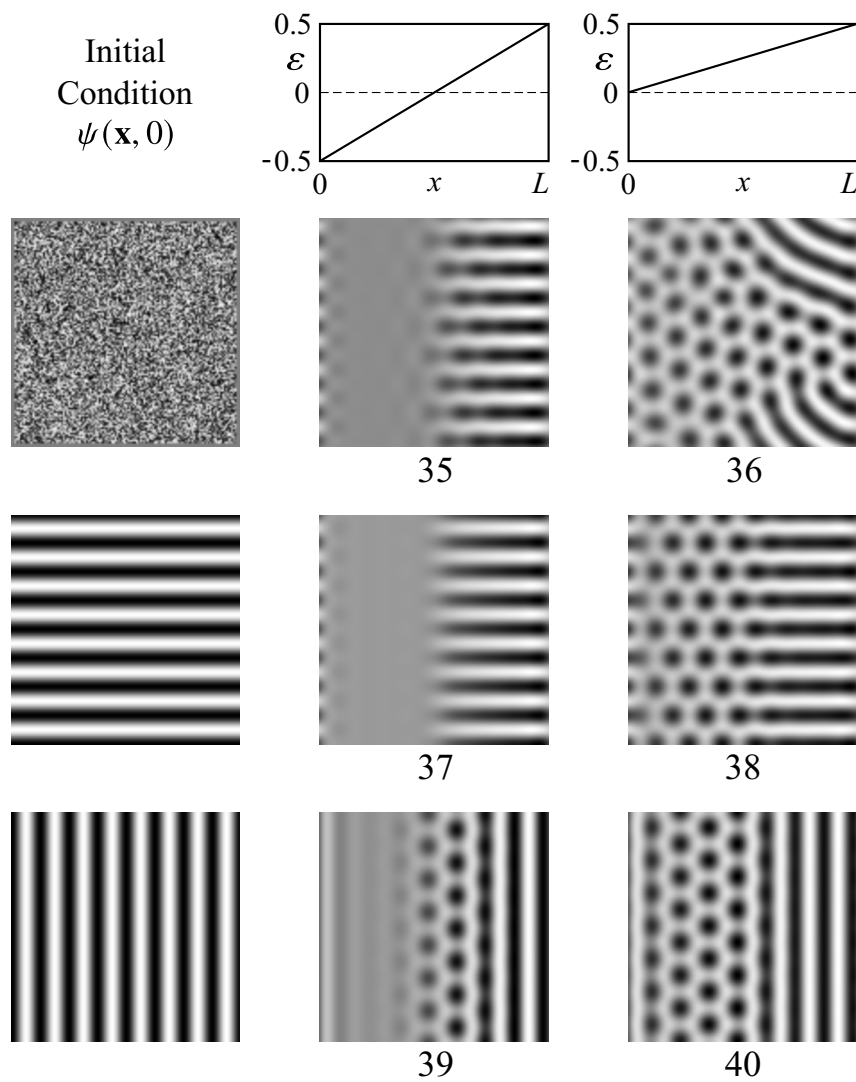
Figure 29 - The results of four simulations with the SH35 equation, forced with a spatial ramp of the control parameter ε. All simulations started from the same preexisting square pattern ($\psi = A\cos(q_0 x) + B\cos(q_0 y)$), shown in the first column. The remaining columns present the steady state. First row: the prescribed profile of the control parameter ε. Second and third rows: results for GDBC, and PBC, respectively. Results of the second row show that boundary effects dominate the orientaion effect when GDBC are prescribed. In the third row, the absence of boundary effects allows the dominance of the orientation effect of the gradient.

(a) GDBC

(b) PBC
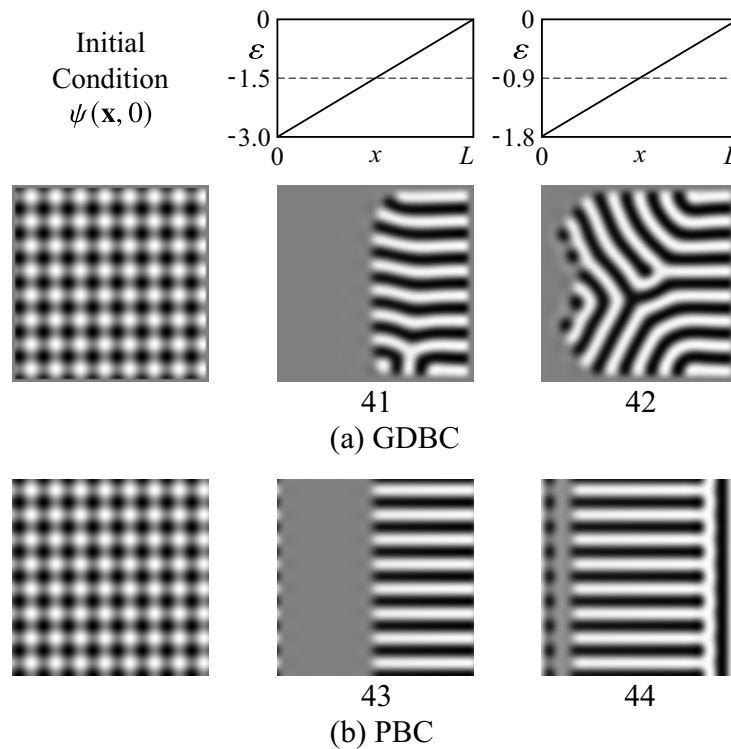
Source: Original work by the author.

CONCLUSIONS

In this thesis, we extended a numerical scheme proposed by Christov & Pontes (PONTES; WALGRAEF; CHRISTOV, 2008) to investigate pattern formation modeled by the cubic Swift-Hohenberg equation SH3 in two dimensions. The original scheme presents second order representation of all derivatives, strict implementation of the associated Lyapunov functional, rigid boundary conditions (GDBC), and a semi-implicit assignment of the terms.

The present work includes the quintic version of the Swift-Hohenberg equation and periodic boundary conditions (PBC) for both the cubic and the quintic versions of the model. The scheme retains all characteristics of the original one, namely strict representation of the Lyapunov functional, unconditional stability, and second order representation of all derivatives. In addition, we also included a convergence analysis, new verification tests, and an initial evaluation of the effect of nonuniform forcings in the form of spatial ramps and of gaussian distributions of the control parameter ϵ. Among the verification tests, the convergence analysis confirmed the truly second-order accuracy of the scheme both in space and time and the existence of localized structures developed in the framework of the SH35 equation even with nonuniform forcings. The numerical experiments conducted in this work suggest the existence of effects and the onset of patterns not addressed in the literature. Both questions will be the object of a forthcoming paper.

The conducted tests confirmed the robustness of the developed tool for pursuing the investigation of the pattern formation through the parabolic Swift-Hohenberg equation presenting various nonlinear terms, including nonuniform forcings.

This work also addressed the orientation effect due to gradients of the control parameter ε in stripe patterns using the Swift-Hohenberg dynamics, and how it fares against competing effects. A weakly nonlinear analysis confirms and extends existing results showing that stripes tend to align to the gradient. We show that stripes with wavevector $\mathbf{q}$ perpendicular to $\nabla\varepsilon$ are stable and correspond to a lower energy state than stripes with $\mathbf{q}$ parallel to $\nabla\varepsilon$, which are unstable near the Turing point. However, our main numerical results show that the orientation effect of the gradient, though existing, does not always prevail when facing competition with other bulk, boundary, geometric, and periodic effects due to computational domains. This competition leads to the emergence of a rich dynamics, as apparent in our results, which strongly depends on the magnitude of the forcing and initial conditions (preexisting patterns or pseudo-random). In this sense, the various forms of forcing and initial conditions addressed in this work, while extensive, do not cover the full range of possible cases.

Among our most representative results, we cite simulations where, starting from a structure of stripes with wavevector $\mathbf{q}$ perpendicular to $\nabla\varepsilon$, the initial pattern is preserved, and cases where this orientation is compromised by competing effects. Even starting from a structure of stripes with $\mathbf{q}$ parallel to the gradient, we found cases where the initial pattern persists. However, upon introducing a finite pseudo-random perturbation on the initial conditions, either $\nabla\varepsilon$ fully reorients

the stripes or competing effects interfere, reshaping the pattern (e.g. introducing defects). Forcing with a gaussian distribution of ε resulted, in one case, in a target structure of stripes perpendicular to the gradient ($\mathbf{q} \parallel \nabla\varepsilon$) and, in other, in straight stripes perpendicular to the domain main diagonal. In the former, the target pattern results from a geometric constraint, as a pattern with $\mathbf{q} \perp \nabla\varepsilon$ would imply in a large density of defects (higher energy). In the latter, the elongated pattern along the domain main diagonal complies with a well known effect, which states that the most difficult direction for modulation is the one of the wavevector (NEWELL; WHITEHEAD, 1969; SEGEL, 1969).

An estimation for the local amplitude of the patterns could was derived in the form of a NWS equation, function of the nonuniform forcing $\epsilon(\mathbf{x})$. Its steady state solution, $h = [\varepsilon(\mathbf{x})/-3\beta]^{1/2}$(Eq. 25), neglects diffusion of the amplitude and still represents a satisfactory approximation of its envelope far from the boundaries and the Turing point. This estimation is more accurate when the pattern preserves a dominant mode in the x (or y) direction, but even when there are other modes present, the approximation is satisfactory.

In summary, we observed that the orientation effect of the gradient prevailed in many, but not all, of the explored configurations, either starting from a preexisting structure of stripes parallel or perpendicular to the gradient, or with a pseudo-random initial condition. The orientation effect is relevant for many physical systems presenting periodic patterns, such as in developmental biology (HISCOCK; MEGASON, 2015; RUPPERT; ZIEBERT; ZIMMERMANN, 2020), smectic mesophases (VITRAL; LEO; VIÑALS, 2019), and localized sand patterns (AUZERAIS et al., 2016), whose dynamics have been studied by Swift-Hohenberg type equations, but present mechanisms of stripe orientation that are not well understood.

REFERENCES

AMUNDSON, K.; HELFAND, E. Quasi-static mechanical properties of lamellar block copolymer microstructure. *Macromolecules*, ACS Publications, v. 26, n. 6, p. 1324–1332, 1993.

AUZERAIS, A.; JARNO, A.; EZERSKY, A.; MARIN, F. Formation of localized sand patterns downstream from a vertical cylinder under steady flows: Experimental and theoretical study. *Physical Review E*, APS, v. 94, n. 5, p. 052903, 2016.

BOYD, J. P. *Chebyshev and Fourier spectral methods*. Courier Corporation, 2001.

BRAZOVSKII, S.; DMITRIEV, S. Phase transitions in cholesteric liquid crystals. *Zh. Eksp. Teor. Fiz*, v. 69, p. 979–989, 1975.

BURKE, J.; KNOBLOCH, E. Localized states in the generalized swift-hohenberg equation. *Physical Review E*, APS, v. 73, n. 5, p. 056211, 2006.

CASTETS, V.; DULOS, E.; BOISSONADE, J.; KEPPER, P. D. Experimental evidence of a sustained standing turing-type nonequilibrium chemical pattern. *Physical Review Letters*, The American Physical Society, v. 64, 1990.

CHANDRASEKHAR, S. *Hydrodynamics and Hydrodynamic Stability, Clarendon*. Oxford, 1961.

CHRISTOV, C.; PONTES, J. Numerical scheme for Swift-Hohenberg equation with strict implementation of Lyapunov functional. *Mathematical and Computer Modelling*, Elsevier Science, v. 35, 2002.

CHRISTOV, C.; PONTES, J.; WALGRAEF, D.; VELARDE, M. Implicit time splitting for fourth-order parabolic equations. *Computer Methods in Applied Mechanics and Engineering*, Elsevier Science, v. 148, 1997.

COELHO, D. L.; VITRAL, E.; PONTES, J.; MANGIAVACCHI, N. Numerical scheme for solving the nonuniformly forced cubic and quintic Swift-Hohenberg equations strictly respecting the Lyapunov functional. *Submitted to Journal of Computational and Applied Mathematics*, 2020.

COLEMAN, R. *Rippled clouds - Flickr Webpage*. 2009. Disponível em: <https://www.flickr.com/photos/61603002@N07/5640249650/>.

CROSS, H. G. M. *Pattern Formation and Dynamics in Nonequilibrium Systems*. 1. ed. Cambridge University Press, 2009. ISBN 0521770505,9780521770507. Disponível em: <http://gen.lib.rus.ec/book/index.php?md5=677587B21697E0C4974689E2C0D4A469>.

CROSS, M. Boundary conditions on the envelope function of convective rolls close to onset. *The Physics of Fluids*, American Institute of Physics, v. 25, n. 6, p. 936–941, 1982.

CROSS, M. Ingredients of a theory of convective textures close to onset. *Physical Review A*, APS, v. 25, n. 2, p. 1065, 1982.

CROSS, M. C.; HOHENBERG, P. C. Pattern formation outside of equilibrium. *Rev. Modern Phys.*, v. 65, p. 851, 1993.

DOERK, G. S.; YAGER, K. G. Rapid ordering in "wet brush" block copolymer/homopolymer ternary blends. *ACS Nano*, 12 2017.

DOUGLAS, J.; RACHFORD., H. H. On the numerical solution of heat conduction problems in two and three space variables. *Trans. Amer. Math. Soc.*, 1956.

ELDER, K. R.; GRANT, M. Modeling elastic and plastic deformations in nonequilibrium processing using phase field crystals. *Physical Review E*, APS, v. 70, n. 5, p. 051605, 2004.

ELDER, K. R.; KATAKOWSKI, M.; HAATAJA, M.; GRANT, M. Modeling elasticity in crystal growth. *Physical review letters*, APS, v. 88, n. 24, p. 245701, 2002.

ELSEY, M.; WIRTH, B. A simple and efficient scheme for phase field crystal simulation. *ESAIM: Mathematical Modelling and Numerical Analysis*, EDP Sciences, v. 47, n. 5, p. 1413–1432, 2013.

GLANSDORFF, P.; PRIGOGINE, I. Structure, stabilité et fluctuations. Masson, 1971.

GREENSIDE, H. S.; COUGHRAN, W. M. Nonlinear pattern formation near the onset of Rayleigh-Bénard convection. *Physical Review A*, v. 30, n. 1, p. 398–428, 1984.

GRUBB, C. *Anna the Grevy's Zebra is Pregnant - Reid Park Zoo Webpage*. 2020. Disponível em: <https://reidparkzoo.org/blog/anna-the-grevys-zebra-is-pregnant/>.

HAKEN, H. *Synergetics*. 1981.

HAKEN, H. *Synergetics: An Introduction. Equilibrium Phase Transitions and Self-Organization in Physics, Chemistry and Biology*. 1983.

HILALI, M. F.; MÉTENS, S.; BORCKMANS, P.; DEWEL, G. Pattern selction in the generalized swift-hohenberg model. *Physical Review E*, v. 51, n. 3, p. 2046–2052, April 1995.

HISCOCK, T. W.; MEGASON, S. G. Orientation of turing-like patterns by morphogen gradients and tissue anisotropies. *Cell systems*, Elsevier, v. 1, n. 6, p. 408–416, 2015.

HOYLE, R. B. *Pattern formation: an introduction to methods*. Cambridge University Press, 2006.

KRINSKY, V. I. *Self-organization: autowaves and structures far from equilibrium: proceedings of an international symposium, Pushchino, USSR, July 18-23, 1983*. Springer, 1984. v. 28.

LANDAU, L. D.; LIFSHITZ, E. M. *Statistical Physics*. 3. ed. Oxford: Elsevier Butterworth-Heinemann, 1980. v. 5. (Course of Theoretical Physics, v. 5). ISBN 978-0-7506-3372-7.

LANGER, J.; MÜLLER-KRUMBHAAR, H. Theory of dendritic growth—i. elements of a stability analysis. *Acta Metallurgica*, Elsevier, v. 26, n. 11, p. 1681–1687, 1978.

LANGER, J. S. Instabilities and pattern formation in crystal growth. *Reviews of modern physics*, APS, v. 52, n. 1, p. 1, 1980.

LEE, H. G. An energy stable method for the swift–hohenberg equation with quadratic–cubic nonlinearity. *Computer Methods in Applied Mechanics and Engineering*, Elsevier, v. 343, p. 40–51, 2019.

LEE, H. G.; KIM, J. A simple and efficient finite difference method for the phase-field crystal equation on curved surfaces. *Computer Methods in Applied Mechanics and Engineering*, Elsevier, v. 307, p. 32–43, 2016.

LI, Y.; KIM, J. An efficient and stable compact fourth-order finite difference scheme for the phase field crystal equation. *Computer Methods in Applied Mechanics and Engineering*, Elsevier, v. 319, p. 194–216, 2017.

MALOMED, B. A.; NEPOMNYASHCHY, A. A. Two-dimensional stability of convection rolls in the presence of a ramp. *Europhysics Letters (EPL)*, IOP Publishing, v. 21, n. 2, p. 195–200, jan 1993. Disponível em: <https://doi.org/10.1209%2F0295-5075%2F21%2F2%2F013>.

MANNEVILLE, P. *Non-equilibrium Structures and Weak Turbulence*. Academic Press: San Diego, CA, USA, 1990. ISBN 0-12-469260-5.

MEYER, C. W.; CANNELL, D. S.; AHLERS, G. Hexagonal and roll flow patterns in temporally modulated rayleigh-bénard convection. *Physical Review A*, The American Physical Society, v. 45, 6 1992. Disponível em: <http://gen.lib.rus.ec/scimag/index.php?s=10.1103/PhysRevA.45.8583>.

MORGAN, D.; DAWES, J. H. The swift-hohenberg equation with a nonlocal nonlinearity. *Physica D*, Elsevier, v. 270, p. 60–80, 2014.

NEWELL, A. C.; WHITEHEAD, J. A. Finite bandwidth, finite amplitude convection. *J. Fluid Mech.*, v. 38, p. 279–303, 1969.

PONTES, J. *Pattern formation in spatially ramped Rayleigh-Bénard systems*. Tese (Doutorado) — Free University of Brussels, Brussels, Belgium, April 1994.

PONTES, J. et al. *Fenômenos de Transferência com Aplicacões Ciências Físicas e a Engenharia – Volume 2: Aplicações*. SBM – Sociedade Brasileira de Matemática, 2018. ISBN 978-85-8337-153-3.

PONTES, J.; WALGRAEF, D.; CHRISTOV, C. I. Pattern formation in spatially ramped rayleigh-bénard systems. *Journal of Computational Interdisciplinary Sciences*, v. 1, n. 1, p. 11–32, 2008.

PRIGOGINE, I.; LEFEVER, R. Symmetry breaking instabilities in dissipative systems. ii. *The Journal of Chemical Physics*, American Institute of Physics, v. 48, 1968.

PROVATAS, N.; ELDER, K. *Phase-Field Methods in Materials Science and Engineering*. Wiley, 2010. ISBN 3527407472,9783527407477.

PROVATAS, N.; GREENWOOD, M.; ATHREYA, B.; GOLDENFELD, N.; DANTZIG, J. Multiscale modeling of solidification: phase-field methods to adaptive mesh refinement. *International Journal of Modern Physics B*, World Scientific, v. 19, n. 31, p. 4525–4565, 2005.

ROACHE, P. J. Code verification by the method of manufactured solutions. *J. Fluids Eng.*, v. 124, n. 1, p. 4–10, 2002.

ROY, C. J. Review of code and solution verification procedures for computational simulation. *Journal of Computational Physics*, Elsevier, v. 205, n. 1, p. 131–156, 2005.

RUPPERT, M.; ZIEBERT, F.; ZIMMERMANN, W. Nonlinear patterns shaping the domain on which they live. *New Journal of Physics*, IOP Publishing, v. 22, n. 5, p. 052001, 2020.

SAKAGUCHI, H.; BRAND, H. R. Stable localized solutions of arbitrary length for the quintic Swift-Hohenberg equation. *Physica D*, v. 97, n. 1-3, p. 274–285, 1996.

SALVADOR, G. *Ripple marks on the sand of Idhan Murzuq, Libya - SAATCHI ART Webpage*. 2020. Disponível em: <https://www.saatchiart.com/art/ Photography-ripple-marks-on-the-sand-of-Idhan-Murzuq-Libya-Limited-Edition-of-10/ 1607043/7793885/view>.

SEGEL, L. A. Distant sidewalls cause low amplitude modulation of cellular convection. *Journal of Fluid Mechanics*, v. 38:1, p. 203–224, 1969.

SRULJES, J. A. *Zellularkonvection in Behältern mit Horizontalen Temperauregradienten*. Tese (Doutorado) — Fakultät für Machinenbau, Univ. Karlsruhe, Karlsruhe, 1970.

SWIFT, J.; HOHENBERG, P. C. Hydrodynamic fluctuations at the convective instability. *Physical Review A*, The American Physical Society, v. 15, 1977.

TURING, A. M. The chemical basis of morphogenesis. *Philosophical Transactions Biological Sciences*, The Royal Society, v. 237, 1952. Disponível em: <http: //gen.lib.rus.ec/scimag/index.php?s=10.1098/rstb.1952.0012>.

VITRAL, E.; LEO, P. H.; VIÑALS, J. Role of gaussian curvature on local equilibrium and dynamics of smectic-isotropic interfaces. *Physical Review E*, APS, v. 100, n. 3, p. 032805, 2019.

VITRAL, E.; WALGRAEF, D.; PONTES, J.; ANJOS, G.; MANGIAVACCHI, N. Nano-patterning of surfaces by ion sputtering: Numerical study of the anisotropic damped Kuramoto-Sivashinsky equation. *Computational Materials Science*, Elsevier Science, v. 146, 2018.

WALGRAEF, D. *Spatio-Temporal Pattern Formation: With Examples from Physics, Chemistry, and Materials Science*. 1. ed. Springer-Verlag New York, 1997. (Partially Ordered Systems). ISBN 978-1-4612-7311-0,978-1-4612-1850-0.

WALTON, I. On the onset of Rayleigh-Bénard convection in a fluid layer of slowly increasing depth. *Studies in Applied Mathematics*, Wiley Online Library, v. 67, n. 3, p. 199–216, 1982.

WALTON, I. The onset of cellular convection in a shallow two-dimensional container of fluid heated non-uniformly from below. *Journal of Fluid Mechanics*, Cambridge University Press, v. 131, p. 455–470, 1983.

WANG, J.; ZHAI, S. A fast and efficient numerical algorithm for the nonlocal conservative Swift–Hohenberg equation. *Mathematical Problems in Engineering*, Hindawi, 2020.

YANENKO, N. N.; HOLT, M. *The Method of Fractional Steps*. Springer, 1971. ISBN 3540052720, 9783540052722.

ZHABOTINSKI, A. Periodic oxidation reactions in the liquid phase. In: *Dokl. Akad. Nauk SSSR*. 1964. v. 157, p. 701–704.

Appendices

APPENDIX A – Pattern formation in Rayleigh-Bénard systems: an overview of the Rayleigh instability mechanism

An example of pattern formation in hydrodynamical systems is the Rayleigh-Bénard convection. It is a type of natural convection, occurring in a plane horizontal thin layer of fluid heated from below, in which the fluid develops a regular pattern of convection cells known as Bénard cells. An experimental set up is illustrated below:

Figure 30 - Schematic convection rolls in the Rayleigh-Bénard experiment.
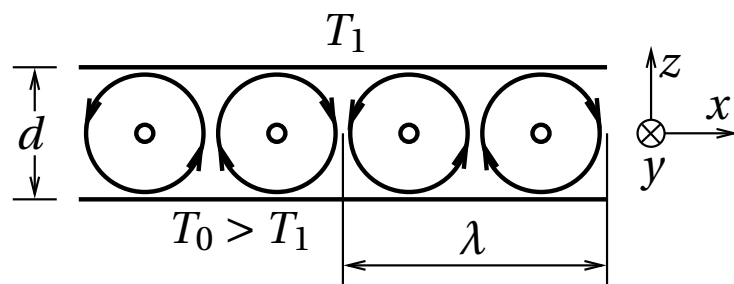
Source: Original work by the author.

The classical mathematical approach for describing the emergence of convection rolls consists of the Oberbeck-Boussinesq (OB) equations. The mathematical formalism shown in this appendix follows some classical notation and derivations from the literature (CHANDRASEKHAR, 1961; SWIFT; HOHENBERG, 1977; HAKEN, 1981; PONTES et al., 2018). Furthermore, some useful insights about the instability mechanism will be provided along with the reduction of the full dynamics to a simplified model performed by Swift and Hohenberg (1977).

A.1 **Boussinesq equations**

Rayleigh-Bénard convection is mathematically modeled by continuity, Navier-Stokes, and heat equations. They are derived from the mass, momentum, and energy balance (conservation) principles, respectively. For the sake of simplicity, and accordingly to the classical literature, we consider the Boussinesq approximation, i.e., we adopt a incompressible fluid, and that variations in fluid properties other than density ρ are ignored, and the density only appears when it is multiplied by the gravitational acceleration (**g**). Therefore, the Boussinesq approximation states that the density variation is only important in the buoyancy term. Furthermore, we consider that density variations are assumed to have a fixed part and another part that has a linear dependence on temperature. It is worth noting that density variations are not sufficient to significantly change

Table 5 - Variables and fluid properties for the Boussinesq equations (SI base unit adopted).

Variables	Description	Fluid properties	Description
$\mathbf{v}(\mathbf{x}, t)$	velocity vector	ν	cinematic viscosity
$T(\mathbf{x}, t)$	temperature field	α	diffusivity coefficient
p	pressure	ρ	density
-	-	β	coefficient of thermal expansion

Source: Original work by the author.

a particle's mass and, consequently, the inertial term. Considering the stated hypothesis, the model consists of the following continuity, Navier-Stokes, and heat equations, respectively:

$$\nabla \cdot \mathbf{v} = 0 , \tag{57a}$$

$$\rho_0 \frac{D\mathbf{v}}{Dt} = -\nabla p + \rho_0 \nu \nabla^2 \mathbf{v} + \rho_0 \left[1 - \beta(T - T_0)\right] \mathbf{g} , \tag{57b}$$

$$\frac{DT}{Dt} = \alpha \nabla^2 T , \tag{57c}$$

where the variables and fluid properties are described in Table 5, and the material derivative (operator) can be expressed as: $D/Dt = (\partial/\partial t + \mathbf{v} \cdot \nabla)$. For convenience, we rewrite the Boussinesq Eqs. (57) with index notation (Einstein's convention):

$$\frac{\partial v_i}{\partial x_i} = 0 ; \tag{58a}$$

$$\rho_0 \left(\frac{\partial v_i}{\partial t} + v_j \frac{\partial v_i}{\partial x_j} \right) = -\frac{\partial p}{\partial x_i} + \rho_0 \nu \frac{\partial^2 v_i}{\partial x_j \partial x_j} + \rho_0 \left[1 - \beta(T - T_0)\right] g_i ; \tag{58b}$$

$$\frac{\partial T}{\partial t} + v_j \frac{\partial T}{\partial x_j} = \alpha \frac{\partial^2 T}{\partial x_j \partial x_j} . \tag{58c}$$

The variables from equations can be scaled as

$$t = \frac{d^2}{\alpha} t^* , \quad x_i = d\, x_i^* , \quad v_i = \frac{\beta g |\Delta T_0| d^2}{\nu} v_i^* ,$$

$$p = \rho_0 \left(\frac{\beta g |\Delta T_0| d^2}{\nu} \right)^2 p^* , \quad T = T_0 + |\Delta T_0|(T^* - 1) .$$

Now we write a dimensionless form of the Boussinesq equations:

$$\frac{\partial v_i}{\partial x_i} = 0 ; \tag{59a}$$

$$\frac{1}{Pr}\left(\frac{\partial v_i}{\partial t} + Ra\, v_j \frac{\partial v_i}{\partial x_j}\right) = -\frac{Ra}{Pr}\frac{\partial p}{\partial x_i} + \frac{\partial^2 v_i}{\partial x_j \partial x_j} + \left[\frac{1}{\beta|\Delta T_0|} - (T-1)\right]\kappa_i ; \tag{59b}$$

$$\frac{\partial T}{\partial t} + Ra\, v_j \frac{\partial T}{\partial x_j} = \alpha \frac{\partial^2 T}{\partial x_j \partial x_j} . \tag{59c}$$

We now write the dimensionless evolution equations, eliminating the pressure field. For this purpose, we apply the Laplacian operator, ∇^2, on the Eq. (59b) of v_z from Navier-Stokes equation, which yields:

$$\left(\nabla^2 - \frac{1}{Pr}\frac{\partial}{\partial t}\right)\nabla^2 v_z + \nabla^2 T - \frac{Ra}{Pr}\frac{\partial}{\partial z}\nabla^2 p = \frac{Ra}{Pr}\nabla^2\left(v_j \frac{\partial v_z}{\partial x_j}\right) . \tag{60}$$

Now, we derive an equation for the vertical component of the curl, or vorticity ($\zeta = \partial v_y/\partial x - \partial v_x/\partial y$) by applying the first derivative $\partial/\partial y$ on the equation for v_x, the first derivative $\partial/\partial x$ on the equation for v_y, from NS equation, and subtracting the first from the second one:

$$\left(\nabla^2 - \frac{1}{Pr}\frac{\partial}{\partial t}\right)\zeta = \frac{Ra}{Pr}\left[\frac{\partial}{\partial x}\left(v_x \frac{\partial v_y}{\partial x} + v_y \frac{\partial v_y}{\partial y} + v_z \frac{\partial v_y}{\partial z}\right) - \frac{\partial}{\partial y}\left(v_x \frac{\partial v_x}{\partial x} + v_y \frac{\partial v_x}{\partial y} + v_z \frac{\partial v_x}{\partial z}\right)\right] \tag{61}$$

Applying the divergence operator, $\nabla\cdot$, to NS equation, we have:

$$\frac{1}{Pr}\frac{\partial}{\partial t}\frac{\partial v_i}{\partial x_i} + \frac{Ra}{Pr}\left(\frac{\partial v_j}{\partial x_i}\frac{\partial v_i}{\partial x_j} + v_j \frac{\partial}{\partial x_j}\frac{\partial v_i}{\partial x_i}\right) = -\frac{Ra}{Pr}\nabla^2 p - \kappa_i \frac{\partial T}{\partial x_i} + \nabla^2 \frac{\partial v_i}{\partial x_i} \tag{62}$$

Since the velocity field is divergence free, we readily obtain

$$-\frac{Ra}{Pr}\nabla^2 p = \frac{Ra}{Pr}\frac{\partial v_j}{\partial x_i}\frac{\partial v_i}{\partial x_j} + \kappa_i \frac{\partial T}{\partial x_i} \tag{63}$$

Plugging this result in Eq.(60), we get the equation for the vertical component of the velocity field, from NS equation, without the pressure field,

$$\left(\nabla^2 - \frac{1}{Pr}\frac{\partial}{\partial t}\right)\nabla^2 v_z + \nabla^2 T + \frac{Ra}{Pr}\frac{\partial}{\partial z}\left(\frac{\partial v_j}{\partial x_i}\frac{\partial v_i}{\partial x_j}\right) - \frac{\partial T}{\partial z} = \frac{Ra}{Pr}\nabla^2\left(v_j \frac{\partial v_z}{\partial x_j}\right) , \tag{64}$$

which can be rewritten as

$$\left(\nabla^2 - \frac{1}{Pr}\frac{\partial}{\partial t}\right)\nabla^2 v_z + \nabla^2_\perp T = \frac{Ra}{Pr}\left[\nabla^2\left(v_j \frac{\partial v_z}{\partial x_j}\right) - \frac{\partial}{\partial z}\left(\frac{\partial v_j}{\partial x_i}\frac{\partial v_i}{\partial x_j}\right)\right] , \tag{65}$$

where $\nabla^2_\perp = \partial^2/\partial x^2 + \partial^2/\partial y^2$. The Boussinesq equations, without pressure, now read

$$\frac{\partial v_i}{\partial x_i} = 0 \tag{66a}$$

$$\left(\nabla^2 - \frac{1}{Pr}\frac{\partial}{\partial t}\right)\zeta = \frac{Ra}{Pr}\left[\frac{\partial}{\partial x}\left(v_j\frac{\partial v_y}{\partial x_j}\right) - \frac{\partial}{\partial y}\left(v_x\frac{\partial v_x}{\partial x_j}\right)\right] \tag{66b}$$

$$\left(\nabla^2 - \frac{1}{Pr}\frac{\partial}{\partial t}\right)\nabla^2 v_z + \nabla^2_\perp T = \frac{Ra}{Pr}\left[\nabla^2\left(v_j\frac{\partial v_z}{\partial x_j}\right) - \frac{\partial}{\partial z}\left(\frac{\partial v_j}{\partial x_i}\frac{\partial v_i}{\partial x_j}\right)\right] \tag{66c}$$

$$\frac{\partial T}{\partial t} + Ra\, v_j\frac{\partial T}{\partial x_j} = \alpha\nabla^2 T \ . \tag{66d}$$

Since we are interested in the vertical velocity and in the temperature field, we can rewrite the equations in matrix form with just these two fields, i.e.,

$$\frac{\partial}{\partial t}\begin{bmatrix}\nabla^2\tilde{v}_z \\ \tilde{T}\end{bmatrix} = \begin{bmatrix}Pr\nabla^4 & Pr\nabla^2_\perp \\ Ra & \nabla^2\end{bmatrix}\begin{bmatrix}\tilde{v}_z \\ \tilde{T}\end{bmatrix} + Ra\begin{bmatrix}\nabla_z\nabla_i\nabla_j\left(v_jv_i\right) - \nabla_i\nabla_i\nabla_j\left(v_zv_j\right) \\ \mathbf{v}_\perp\cdot\nabla_\perp T\end{bmatrix} , \tag{67}$$

such that the linear and nonlinear terms are easily spotted.

A.2 Linearized problem

Following Pontes et al. (2018), we linearize Eq. (67), and obtain decoupled equations for $\tilde{v}_z$ and $\tilde{T}$, which can be solved separately. It's straightfoward that we end up with just the linear terms from Eq. (67), such that

$$\frac{\partial}{\partial t}\begin{bmatrix}\nabla^2\tilde{v}_z \\ \tilde{T}\end{bmatrix} = \begin{bmatrix}Pr\nabla^4 & Pr\nabla^2_\perp \\ Ra & \nabla^2\end{bmatrix}\begin{bmatrix}\tilde{v}_z \\ \tilde{T}\end{bmatrix} , \tag{68}$$

where: $\nabla^2_\perp = \partial^2/\partial x^2 + \partial^2/\partial y^2$. Assuming solutions in the form

$$A\begin{bmatrix}\tilde{v}_z \\ \tilde{T}\end{bmatrix} = A\begin{bmatrix}V_{qn} \\ \Theta_{qn}\end{bmatrix}e^{\omega t + i\mathbf{qx}}\sin\left(n\pi z\right) + \text{c.c.} , \tag{69}$$

we reach the following dispersion relation:

$$a\omega^2 + a^2(Pr + 1)\,\omega + Pr\left(a^3 - Ra\,q^2\right) = 0 \ . \tag{70}$$

where: $a = q^2 + n^2\pi^2$. The Rayleigh number for which the growth rate ω vanishes is determined by the condition that the product of roots from the dispersion relation is zero. Then,

$$Ra = \frac{a^3}{q^2} = \frac{\left(q^2 + n^2\pi^2\right)^3}{q^2} \ . \tag{71}$$

The critical Rayleigh number (Ra_c) corresponds to the minimum of the curve in the last

term of RHS in eq. (70), such that

$$\frac{dRa}{dq} = \frac{6q\left(q^2 + n^2\pi^2\right)^2}{q^2} - \frac{2\left(q^2 + n^2\pi^2\right)^3}{q^3} = 2q^6 + 3q^4 n^2\pi^2 - n^6\pi^6 = 0 \qquad (72)$$

yields the positive real solution $q = n\pi/\sqrt{2}$. The instability threshold is given by the minimum of the lowest curve corresponding to first unstable mode ($n = 1$). We get

$$Ra_c = \frac{\left(q_0^2 + \pi^2\right)^3}{q_0^2} = \frac{27\pi^4}{4} \quad ; \quad q_0^2 = \frac{\pi^2}{2} \, . \qquad (73)$$

A.3 Instability mechanism

A.3.1 Linear domain

Since we are only insterest in the real roots close to the threshold, we find it preferable to search for their approximate values from order of magnitude comparison. Rewritting eq. (70), we have:

$$\omega^2 + a(Pr + 1)\,\omega + Pr\left(a^2 - Ra\,q^2/a\right) = 0 \, . \qquad (74)$$

In the vicinity of instability, we perform a Taylor expansion of the above equation around (Ra_c, q_0^2), using the relations: $Ra_c = a_0^3/q_0^2$; $q_0^2 = \pi^2/2$. Now the dispersion relation associated to the linear evolution matrix becomes:

$$\omega^2 + a_0(Pr + 1)\,\omega + a_0\,Pr\left[-a_0(Ra - Ra_c)/Ra_c + (q^2 - q_0^2)^2/q_0^2\right] = 0 \, . \qquad (75)$$

On the onset of instability ($Ra \sim Ra_c$), one of the eigenvalues stays negative (ω_2) while the other becomes slightly positive, close enough to zero ($\omega_1 \sim 0$). Therefore, by considering $\omega^2 \sim 0$ in eq. (75), we obtain ω_1. The negative eigenvalue ω_2 is then obtained by neglecting the last term in RHS of eq. (75) ($\omega_1\omega_2 \sim 0$). The first (ω_1) and the second (ω_2) eigenvalues correspond to the unstable modes and stable modes, respectively. Since $a_0 = q_0^2 + \pi^2$, we can write both eigenvalues as:

$$\omega_1 = \frac{Pr(q_0^2 + \pi^2)}{Pr + 1}\left[\left(\frac{Ra - Ra_c}{Ra_c}\right) - \frac{\left(q^2 - q_0^2\right)^2}{q_0^2(q_0^2 + \pi^2)}\right] ; \qquad (76)$$

$$\omega_2 = -(q_0^2 + \pi^2)(Pr + 1) \, . \qquad (77)$$

For high Prandtl values ($Pr \gg 1$), w_2 is strongly negative and, consequently, the separation between stable and unstable modes is even more evident. This instability mechanism appears in

Rayleigh-Bénard convection and similar ones are observed in many distinct physical, chemical, and biological systems.

A.3.2 Nonlinear domain

In the linear domain we obtained the eigenvalues corresponding to eigenmodes of interest in the onset of the instability. The positive eigenvalues defines a band of wavenumbers for which the corresponding modes are the unstable ones. Now, we address how these modes interact in the weakly nonlinear regime, i.e., when the first nonlinearity effects rise beyond instability threshold. It is expected that such interactions are compatible with the nonlinear terms present in the governing equations. For this purpose we may write the nonlinear equations of interest (for v_z and $\tilde{T}$) in matrix form, after eliminating the pressure field (Eq. 59):

$$\mathcal{L}\Psi + \mathcal{N}\left(\Psi\right) \;=\; 0\,, \tag{78}$$

where the two-component column vector Ψ and the linear operator matrix $\mathcal{L}$ are defined as

$$\Psi = \begin{bmatrix} v_z \\ T \end{bmatrix}\,, \quad \mathcal{L} = \begin{bmatrix} Pr\nabla^4 - \dfrac{\partial}{\partial t}\nabla^2 & Pr\nabla_\perp^2 \\[2ex] -Ra & \dfrac{\partial}{\partial t} - \nabla^2 \end{bmatrix}\,, \tag{79}$$

respectively. The symbol $\mathcal{N}\left(\Psi\right)$ is used to denote the two-component vector

$$\mathcal{N}\left(\Psi\right) \;=\; Ra \begin{bmatrix} \nabla_z \nabla_i \nabla_j \left(v_j v_i\right) - \nabla_i \nabla_i \nabla_j \left(v_z v_j\right) \\[1ex] \mathbf{v}_\perp \cdot \nabla_\perp T \end{bmatrix}\,, \tag{80}$$

that represents the (quadratic) nonlinearity in which we are expanding, and where the subscript $(\cdot)_\perp$ corresponds to the two dimensional catersian components, x and y. By adopting a discrete spectrum, i.e, ignoring finite band perturbations, and imposing periodic boundary conditions in x and y directions, we can express Ψ as:

$$\Psi(\mathbf{x}, z, t) = \sum_{\mathbf{q},n} \xi_{\mathbf{q},n}(t)\, \tilde{\Psi}_{\mathbf{q},n}(\mathbf{x}, z)\,, \tag{81}$$

where $\xi_{\mathbf{q},n}(t)$ are unknown time-dependent amplitudes. The sumation runs over all $\mathbf{q}$ and n. Plugging this definition into Eq. 78 and rearranging terms, we have

$$\frac{\partial \xi_{\mathbf{q},n}(t)}{\partial t}\begin{bmatrix} 1 & 0 \\ 0 & 1 \end{bmatrix}\tilde{\Psi}_{\mathbf{q},n} + \begin{bmatrix} aPr & -q^2 Pr/a \\ -Ra & a \end{bmatrix}\xi_{\mathbf{q},n}(t)\tilde{\Psi}_{\mathbf{q},n} + \mathcal{N}_{\mathbf{q},n}\left(\Psi\right) = 0 \tag{82}$$

where:

$$\mathcal{N}_{\mathbf{q},n}(\mathbf{\Psi}) = \frac{Ra}{a} \begin{bmatrix} \nabla_z \nabla_i \nabla_j (v_j v_i) - \nabla_i \nabla_i \nabla_j (v_z v_j) \\ a\, \mathbf{v}_\perp \cdot \nabla_\perp T \end{bmatrix} . \tag{83}$$

In order to obtain equations for the amplitudes $\xi_{\mathbf{q},n}(t)$, we multiply both sides of Eq. 82 by one of the eigenmodes $\tilde{\mathbf{\Psi}}^*_{\mathbf{q},n}(\mathbf{x}, z)$ and integrate over the normalization volume, such that

$$\int d\mathbf{x} \int_0^1 dz \left\{ A^2_{\mathbf{q},n} \tilde{\mathbf{\Psi}}^*_{\mathbf{q},n} \tilde{\mathbf{\Psi}}_{\mathbf{q},n} \right\} = \delta_{\mathbf{q},\mathbf{q}'} \delta_{n,n'} , \tag{84}$$

where $A^2_{\mathbf{q},n} = ||\mathbf{\Psi}_{\mathbf{q},n}||^{-2}$ is a normalization constant. Eq. 82 can then be rewritten as:

$$\frac{\partial \xi_{\mathbf{q},n}(t)}{\partial t} + \mathcal{L}_{\mathbf{q},n} \xi_{\mathbf{q},n}(t) + \int d\mathbf{x} \int_0^1 dz \left\{ A^2_{\mathbf{q},n} \langle \tilde{\mathbf{\Psi}}^*_{\mathbf{q},n}, \mathcal{N}_{\mathbf{q},n}(\mathbf{\Psi}) \rangle \right\} = 0 , \tag{85}$$

where $\langle \cdot, \cdot \rangle$ represents the inner product and:

$$\mathcal{L}_{\mathbf{q},n} = \begin{bmatrix} aPr & -q^2 Pr/a \\ -Ra & a \end{bmatrix} . \tag{86}$$

The linear evolution matrix from the linear domain analysis has a second row with opposite sign when compared to $\mathcal{L}_{\mathbf{q},n}$. However, the absolute values of ω are exactly the same and both satisfy $\mathcal{L}_{\mathbf{q},n} \xi_{\mathbf{q},n}(t) = -\omega(\mathbf{q}, n)\xi_{\mathbf{q},n}(t)$. Because the corresponding calculations reagarding the last term from the left hand side of Eq. 85 are simple in principle but somewhat lengthy, we quote only the final result. Considering the latter, now we can write equations for the amplitudes ξ's with the following structure:

$$\frac{\partial \xi_{\mathbf{q},n}(t)}{\partial t} = \omega(\mathbf{q}, n)\xi_{\mathbf{q},n}(t) - \sum_{\mathbf{q}',n'} \sum_{\mathbf{q}'',n''} H_{\mathbf{q},n\,;\mathbf{q}',n'\,;\mathbf{q}'',n''} \xi_{\mathbf{q}',n'}(t)\xi_{\mathbf{q}'',n''}(t) = 0 . \tag{87}$$

where $\omega(\mathbf{q}, n)$ represents the eigenvalues found in the linear domain analysis. The equation for the unstable mode then reads

$$\frac{\partial \xi_{\mathbf{q}_0,1}}{\partial t} = \frac{Pr(q_0^2 + \pi^2)}{Pr + 1} \left[\left(\frac{Ra - Ra_c}{Ra_c} \right) - \frac{\left(q^2 - q_0^2\right)^2}{q_0^2(q_0^2 + \pi^2)} \right] \xi_{\mathbf{q}_0,1} + H_1 \xi_{\mathbf{q}_0,1}\xi_{0,2} . \tag{88}$$

As a second step, we must consider the equation for the stable mode $\xi_{0,2}$:

$$\frac{\partial \xi_{0,2}}{\partial t} = -(q_0^2 + \pi^2)(Pr + 1)\xi_{0,2} - H_2|\xi_{\mathbf{q}_0,1}|^2 . \tag{89}$$

We now invoke the principle of adiabatic elimination, i.e., since $|\omega_2| \gg |\omega_1|$, the stable mode $\xi_{0,2}$ adapts rapidly to any change in the unstable mode $\xi_{\mathbf{q}_0,1}$. Accordingly we put

$$\frac{\partial \xi_{\xi_{0,2}}}{\partial t} = 0 \tag{90}$$

and readily obtain

$$\frac{\partial \xi_{\xi_{0,2}}}{\partial t} = -\frac{H_2}{(q_0^2 + \pi^2)(Pr + 1)} \cdot |\xi_{\mathbf{q}_0,1}|^2 \, , \tag{91}$$

which allow us to eliminate $\xi_{0,2}$ in the equation for the unstable modes, which now become the order parameters. The final equation reads

$$\frac{\partial \xi_{\mathbf{q}_0,1}}{\partial t} = \frac{Pr(q_0^2 + \pi^2)}{Pr + 1} \left[\left(\frac{Ra - Ra_c}{Ra_c} \right) - \frac{\left(q^2 - q_0^2 \right)^2}{q_0^2(q_0^2 + \pi^2)} \right] \xi_{\mathbf{q}_0,1} - \frac{H_1 H_2}{(q_0^2 + \pi^2)(Pr + 1)} |\xi_{\mathbf{q}_0,1}|^2 \xi_{\mathbf{q}_0,1} \, . \tag{92}$$

Since all the wave numbers from the unstable modes are close to $\mathbf{q}_0$, one obtains, in scaled variables, the equivalent equation in Fourier space,

$$\frac{\partial \psi_{\mathbf{q}}}{\partial t} = \left[\varepsilon - \left(q^2 - q_0^2 \right)^2 \right] \psi_{\mathbf{q}} - \int \int d\mathbf{q}' d\mathbf{q}'' \psi_{\mathbf{q}-\mathbf{q}'} \psi_{\mathbf{q}'-\mathbf{q}''} \psi_{\mathbf{q}} \, . \tag{93}$$

which reads, in real space,

$$\frac{\partial \psi(\mathbf{x}, t)}{\partial t} = \left[\varepsilon - \left(\nabla^2 - q_0^2 \right)^2 \right] \psi(\mathbf{x}, t) - \psi(\mathbf{x}, t)^3 \, , \tag{94}$$

where $\varepsilon = (Ra - Ra_c)/Ra_c$ is the bifurcation or control parameter. Since this equation is derived for describing the planform view of Rayleigh-Bénard convection cells, we have a two-dimensional Laplacian operator, which, in cartesian coordinates, reads: $\nabla^2 = \partial^2/\partial x^2 + \partial^2/\partial y^2$. This last equation is known as the Swift-Hohenberg (SH) equation and a similar mathematical procedure was performed by Jack Swift and Pierre Hohenberg, in 1977 (SWIFT; HOHENBERG, 1977), to derive their model.

APPENDIX B – Pseudo-spectral schemes for solving the one-dimensional Newell-Whitehead-Segel equation

In the weakly nonlinear analysis section, a pair of coupled Newell-Whitehead-Segel (NWS) equations (Eqs. (20) and (21)) is derived for the modes $A(\mathbf{x}, t)$ and $B(\mathbf{x}, t)$ via the multiple scale formalism. In order to compare the amplitude envelopes from SH simulations and the ones described by those amplitude equations, we develop numerical solutions for the NWS. The one-dimensional (x-direction) NWS equation has the form,

$$\partial_t u = \varepsilon(\mathbf{x})u - \alpha\partial_x^4 u + 3\beta u^3 \, , \tag{95}$$

where $\alpha = 1$, $\beta = -1$, $t \geqslant 0$ and $u = uivu(x, t)$ is a real function described in the regular domain $\Omega : \{x \in [0, L_x]\}$ with periodic boundary conditions (PBC) and generalized Dirichlet boundary conditions (GDBC). Since an analytical study is not trivial for this equation, we develop a numerical study using a semi-implicit pseudo-spectral method with first-order accuracy in time. The Fourier approach is adopted for the configurations with periodic boundary conditions (PBC). The Chebyshev approach is adopted for the configurations subjected to generalized Dirichlet boundary conditions (GDBC), for dealing with the imposed boundary conditions. Both approaches are briefly discussed in the following sections.

B.1 Fourier pseudo-spectral scheme

The eigenfunctions of the fourth-order differential operator over the domain with periodic boundary conditions (PBC) are the Fourier modes $e^{ik \cdot x}$ ($k \in \mathbb{Z}^N$). Since $\partial_x^4 e^{ik \cdot x} = |k|^4 e^{ik \cdot x}$, Eq. (95) can be written as

$$\partial_t \hat{u}_k = \varepsilon(\mathbf{x})\hat{u}_k - \alpha|k|^4\hat{u}_k + 3\beta\hat{u}_k^3 \, , \tag{96}$$

where $\hat{u}_k$ is the Fourier coefficient associated with the mode k. The fourth order derivative term is treated implicitly since it has a numerical stabilizing property (denoted by index $n + 1$). The control parameter linear term is explicit since it is destabilizing in the scheme (denoted by index n). The nonlinear terms are computed in real space in order to avoid computing Fourier mode convolutions (higher computational effort) and therefore are treated explicitly. Since we are interested in the steady state solution, a semi-implicit first order accurate in time scheme is employed, that can be expressed as follows:

$$\hat{u}_k^{n+1} = \mu_k \left(\hat{u}_k^n + \Delta t \hat{f}^n \right) \, , \tag{97}$$

where $\mu_k = \left(1 + \alpha \Delta t k^4\right)^{-1}$ and $\hat{f}^n = \mathcal{F}(f(u^n))$ is the Fourier transform of the nonlinear and variable coefficient terms $f(u^n) = \varepsilon(\mathbf{x})u^n + 3\beta(u^n)^3$. This transformation is performed via a fast Fourier transform (FFT)-based code without dealiasing, using Octave FFT library.

B.2 Chebyshev pseudo-spectral scheme

Equation (95) is solved using Chebyshev spectral collocation method (BOYD, 2001). Chebyshev polynomials of degree n have n zeros in the interval $\xi \in [-1, 1]$ that should be mapped to the physical domain $x \in [0, L_x]$. For that purpose, a simple mapping is chosen: $x = 0.5(\xi + 1)L_x$. The numerical scheme can be expressed as

$$\left(I + \alpha \Delta t D_x^4\right) u^{n+1} = u^n + \Delta t f^n \,, \tag{98}$$

where $f^n = \varepsilon(\mathbf{x})u^n + 3\beta(u^n)^3$ and D_x^4 is the Chebyshev collocation for the fourth-order differential operator on the mapped domain. This system of linear equations is solved subjected to the boundary conditions for the amplitude B. For such purpose we adopted $B = \partial B/\partial x = 0$, for the boundary points $x = 0$ and $x = L_x$. These conditions are consistent with the GDBC used in the SH equation simulations, for the order parameter ψ.

APPENDIX C – Pseudo-spectral scheme for solving the two-dimensional Swift-Hohenberg equation in periodic domains

Larger computational domains tend to become expensive in terms of computing power and time, since it corresponds to dealing with very large matrices within the code. Spectral methods are usually employed to partially overcome this issue, and their implementation is very straightforward for regular geometries using periodic boundary conditions, which are the main focus here. For the sake of the completeness of this work, in this Appendix, a semi-implicit pseudo-spectral scheme has second-order accuracy in time is presented. The order parameter u is computed after each time step using a combination of Crank-Nicolson and Adams-Bashforth schemes in Fourier space. For such task, we respectively define the linear operator L_q, and the Fourier transform N_q of the nonlinear terms as

$$
L_q = \omega \hat{u}_q = \left[-(q^2 - q_0^2)^2\right] \hat{u}_q \ ,
$$
$$
N_q = \mathcal{F}\left(\epsilon(\mathbf{x})u - u^3\right) \ .
$$

We then use a combination of the implicit Crank-Nicolson (CN) scheme for the linear terms with an explicit, second-order Adams-Bashforth (AB) scheme for the nonlinear terms in Fourier space to integrate eq. (8),

$$
\frac{\hat{u}_q^{n+1} - \hat{u}_q^n}{\Delta t} = \frac{1}{2}\left[(\omega \hat{u}_q)^{n+1} + (\omega \hat{u}_q)^n\right] + \frac{1}{2}\left[3N_q^n - N_q^{n-1}\right] \ .
$$

Then, we obtain u for the new time,

$$
\hat{u}_q^{n+1} = \frac{\left(1 + \dfrac{\Delta t}{2}\omega^n\right)\hat{u}_q^n + \dfrac{\Delta t}{2}\left(3N_q^n - N_q^{n-1}\right)}{\left(1 - \dfrac{\Delta t}{2}\omega^{n+1}\right)} \ .
$$

Returning to physical space by using the iFFT then reads

$$
u^{n+1} = \mathcal{F}^{-1}(\hat{u}_q^{n+1}) \ .
$$

Since $\omega = -(q^2 - q_0^2)^2$, the quantity $(1 - (\Delta t/2)\omega^n) > 1$, which is required for numerical stability of the linear part, at least. Note that $\omega^{n+1} \equiv \omega^n$, so a single ω can be evaluated before the main loop, which is desired for implementing parallel code processing, allow higher performance computing.

APPENDIX D – Computational implementation

The code solves the Swift-Hohenberg evolution equation for the order parameter through an inhouse developed Python code which relies on the Numpy, Scipy library, and other standard libraries for data processing. Sparse matrices are implemented in order to reduce computational cost in the simulations. This code is available on github.com/dancoelho/swifthohenberg.

Most of the numerical simulations were carried out on the computers of the Laboratory of Numerical Tests (LEN) from the Group for Environmental Studies in Reservoirs (GESAR), and a personal computer with the following configuration, respectively:

- ★ AMD FX-8350 4GHz with 8 Cores, 32GB of RAM memory. HDD: 1TB. Operational system: LINUX Ubuntu 18.04 LTS, with Python 3.5.

- ★ Intel(R) Core(TM) i5-3330 CPU @ 3.00GHz, 4 Cores, 16GB of RAM memory. SSD: 120GB; HDD: 1TB. Operational system: Windows 10 Professional, with Python 3.5.

APPENDIX E – Conference Proceeding and Journal Publications

During the development of the present master thesis, a conference proceeding was produced, submitted, and accepted for oral presentation at the 25th International Congress of Mechanical Engineering (COBEM). The event, that started on October 20th, 2019, took place in Uberlândia Federal University (UFU), Uberlândia MG, Brazil.

⋆ COELHO, D. L., VITRAL E., PONTES, J., MAGIAVACCHI, N. Pattern formation survey on nonuniformly forced Swift-Hohenberg equation. 25th International Congress of Mechanical Engineering (COBEM), 2019. [ResearchGate]

Some manuscripts containing developments and results from the present work were produced and submitted to two Journals. They are already considered for publication and are currently under review process. The first manuscript contains the numerical framework exposed in Chapter 3 and was submitted to Journal of Computational and Applied Mathematics (JCAM) on March 25th, 2020:

⋆ COELHO, D. L., VITRAL E., PONTES, J., MAGIAVACCHI, N. Numerical scheme for solving the nonuniformly forced cubic and quintic Swift-Hohenberg equations strictly respecting the Lyapunov functional. Submitted to *Journal of Computational and Applied Mathematics*, Elsevier Science, 2020. [arXiv]

The second manuscript addresses questions about the preferred orientation of stripe patterns (using SH equation) in the presence of a gradient of the bifurcation/control parameter exposed in Chapter 2 and was submitted to Physical D: Nonlinear Phenomena on February 26th, 2021:

⋆ COELHO, D. L., VITRAL E., PONTES, J., MAGIAVACCHI, N. Stripe patterns orientation resulting from nonuniform forcings and other competitive effects in the Swift-Hohenberg dynamics. Submitted to *Physica D*, Elsevier Science, 2021. [arXiv]

Both submitted manuscripts are available on `https://arxiv.org/`, and are attached by the end of this appendix, respectively.